Artificial multiferroic heterostructures: Magnetoelectric coupling and dynamics

Inauguraldissertation
zur
Erlangung der Würde eines Doktors der Philosophie
vorgelegt der
Philosophisch-Naturwissenschaftlichen Fakultät
der Universität Basel

Von

Jaianth Vijayakumar

Aus Indien

Basel, 2019

Genehmigt von der Philosophisch-Naturwissenschaftlichen Fakultät auf Antrag von

Fakultätsverantwortlicher: Prof. Dr. Frithjof Nolting

Korreferent: Dr. Florian Kronast

Basel, 26.03.2019

Prof. Dr. Martin Spiess

Contents

Abstract

Artificial multiferroics consist of materials systems engineered to have a coupling between multiple order parameters at the interface, such as between magnetic and ferroelectric order (magnetoelectric coupling) which enable the electric field control of magnetism suitable for applications in energy efficient storage or sensor devices. In this thesis we investigate two types of magnetoelectric coupling, namely, strain-mediated and charge-mediated, with a goal of characterizing their dynamic behaviour. For strain-mediated coupling, we considered a system consisting of Co dots fabricated on a ferroelectric $BaTiO_3$ thin film, where application of an electric field led to a change in magnetic domain structure induced by the piezo-strain; however, we find that the process is stochastic as a consequence of a strong pining of the Co magnetization induced by the high surface roughness of $BaTiO_3$ making it unsuitable for pump and probe dynamical characterization. A second type of system investigated consists of perpendicular magnetic anisotropy (PMA) structures deposited on a silicon nitride membrane gate dielectric, where we used the charge screening effects to modulate the charge carrier density at the metallic/silicon nitride interface. We studied two types of tri-layer structure (i) Pt/Co/Pt/Si_3N_4 and (ii) Pt/Co/Ta/Si_3N_4, where the Co thickness is chosen to be at spin reorientation transition. For Pt/Co/Pt, we find the presence of a charge mediated magnetoelectric coupling in the form of domain nucleation and domain wall fluctuations dependency with the electric field; from the latter we estimate a change in energy barrier height of about 10 %. For Ta/Co/Pt heterostructures a net Dzyaloshinskii-Moriya interaction (DMI) is expected and the goal was to investigate the possibility to control the DMI and/or skyrmions with applied electric fields. For these structures we observe the presence of out-of-plane spin structures in an in-plane dominant magnetized surroundings. The out-of-plane spin structures resemble a Néel type skyrmion with a dimension from 200 nm to 2 μm at room

temperature under no external magnetic field. We demonstrate that such out-of-plane spin structures can be manipulated by changing the anisotropy of the system with electric fields. The measured capacitive rise time of a 200 nm thick silicon nitride membrane is $\sim$140 ns making it suitable for high frequency characterization; however, we find that the presence of charge traps and/or charge defects in the silicon nitride membranes preclude a systematic control of the magnetization. In this context, we characterize the dielectric time response of different dielectrics, including stoichiometric silicon nitride membranes, AlN, Al_2O_3, $BaTiO_3$ and MgO grown by physical vapour deposition (PVD) methods. We find that all dielectrics have a significant density of charge defects and/or charge traps. From capacitance vs frequency characterization, we find that the capacitance decreases with increasing frequency; since the mobility of carrier charges such as electrons is independent of the measuring frequency and we measure a higher capacitance at lower frequency, it is likely that we are also moving ions or possible vacancies with the applied electric field along with bound electrons, as ionic mobility with electric field is slower than electron mobility. Our results suggests the importance of characterizing and optimizing the dielectric time response for high frequency charge mediated magnetoelectric devices.

Chapter 1

General Introduction

All materials surrounding us, such as a grain of sand or a piece of rock, could potentially become a valuable item for the future if we understand its characteristics and capabilities. It is silicon present in a grain of sand which forms the basis for most of the present day silicon based electronic devices positioning itself in a multibillion dollar industry. Therefore, understanding the science of a material can result in new inventions capable of solving problems for humanity. Multiferroic materials are one such type of materials with potential for replacing more conventional materials used in electronic components and devices, with a better functionality and more efficient use of energy [1]. Multiferroics are a class of materials where magnetism can be controlled by applying an electric field. Multiferroic properties can exist in single phase compound known as intrinsic multiferroics or at the interface of ferromagnetic and ferroelectric composite material known as artificial multiferroics. Magnetization in an artificial multiferroic material can be controlled by means of strain or charge modulation arising from ferroelectric/dielectric material or exchange bias effect with the presence of a antiferromagnetic multferroic material. The phenomenon of (artificial)multiferroics is described in detail in the next chapter.

Multiferroic materials have many possible applications including; amplifiers [2], AC/DC magnetic field sensors [3] [4] [5] [6], microwave resonators tuned electrically [7] [8] [9], microwave phase shifters, microwave signal delay lines, magnetic recording heads, random access memories [10] [11] [12], solar cells [13] and energy harvesting [14] [15] [16] [17]. In this thesis we focus on the electric field control of magnetism using multiferroic heterostructures suitable for memory and storage devices.

Storage and memory devices such as hard disk drives (HDD) or a magnetic random access memory (MRAM) which are non-volatile memory devices (where information is stored even when the power is off) are important components in electronic devices such as laptops or smart phones; in addition the demand for better use of energy and functionality in such devices are always high. In HDD devices, a bit of data is stored in the form of magnetic domains; currently a HDD is capable of storing 1 Tb/in^2 [18] [19] [20]; in order to read and write data, a HDD uses a read head and a write head. To carry out both read and write operations electrical currents in the order of mA and above are necessary. The write head is basically an electromagnet which produces a strong enough magnetic field to change the local magnetization of the magnetic recording medium and a read head consisting of a tunnelling magnetoresistive (TMR) device.

A TMR device consists of a tunnelling junction in a ferromagnet/insulator/ferromagnet structures, where one of the ferromagnetic layers has a fixed magnetization, and the other ferromagnetic layer is called a free layer, change its magnetization with small magnetic fields. The resistance across the junction varies depending on the magnetization of the free layer; the read head scans across the HDD magnetic layer and the free layer which is sensitive to the local magnetization from the HDD, change its magnetization depending on the local magnetic field from the domains in the HDD. A high magnetoresistance state is observed, if the spin of the fixed layer is up and the HDD domain is down, and when the spin states are same (both layers have spin up/down) we have a low resistance state, the difference between the high and low magnetoresistance states can be about 30 %. Nevertheless, the read out of magnetoresistance can result in a current flow of few mA [21], which can lead to thermal noise and heat.

A MRAM device consist of many TMR junctions, with each structure having a heterostructure configuration of a fixed magnetization layer/insulator/free layer; the magnetization of the free magnetic layer can be controlled by applying an electric current, which acts as a storage bit. The energy consumption associated with this process is higher than the energy consumed by a commercially used dynamic RAM (DRAM), where an electric field is utilized instead. However, MRAM is considered to offer a faster read and write time and longer retention of information over DRAM, static RAM (SRAM) or flash memory [22].

In both cases of HDD and MRAM, if the operations were performed using electric field instead of electric currents, the energy consumption could be significantly reduced without the need for a compromise in the functionality.

For TMR junction based devices used in MRAM or read heads, several proposals have already been made to use artificial multiferroic heterostructures [10] [11] [12]. Similarly, in order to increase the storage density, magnetic spin structures with smaller dimensions such as skyrmions were proposed instead of magnetic domains, and it has been demonstrated that such spin structures can also be controlled by electric field using gated dielectrics [23] [24] [25] [26]. Besides these ideas and proposals, there are still many other challenges such as stabilization of skyrmions at room temperature, sample growth, fabrication, design of read or write head which needs to be addressed in order to create working devices.

Nevertheless, in order to replace the current technology, the newly proposed artificial multiferroic components should not only be energy efficient but also posses equal or better functionality with a similar size, simple fabrication process, durability and performance. The read and write time of one bit associated with a HDD is in the order of μs and ns respectively. Therefore, the multiferroic devices should operate in such time period or faster; hence, investigation of the time response of the magnetoelectric coupling is required. Previous studies on single phase multiferroics or artificial multiferroics have demonstrated its functionality in static or at low frequency regime (few kHz) [27] [28] [29] and recently a MHz frequency characterization on a strain mediated coupling device was made using a substrate capable of producing surface acoustic waves [30]; these heterostructures need to be scaled down in size in order to use it as MRAM or read head devices, and this process comes with many challenges. Such challenges arise predominantly from the ferroelectric/dielectric component as follows:

1. A thin ferroelectric layer may contain charge defects that may result in leakage currents [31] [32] [33], therefore to have an effective insulation, the ferroelectric layer has to be sufficiently thick. Similar problems can be expected when using a dielectric material instead of a ferroelectric material. A permissible leakage current in DRAM devices is 10 μA/cm^2 [34] and in such devices SiO_2 or SiO_2 in combination of Si_3N_4 is used as a dielectric, with a total thickness of about 10 nm [35] [36].

2. With thicker ferroelectric layers, however, obtaining a smooth surface is challenging, while the latter is required for an effective coupling [37] [38].

3. Ferroelectric layers below a certain critical thickness (typically 3 nm and below) may not be ferroelectric [39] and the field effect can also result from ionic displacement instead of charge displacement resulting in a slower process [40] making it not suitable for high frequency applications.

The goal of this thesis is to investigate the time response of magnetoelectric coupling in the μs or lower time scale in devices with micrometer dimensions and to estimate how quick the magnetic component responds to a change created by the ferroelectric/dielectric component at the interface through strain or charge modulation. With this objective, we first explore the possibility to scale down the device size with appropriate fabrication methods and sample growth processes for different artificial multiferroic heterostructures using suitable combinations of ferromagnetic/ferroelectric or ferromagnetic/dielectric materials. We investigate devices made of Co/$BaTiO_3$ and Si_3N_4/Pt/Co/Pt structures for strain and charge mediated coupling, respectively, and we find the presence of magnetoelectric coupling in both cases. However, the presence of intrinsic defects in $BaTiO_3$ and Si_3N_4 resulted in a lack of systematic control in magnetoelectric coupling, which prevented the high frequency characterization. We also find the presence of magnetic domain with out-of-plane magnetization surrounded by in-plane spins in Ta/Co/Pt heterostructures, induced by the Dzyaloshinskii-Moriya interaction (DMI) and stabilized by the surface roughness of Si_3N_4 membrane, a type of spin configuration not reported before. We find that such out-of-plane spin structures are stable at room temperature without a need for an external magnetic field, can be controlled by an electric field, and have properties that resemble skyrmionic structures. The challenges related to the sample growth and fabrication methods demonstrated in this thesis can provide appropriate guidance for the optimization of magnetoelectrically coupled devices for high frequency operations in electric field control of magnetism. Furthermore, we have also designed experiments suitable for characterizing magnetoelectric coupling at high frequency using optical, electrical and X-ray based techniques. With well optimized fabrication and sample growth processes, we expect that the multiferroic devices investigated in this thesis can operate in similar time scales as those of commercial HDD or MRAM devices. The new type of

spin structures found from our experiments can open new possibilities to explore roughness induced/stabilized spin structures and possible data storage applications similar to skyrmions.

The thesis comprises of seven chapters. Chapters 1-3 consist of fundamentals related to artificial multiferroics, sample preparation, lithography and characterization. The experimental results of this thesis are described in chapters 4-7. The contents of the individual chapters are as follows:

Chapter 2 discusses the basics of the magnetic energy terms and of artificial multiferroics; since the goal of this thesis is to perform high frequency characterization, we describe the conditions required to have the appropriate devices. The last part gives an introduction to skyrmions.

Chapter 3 discusses the different deposition techniques, lithography methods, and the magneto-optic Kerr effect (MOKE) and X-ray characterization tools used in this work.

Chapter 4 presents the results from strain mediated magnetoelectric coupling in $Co/BaTiO_3$ and $Ni/BaTiO_3$ heterostructures, the fabrication requirements, and the challenges and future plans.

Chapter 5 presents the results from charge mediated coupling in Si_3N_4 gated Pt/Co/Pt heterostructures, comprising the results from X-ray photoemission electron microscopy (XPEEM), MOKE and transmission X-ray characterization.

Chapter 6 describes the spin structures formed by Ta/Co/Pt heterostructures on Si_3N_4, where we find a possible skyrmionic-like structure in a system with dominant in-plane (IP) magnetic anisotropy.

Chapter 7 presents the results from the high frequency characterization of different dielectrics and its suitability for high frequency characterization of magnetoelectric coupling devices.

Chapter 2

Magnetoelectric coupling and Magnetic spin structures

The functionality of an artificial multiferroic heterostructures originated from the intrinsic and microscopic properties of ferromagnetism and ferroelectricity. This chapter provides a brief description on how ferromagnetism can be controlled by inducing changes in different microscopic magnetic energies and introduces single phase and artificial multiferroics with a focus on strain- and charge-mediated coupling to control magnetism. Since for applications high frequency operation is desired, the fabricated device should be suitable for high frequency characterization and a description on the physical requirements, such as sample dimension and the corresponding electrical properties, will be discussed. Part of this thesis also deals with the observation of skyrmions-like spin structures, therefore an introduction to skyrmions will be given in the last section.

2.1 Magnetic energies

A ferromagnetic material consists of many magnetic domains whose net magnetization can point in different directions. The net magnetization of the system is determined by the point where the total magnetic energy is at a minimum. The total magnetic energy (E) is given by

$$E = E_{\text{Exchange}} + E_{\text{DMI}} + E_{\text{Anisotropy}} + E_{\text{Zeeman}} + E_{\text{Demag}} + E_{\text{Magneto-elastic}} \tag{2.1}$$

The different energy contributions are as follows:

1. E_{Exchange} is the exchange interaction energy, which is the fundamental interaction between two spins responsible for magnetic ordering, whose Hamiltonian is given as $H = \sum_{i,j} J_{i,j}.\vec{S_i}.\vec{S_j}$, where J_{ij} is the exchange integral, $\vec{S_i}$ and $\vec{S_j}$ represents the two interacting spins (i,j).

2. E_{DMI} is the asymmetric exchange interaction (Dzyaloshinskii-Moriya interaction - DMI), between the ferromagnetic material with an another material with large spin-orbit coupling and can also exist in single phase material (with non-centrosymmetric structure), the Hamiltonian is given as $H = \vec{D}_{i,j}.(\vec{S_i} \times \vec{S_j})$, where $\vec{D}$ is the DMI vector which determines the direction of rotation of the interacting spins, and is responsible for the formation and stabilization of skyrmions.

3. $E_{\text{Anisotropy}}$ is the energy term which determines the energetically favourable directions in a material.

4. E_{Zeeman} is the Zeeman energy, corresponding to the interaction energy between the magnetization and the external magnetic field, given as $\text{E} = \mu_0 \int_V \vec{M}.\vec{H}dV$, where $\vec{M}$ is the net magnetization, $\vec{H}$ is the external magnetic field and V is the volume.

5. E_{Demag} is the demagnetization energy, also called magnetostatic energy, which originates from the magnetic stray field from the sample. This term also contributes to the shape anisotropy given as $(2\pi M_s^2)$, where M_s is the saturation magnetization (magnetic moment per unit volume).

6. $E_{\text{Magneto-elastic}}$ is the energy caused by the strain within crystal lattice.

A change in any energy term results in a change in the total energy, thereby changing the magnetization of the system to another energy minimum. Conventional methods to induce a change in these energy terms include using a magnetic field or electric current (eg. spin transfer torque) [41] [42] [43]; other methods such as thermal assisted or

laser induced control of the local magnetization are also being investigated [44] [45] [46]. Dielectrics and ferroelectrics interfacing a ferromagnetic material in artificial multiferroic structures can also induce changes in the magnetic energy, as will be described in the coming sections.

2.2 Artificial Multiferroics

Multiferroics are a class of materials where there is a coupling between multiple order parameters, for example, between ferromagnetic and ferroelectric orders (magnetoelectric coupling), by which one can control magnetism using electric fields and by using magnetic fields one can control the ferroelectric properties [47] [48] [49]. The magnetoelectric coupling tensor can be obtained by expanding the free energy term of a multiferroic material using multivariant Taylor series as a function of electric and magnetic field induction [50] [51],

$$-F(\vec{E},\vec{B}) = F_0 + \vec{P}\vec{E}_i + \vec{M}\vec{B}_i + \frac{\epsilon_0}{2}\sum_{ij}\chi^e_{ij}\vec{E}_i\vec{E}_j + \frac{1}{2\mu_0}\sum_{ij}\chi^m_{ij}\vec{B}_i\vec{B}_j + \underbrace{\frac{\delta\vec{P}_i}{\delta\vec{B}_j}\vec{E}_i\vec{B}_j}_{\text{magnetoelectric}} + \dots \quad (2.2)$$

Where, $\vec{P}$ and $\vec{M}$ represent spontaneous polarization and magnetization, $\vec{E}$ and $\vec{B}$ represents electric field and magnetic field induction vector, χ^e_{ij} and χ^m_{ij} are electric and magnetic susceptibility, ϵ_0 is the permitivitty in vacuum, μ_0 is the permiability of vacuum. The change in magnetization as a function of applied electric field or a change in ferroelectric polarization with applied magnetic field can be observed as a quadratic order, described by the magnetoelectric coupling tensor α_{ME}. Multiferroic properties can exist in single phase compounds known as single phase multiferroics, such as $BiFeO_3$ [52] [53] [54] [55]. However, their number is relatively small and they tend to either order at relatively low temperatures or have small magnetoelectric couplings. Artificial multiferroics consist of a ferromagnetic material interfaced with a ferroelectric system such that a magnetoelectric coupling is induced at the interface. They have the advantage over single phase multiferroics of stronger magnetoelectric couplings and room temperature operation [47] [27] [49] [56]. By combining piezoelectric and magnetrostrictive properties one can obtain a strain-mediated magnetoelectric coupling; while by using a ferroelectric as

a gate dielectric one can obtain charge-mediated magnetoelectric coupling, which takes advantage of the high magnitude of the permittivity, resulting in modulation of a large quantity of interfacial charges. One can also obtain a magnetoelectric coupling through exchange-bias effects between multiferroic and antiferromagnetic heterostructures. In this thesis we explore both strain and charge mediated magnetoelectric coupling.

In a strain mediated coupling system, the ferroelectric interface creates a piezo-strain, which induces a distortion in the unit cell of the interfacing ferromagnetic material. Strain-mediated coupling has been demostrated in many multiferroic system such as $CoFeB/BaTiO_3$ [57] [58], Ni/PMNPT [59], $Co/PbZrTiO_3$ [28] among others [47]. Similarly, piezoelectric materials without ferroelectric order such as AlN [60] or ZnO [61] have also been used to create strain-mediated coupled magnetoelectric heterostructures. The ferromagnetic material changes its net magnetic moment due to inverse magnetostriction effect created by the strain. The sensitivity of a magnetic material towards strain is characterized by the magnetostrictive coefficient (λ_{xyz}) which gives the relative change in dimension along the xyz crystal axis. The value of λ for polycrystalline Ni and Co is -34 $\times$ 10^{-6} and -62 $\times$ 10^{-5}, respectively [62], which are among the highest within the 3d transition metals. When there is a crystallographic distortion, the magneto-elastic energy changes (eqn.2.1), which in turn changes the total energy minima and the overall magnetization configuration of the material. A schematic of the strain mediated coupling is shown in Fig. 2.1.

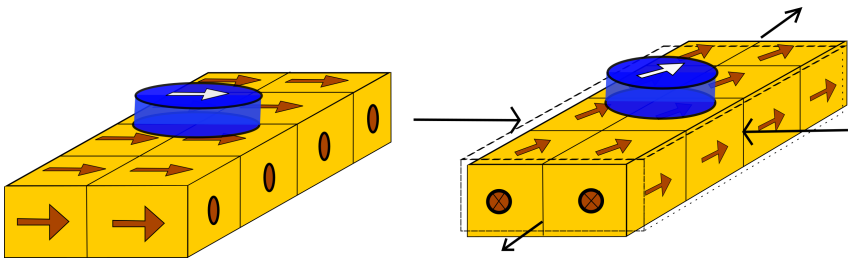

Figure 2.1: Schematic of strain-mediated coupling. The yellow structure indicates the ferroelectric layer with spontaneous polarization indicated by red arrow; the blue structure represents the ferromagnetic layer whose net magnetization is indicated by white arrow.

Charge-mediated magnetoelectric coupling employs the strong polarizable nature of

the ferroelectric material and its ability to modulate the interfacial charges to a large extent. Modifying the interfacial charges can result in a change in interfacial anisotropy (in ferroelectric/ferromagnetic) and a shift in the Fermi level which can result in a change in the density of spin up and spin down electrons near the Fermi level which determines the magnetic moment as described by Band theory of ferromagnetism where the net magnetic moment is determined by the difference between spin up and spin down electrons. The effect of charge modulation is only present for few atomic layers corresponding to the charge screening length, it is necessary that the interfacing ferromagnetic material be thin (< 1 nm). However, changes in the interfacial anisotropy can result in large change in the magnetic energy and in turn in the net magnetization [63] [64]. A schematic of charge-mediated coupling is shown in Fig. 2.2. Charge-mediated magnetoelectric coupling has been demonstrated in artificial multiferroic heterostructures such as $LaSrMnO_3/BaTiO_3$ [65] [40], $PbZrTiO_3/LaSrMnO_3$ [66] [67] [37] [68] [69] [70] and Fe/PMN-PT [71]. Similarly, charge mediated coupling can also be found at the interface of a ferromagnetic and a dielectric layer [64] [72]. Charge-mediated coupling can involve movement of ions across the interface which can result in a modification of the magnetic anisotropy, magnetic moment, or the magnetic ground state by a chemical mechanism. For example, at the interface between Co/GdO_x [73] [74], the Co layer changes its anisotropy due to the oxidation of a few layers of Co as a result of the movement of oxygen ions at the interface with the applied electric field. Charge mediated coupling due to modulation of charges is preferred over coupling due to ionic movements as the movement of charge is faster and provides the possibility for high frequency applications.

A functional artificial multiferroic device is effectively a capacitive structure with the dielectric or ferroelectric with the ferromagnetic component engineered to be interfaced with the insulators. For example, the charge mediated coupling devices fabricated in this thesis have a capacitive structure of the form metal-ferroelectric (or dielectric)-ferromagnetic, therefore characteristic features of the capacitor devices need to be considered in making the design. Especially, the capacitance can limit the time response of the material through the RC time constant which is discussed in the next section.

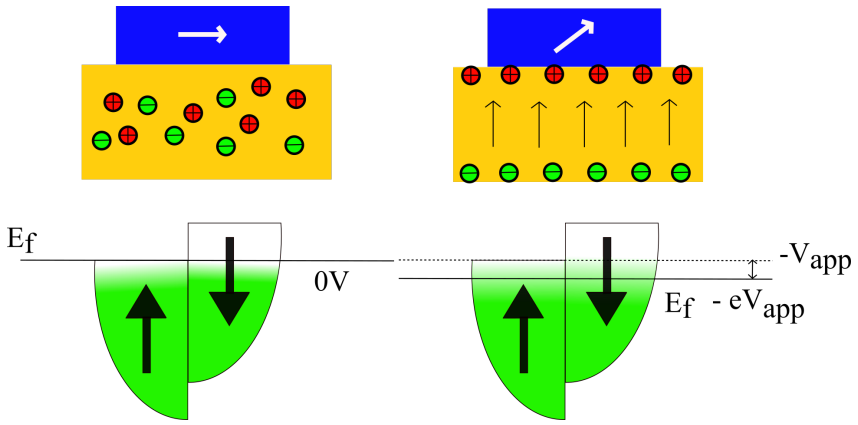

Figure 2.2: Schematic of charge mediated coupling: the yellow layer represents a dielectric layer (which is not polarized) and the net magnetization is indicated by the white arrow in the ferromagnetic layer (blue region). With the application of electric field, the magnetization can change due to a change in the Fermi level as indicated in the schematic. The coloured (green) region and white region represent occupied and unoccupied states respectively.

2.3 Designing a multiferroic heterostructure for high frequency characterization

Since we require a capacitive structure in artificial multiferroic systems, for high frequency characterization one must take into account the frequency dependence of the capacitor structure of the device, especially the capacitance rise time and the cut-off frequency, to have an effective coupling. The capacitance of an ideal capacitor is $C = Q/V$ where Q is the charge displaced with applied voltage V, and C is independent of applied voltage or the frequency. However, in a non-ideal case, small changes in the capacitance are inevitable both with frequency and with applied voltage. The capacitance C is given by the physical dimension and the permittivity of the dielectric material as $C = \epsilon_0 \epsilon_r A/d$, where ϵ_0 is permittivity in vacuum, ϵ_r is the relative permittivity of the material, A and d is area and thickness, respectively. The rise time of a capacitor is defined as the time taken to accumulate about 63.2% of the total charge with the applied electric field. It is the rise time that can affect the magnetoelectric coupling at high frequency: if the

rise time is larger than the time period of the applied voltage pulse, then the magnitude of magnetoelectric coupling will be less than that observed with the same magnitude of DC voltage, therefore, in such cases a higher voltage amplitude is necessary to observe a similar magnitude of magnetoelectric coupling effect at higher frequencies. The rise time can be measured by a simple assembly of a function generator and an oscilloscope as shown in Fig. 2.3.

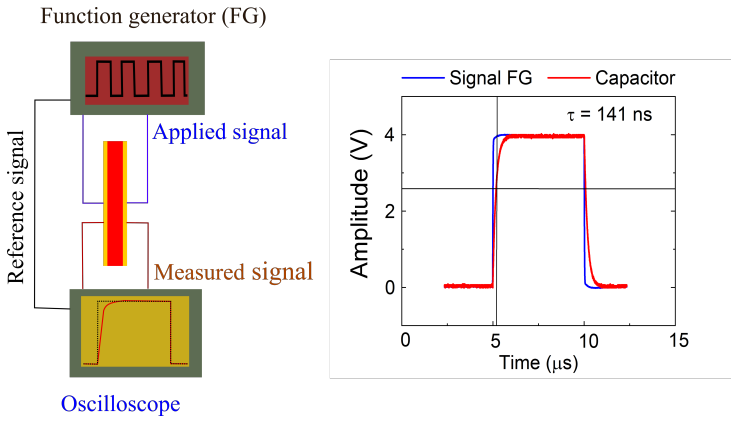

Figure 2.3: Rise time measurement schematic.

Similarly, a capacitor has a cut-off frequency, which is the maximum frequency, up to which the rise time is 63.2%, above the cut-off frequency the rise time is lowered. The cut-off frequency is given as $f_c = 1/2\pi RC$. Figure 2.4 shows the capacitance as a function of different cut off frequencies calculated keeping R as 50 Ω which is close to the combined measured resistance of the wires connecting the sample holder, sample and the measuring device. The values are kept as a reference to design the capacitive structures.

The permittivity of a dielectric material also changes with frequency (frequency dispersion). The change in permittivity is usually small (< 1 %) up to 100 MHz, however, significant changes can be observed above 100 MHz. Therefore, characterizing the permittivity variation as a function of frequency is important when designing devices for high frequency applications. Dielectrics such as SiO_2 or Al_2O_3 are used as capacitive structures in DDR4 RAM which can operate in GHz clock frequencies. For this thesis we considered a characterization frequency within 1 - 100 MHz, so as to avoid contributions from the frequency dispersion. Furthermore, at GHz frequencies, the wavelength of the applied signal is comparable to the dimension of the devices and in such cases, fabrication

of coplanar wave guides or a microstrip lines to the sample may be required; also, at such frequencies a conductor such as bonding wires, can also behave as an inductor which adds inductance in the circuit and making electrical characterization difficult.

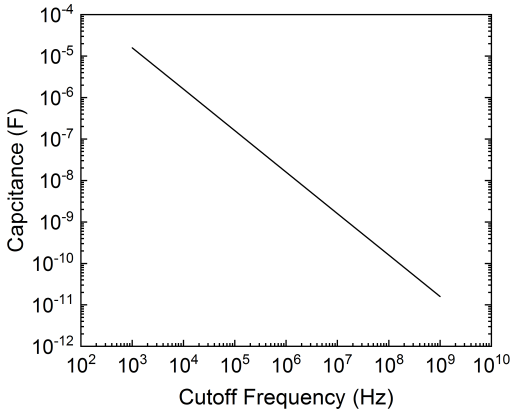

Figure 2.4: Reference plot of capacitance vs cutoff frequency, used for designing the capacitive structure.

It is clear that samples with shorter rise time are best for high frequency charaterization; which can be achieved by reducing the dielectric thickness. However, having a thin dielectric may not be suitable for strain-mediated coupling as the application of voltages is associated with the deformation of the crystal lattice. The duration of a deformation process is expected to be longer than the movement of charges across the capacitor. Therefore, along with the time response of the capacitor one should consider another parameter known as the thickness or volume fraction, defined as the ratio between the thickness of the ferromagnetic layer and sum of ferroelectric and ferromagnetic layer thickness. To have an effective strain-mediated coupling, the thickness of the layer causing the strain (ferroelectric) should be thicker than the interfacing material (ferromagnetic). An effective-strain mediated coupling can be obtained when the thickness of the ferromagnetic layer is about 20 - 30 % of the thickness of the ferroelectric layer [5]. It is the thickness fraction that determines the resonance frequency of the device, which is the frequency at which the change in magnetization of the ferromagnetic layer is equal to the ferroelectric distortion frequency [5]. Another parameter which is determined from the fabrication or design is known as the connectivity, which represents the dimensionality

of the two material components [75] [5]. For example, when a ferromagnetic component is embedded inside the ferroelectric media, and strain is created at the interfaces from all three dimensions from the ferroelectric media (eg. nanoparticle composites), then the connectivity is 3-0. In the coming chapters we discuss the results from strain and charge mediated multiferroic heterostructures and the possibility to perform high frequency characterization.

2.3.1 Domains and domain walls in magnetic thin films

This part is adapted from Ref. [76]. A single monodomain state has a high magnetostatic energy due to the large stray field, which can be minimized when the single domain is broken down into smaller domains throughout the volume to reduce the spatial extent of the demagnetizing stray field. Each domain has a different orientation of the net magnetic moment and the transition region from one domain to another is a magnetic domain wall. The domain wall also has an energy associated to it known as domain wall energy which is proportional to the exchange stiffness (exchange interaction) and the anisotropy energy.

There are two types of domain walls, Bloch and Néel walls. A Bloch wall is typically observed in thin films with out-of-plane (OOP) anisotropy while Néel walls are observed in thin films with in-plane (IP) magnetic anisotropy; a schematic of these domain walls is shown in Fig. 2.5. The type of domain wall is important for characterizing a skyrmion structure, as the DMI value and the topological nature is determined from the domain wall energy as described in the next section.

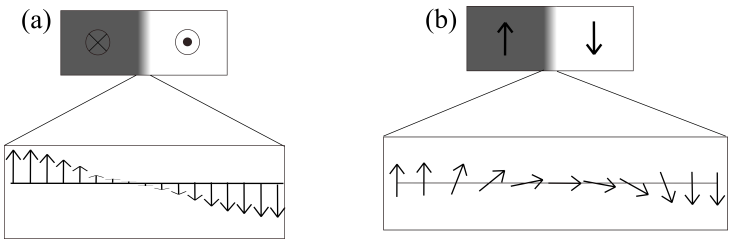

Figure 2.5: Types of domain wall (a) Bloch wall: where the spins make a rotation towards in-plane at the domain wall (b) Néel wall: where the spins rotate within the plane at the domain wall.

2.3.2 Skyrmions

Skyrmions are magnetic spin structures considered to offer better functionality for novel spintronic and storage devices owing to their topological nature which provides stability from defects and from external perturbations [77] [78] [79], small size, and ability to control with small current density. Skyrmions were theoretically predicted in 1989 [80] and confirmed experimentally in 2009 [81] [82] [83], and consist of chiral spin structures in a uniform perpendicularly magnetized surrounding. The formation of skyrmion depends on the local and non-local magnetization energy [76] [84] and they can be stabilized by an asymmetric exchange interaction such as the DMI [85] [86]. Skyrmions can also be observed in multilayer stacks with ferromagnetic layers interfaced between two different non magnetic metal layers, such as Pt or Pd, with a large spin orbit coupling (SOC). Such systems exhibit a broken interfacial inversion symmetry with a net DMI. In this case the DMI occurs between ferromagnetic and non-magnetic metal, leading to the formation and stability of skyrmions [87] [88] [89]. The topological nature of a skyrmion is determined by the type of domain wall from which the topological charge or number is calculated, the topological charge (Q), which quantifies the winding number of the skyrmion structure, defined as $Q = (1/4\pi) \int \mathbf{M} \frac{\partial \mathbf{M}}{\partial x} \times \frac{\partial \mathbf{M}}{\partial y} \cdot dxdy$, whose value vary between ± 1. From the DMI value the chirality of the skyrmion can be determined, left or right. More detailed information on calculating the topological charge can be obtained from ref. [90] [91] [92] [93]. Skyrmions can also be stabilized by the dipolar interaction [79]; such skyrmions are achiral (no left/right preference) but are still topological in nature. Skyrmions can exist in two types, of Bloch and Néel type (the schematic of the corresponding spin structures are shown in Fig. 2.6). A Bloch type skyrmion has a Bloch domain wall and inside the structure the spins are in-plane, forming a circular/spiral pattern. A Néel skyrmion is a circular spin structure formed in a dominant OOP anisotropy system with a Néel domain wall as described in the the schematic (Fig. 2.6), and both Bloch and Néel type skyrmions are chiral and topological in nature.

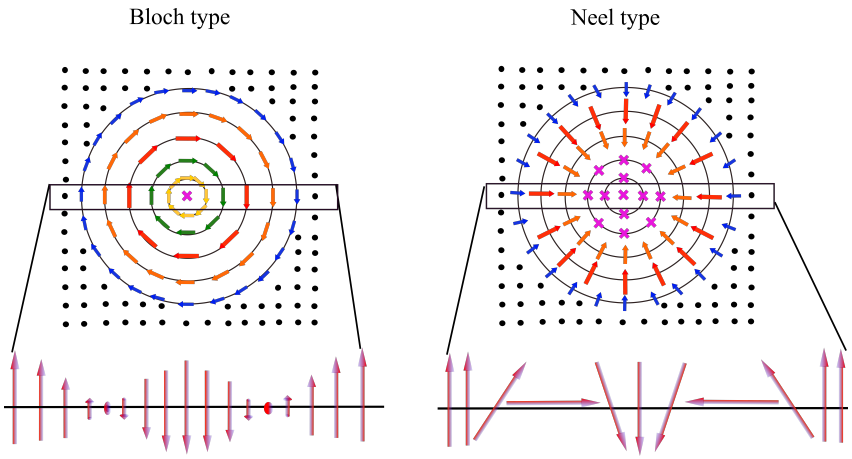

Figure 2.6: Types of Skyrmions. The black and dots pink crosses represent the OOP spins pointing up and down respectively. The coloured arrows represent IP spins. The bottom two images shows the cross section of the spins orientation indicated in the black box .

Circular magnetic bubbles can also exist with similar dimensions as skyrmions, therefore in order to differentiate between skyrmions from circular magnetic bubbles one must characterize the topological charge and the chirality [94]. Besides skyrmionic structures, chiral domain walls [95] [96] and inhomogenous cycloidal spin structures [97] were also reported and are topological in nature.

In the following chapter we discuss the sample preparation and characterizing techniques necessary to characterize the magnetoelectric coupling mechanisms.

Chapter 3

Sample preparation and characterization methods

In this chapter, an overview of the sample growth, lithography process and magnetic characterization used in this thesis will be discussed. Sample preparation plays a crucial part in the response/functioning of the multiferroic devices. In this thesis, we grew dielectrics such as Al_2O_3, AlN, ZnO, MgO; ferroelectric $BaTiO_3$ and ferromagnetic materials such Co, Fe, Ni along with electrical metallic contacts made of Cu or Au. The silicon nitride membranes used were commercially purchased. The ferromagnetic layers used in our devices should be at the appropriate thickness within an accuracy of < 0.5 Å for optimal magnetoelectric effect behaviour. Therefore, it is important to understand and optimize the growth process and use appropriate methods of deposition. The samples are fabricated using e-beam lithography and partly using photolithography. The magnetoelectric effect is characterized by measuring the changes in the magnetic properties as a function of the electric field. Magnetic characterization were performed using electrical, optical and X-ray based techniques.

3.1 Thin film deposition

Thin film deposition plays an important role in realizing a functional device. Advancements in thin film deposition technology to produce epitaxial and smooth interfaces made it possible to engineer artificial multiferroic heterostructures.

A thin film deposition process involves three steps: 1. Producing the appropriate species in its atomic, molecular or ionic form, for example, by heating the source material to its sublimation point; 2. Transporting the evaporated material to the substrate; and 3. Condensation of the evaporated material from the gaseous phase to solid as a thin film on the substrate by adsorption or by a chemical reaction. The condensation process may also involve nucleation or surface diffusion to form a perfect thin film. With this basic principle, a deposition process is divided into two types: 1. physical vapour deposition (PVD) and 2. chemical vapour deposition (CVD) [98]. PVD methods involve processes such as heating or bombarding the material with high energy atoms or electrons, while the CVD process involves one or more chemical reactions in the deposition process. In PVD techniques, the deposition is usually performed at low pressure; this allows the particles to travel within the chamber without a need for a transport process to carry the atoms towards the substrate. During the sublimation process, the evaporated atoms travel everywhere in a straight path from the source, the distance travelled by an atom without collision with itself or the residual particle at a given pressure is known as mean free path (λ_m) [99]. The mean free path of a molecule is given by the expression:

$$\lambda_m = \frac{RT}{\sqrt{2}\pi d^2 N_A p}, \tag{3.1}$$

Where R is the gas constant (8.3145 J/mol K), T is the temperature, N_A is the Avogadro's number, d is the diameter of the molecule and p is the pressure in mbar. The mean free path of ambient air can be approximated to the following expression

$$\lambda_m = \frac{6.65 \times 10^{-3}}{p} \quad (cm) \tag{3.2}$$

From (3.1) and (3.2), it is clear that the mean free path is inversely proportional to the pressure; for example, at a pressure of 6.65 $\times$ 10^{-5} mbar the mean free path is 1 m, while at 6.65 $\times$ 10^{-3} mbar the mean free path is 1 cm. Therefore, with a good vacuum the transportation process occurs by itself without the need for an additional transportation step. Furthermore, the presence of residual gases such as O_2 or CO_2 can result in a chemical reaction and in the formation of oxides or carbides. In particular for metal deposition, the base pressure should be as low as possible. In the following sections we give an overview of the different PVD techniques employed to grow materials used in this thesis.

3.1.1 Pulsed laser deposition

One of the types of multiferroic system studied in this thesis consists of heterostructures with Co or Ni grown on $BaTiO_3$ films. One of the several methods to grow $BaTiO_3$ is by pulsed laser deposition (PLD) [100]; in the PLD process the target material is thermally vaporized by a pulsed laser in a vacuum chamber with/without partially filled gases such as O_2 or N_2, due to which a plasma is generated along with the thermally ablated particles. These particles are then deposited on to a substrate which is usually heated to certain temperature to enhance surface diffusion and to obtain an epitaxial and stoichiometric film. Important parameters to be optimized include laser intensity, spot size and repetition rate. A schematic of the PLD system used in this project is shown in Fig. 3.1. The PLD depositions were carried out at the Laboratory for Mesoscopic Systems, ETH Zurich, Switzerland and the Laboratory for Multiscale Materials Experiments, Paul Scherrer Institut, Switzerland.

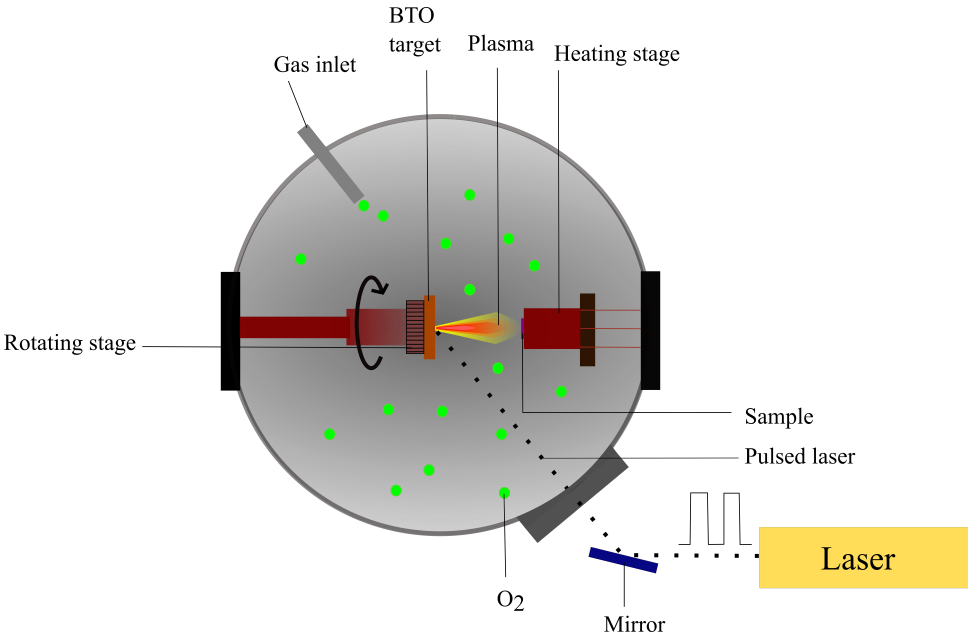

Figure 3.1: Schematic diagram of PLD set-up.

3.1.2 Thermal/e-beam evaporation

In the thermal evaporation process, the material is heated, for example, by passing a current through a tungsten boat containing the material to be deposited. For instance,

to deposit Cu, a current of about 6 A is required to reach the evaporation temperature of about 1000° C. A description of the thermal evaporation system (Balzers) used is shown in Fig. 3.2. Similarly, in the e-beam evaporation method, an electron beam with high acceleration voltage $\sim$ 5 - 10 kV is used to heat up the sample. Electrons are produced by thermionic emission and the high voltage is applied between the source and the sample, directing the electron beam to the source. Since the electron beam is localized, only a small portion of the source is evaporated. Both these methods were tested to grow magnetic heterostructure (Pt/Co/Pt), however, we found that the surface roughness was too high, which is required to have a good coupling at the interface, therefore the thermal evaporation method was used only to grow electrical contacts with materials such as Au, Cu, Cr.

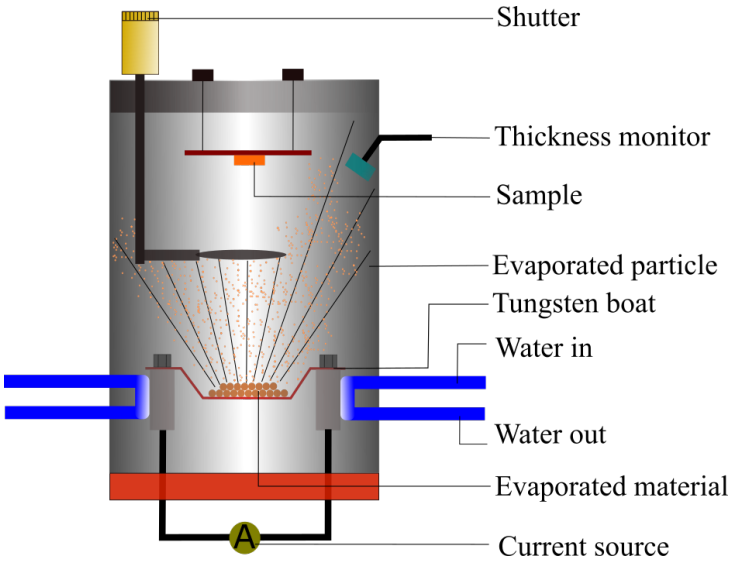

Figure 3.2: Thermal evaporation set-up.

3.1.3 Magnetron sputtering

In sputtering, the material is evaporated by kinetically knocking out atom by atom using other high energy neutral or ionised atoms [98]. There are many types of sputtering techniques, however, here we focus on magnetron sputtering. This method provides smooth and epitaxial films with good thickness accuracy; almost all magnetic metals (Co, Fe, Ni), metals (Pt/Ta) and dielectrics (Al_2O_3, AlN, MgO and ZnO) required in this thesis were deposited using this method.

Since a sputtering process involves bombarding the target material with high energy ionised particles, the trajectory of the emitted atoms depends on the collision trajectory of the incident ions, such as the angle or the kinetic energy. Therefore a controlled bombardment of ions on the target is necessary for a controlled evaporation and a optimal coating of a material on the substrate. A schematic of a sputtering system is shown in Fig. 3.3, where the inset shows a schematic of the target assembly where the sputtering process occurs. It consists of the target material, cathode, anode and a set of magnet(s). The process starts with emission of electrons between the cathode and the anode with an applied voltage, confined to the region defined by the magnetic field surrounding the target material created by the magnet. The chamber is filled with inert Ar gas, and when an Ar atom reaches the region of magnetic field, it ionizes to a positively charged Ar ion by loosing an electron due to collisions with a high energy electron; the Ar ion and electron between the cathode and anode results in the generation of a plasma. The positively charged Ar ions are then accelerated towards the target, which sits at a negative potential, guided by the magnetic field lines. The Ar ions bombard and remove the atoms from the target material and the ejected atoms flow towards the substrate. Finally, the positively charged Ar atom combines with another electron to form inert Ar once again.

Since a negative potential is required to be applied on the target material to attract the Ar^+ ion, the sputtering process on insulators is difficult. However, with sufficient plasma energy and/or higher potential applied on the target, it is possible to sputter insulating materials such as MgO, and in such cases, one may expect a much slower deposition rate. In order to grow metal oxides and nitrides, molecular oxygen and nitrogen can be introduced along with Ar, which lead to a reaction between the metal and the gas inside the chamber, and this process is known as reactive sputtering. AlN, Al_2O_3 and ZnO dielectric materials were synthesized by reactive sputtering in this thesis. The magnetron sputtering systems used for this thesis include a AJA ORION sputtering system at the Laboratory for Mesoscopic Systems, ETH Zurich, Switzerland and the Laboratory for Multiscale Materials Experiments, Paul Scherrer Institut, Switzerland; and a custom made magnetron sputtering system at the Laboratory of Neutron Scattering, Paul Scherrer Institut, Switzerland .

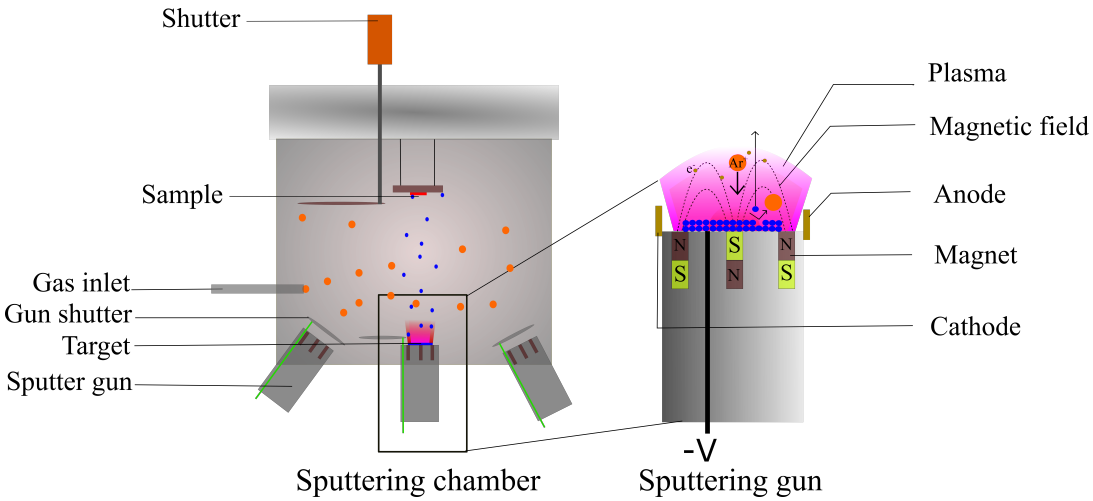

Figure 3.3: Schematic diagram of the sputtering deposition set-up.

3.2 Lithography

The next important process in making a device at micro and nano length-scales is the lithography step. In the past, lithography was used to define a printing process using a stamp or a cast. However, present-day lithography is used to create nano-scale 2D or 3D structures. A simple lithography process requires a photoresist and an illuminating light suitable to cause a chemical reaction on the photoresist. The nature of the photoresist determines the type of lithography and the quality of the structures produced after the lithography process.

A photoresist is usually a polymer material which is sensitive to electromagnetic radiation such as UV/visible light or to an electron beam; the reaction occurring in the photoresist depends on the type of photoresist and light used. There are two types of photoresists, positive and negative, corresponding to which part of the photoresist is removed/dissolved by a chemical, known as a developer, after the exposure to a radiation, a step known as development. If the developer dissolves the exposed region of the photoresist, it is called a positive photoresist; if the unexposed regions of the photoresist is dissolved, then the photoresist is a negative photoresist. In this thesis we used e-beam and UV light in our lithography process. Once the specified region is removed after development, the required material is deposited all over the surface including the region with left-over photoresist; after the deposition the sample is soaked in a solvent such

as acetone to remove the photoresist and the material on top of it leaving behind the material with the pattern on the substrate. This process is known as lift-off and is the last step of a lithography process.

A simple and a complete lithography process involves the following steps as described in Fig. 3.4:

1. Spin-coating with the required photoresist
2. Baking the photoresist to evaporate the solvents
3. Exposing the sample with appropriate electromagnetic radiation
4. Development process
5. Deposition of the appropriate materials
6. Lift-off

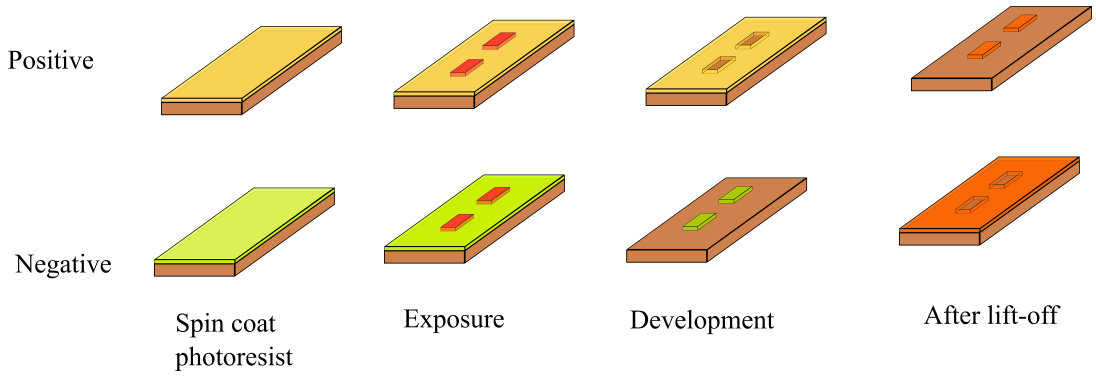

Figure 3.4: Schematic illustration of the lithography process.

3.2.1 E-beam lithography

Electron beam lithography involves raster scanning an electron beam with the desired pattern on the sample coated with photoresist. Common electron beam lithography photoresists include polymethyl metacrylate (PMMA), N-lof, Poly-hydrogen silsesquioxane (HSQ), etc. With electron beam lithography, one can pattern structures in the sub-10 nm range with higher energy electrons (100 keV). The electron beam spot can be focussed down to few nanometers, however, the actual beam spot is affected by dispersion of the electrons and interaction with the photoresist and the substrate, making the exposed region larger than the electron beam spot. The interaction of the electron beam with the

photoresist involves the following events [101] [102]:

1. Generation of secondary electrons: the incident electrons in the photoresist scatter with electrons from the polymer molecule, creating low energy secondary electrons through inelastic scattering; the inelastic mean free path of such secondary electrons varies with the energy of the incoming electron beam and can be typically between 10 - 20 nm. The generation of secondary electron is responsible for the chemical changes occurring in the photoresist. For example, PMMA has a high density of long polymer chain with strong cross links which are broken by the secondary electrons making the exposed region more soluble in the developing solution.

2. Forward scattering: besides producing secondary electrons, the high energy incoming electron beam can also undergo scattering over a large distance either in the photoresist or the substrate underneath; this process can result in exposure of regions deeper than the distance reached by secondary electrons.

3. Backward scattering: sometimes the scattering of electrons can be as high as 90° or the incoming electrons completely reflect back from the surface and also from the substrate resulting in passing though the region twice and doubling the exposure. Similar to the forward scattering process, backward scattering can also significantly affect the area being exposed with the given beam spot. A schematic of dispersion of electrons in an electron beam exposure is shown in Fig. 3.5(b).

A schematic description of the e-beam system is shown in Fig. 3.5(a). The principle of e-beam writing is similar to that of a scanning electron microscope (SEM), where the beam is deflected by the electrostatic deflectors and raster-scan on the sample with the desired pattern [Fig. 3.5(c)]. When fabricating a sample involving an insulating substrate it is necessary to coat the surface of the photoresist with a conducting layer to avoid charging of the surface, usually a thin layer of a metal film or a conducting polymer. Electron beam lithography was used for patterning most of the samples in this thesis using a Vistec 5000 Plus available in Laboratory for Micro and Nanotechnology (LMN) at the Paul Scherrer Institut.

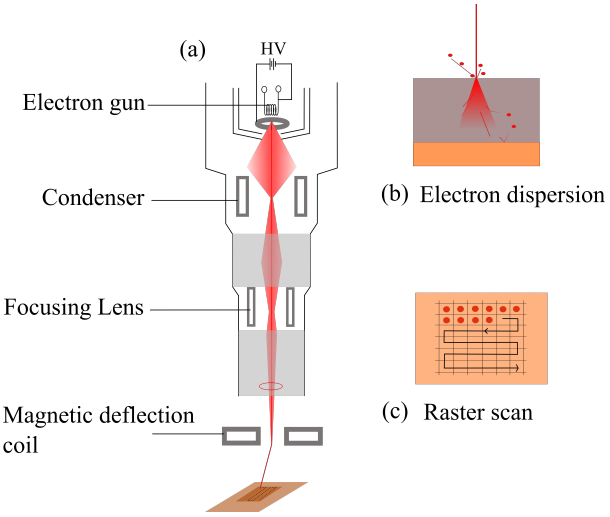

Figure 3.5: (a) Schematic diagram of the e-beam writer. (b) Electron dispersion as a result of scattering process within the photoresist. (c) Description of a raster-scan.

3.3 Magneto-optic Kerr effect (MOKE) characterization

MOKE characterization is a simple, sensitive and at the same time cost efficient magnetic characterization technique requiring only a source of light, a polarizer, an analyser and a light detector. When an electromagnetic wave interacts with a material, it can transmit, refract or reflect and, depending on the type of material, two optical phenomena can occur: (1) dichroism and (2) bifringence. When a material shows a difference in absorption for different light polarizations, the effect is dichroic; and when two different polarization of light propagate in a material at different velocities it is then bifringent. These two effects are not mutually exclusive and can occur simultaneously. The magnetic counterparts of these optical phenomenon are called Faraday and Kerr effects. MOKE referes to the change in the light polarization upon reflection from a magnetic surface, while Faraday effect refers to the change in the light polarization by transmission. Most MOKE set-ups use a visible wavelength laser as light source, for example at 632 nm wavelength, where the absorption length (λ) is in the order of few tens of nm depending on the material (usually larger for semiconductors), making MOKE a surface characterization technique. Since it measures the reflected light, reflective and smooth surfaces are

required. When a polarized light impinges on a magnetic media, one light component is partially absorbed which brings about a change in the ellipticity in the reflected wave known as Kerr ellipticity; the reflected wave also has a small phase shift between the two optical axis due to the magnetic bifringent effect, by which the polarized wave is rotated by a small angle known as Kerr rotation. The following description of interaction of light with matter is adapted from Refs. [103] [104]. The interaction of light with matter can be explained by a classical approach; we first start by defining the wave equation,

$$\nabla(\nabla.\vec{E}) - \nabla^2\vec{E} + \mu_0\mu(\sigma\frac{\partial\vec{E}}{\partial t} + \epsilon_0\epsilon\frac{\partial^2\vec{E}}{\partial t^2}) = 0, \tag{3.3}$$

with the solution of $\vec{E}$, given as;

$$\vec{E} = \vec{E_0}e^{(\vec{k}.\vec{r}-\omega t)} \tag{3.4}$$

where $\vec{E_0}$ is the amplitude, $\vec{k}$ is wave number, r is the position vector, ω is the angular frequency and t is the time. k is also related to the refractive index as $k = \omega n/c$. The components of $\vec{E}$ can be written as x and y components assuming that the wave is propagating in the z direction;

$$\vec{E}_x = \vec{E}_{0x}e^{(\vec{k}.\vec{z}-\omega t)}, \quad \vec{E}_y = \vec{E}_{0x}e^{(\vec{k}.\vec{z}-\omega t)} \tag{3.5}$$

A material related property is the displacement current ($\vec{D}$), given as,

$$\vec{D} = \epsilon_0(1-\chi)\vec{E} = \epsilon\vec{E}, \quad \vec{D} = \epsilon_0\vec{E} + \vec{P} \tag{3.6}$$

where ϵ_0 is the permittivity of vacuum, χ is the electric susceptibility and $\vec{E}$ is the electric field, $\vec{P}$ is the polarization and ϵ the permittivity tensor of the material. The origin of a magneto-optic effect arises from the interaction of the $\vec{E}$-field vector with the $\vec{D}$ vector. The $\vec{D}$ vector represents the direction of the electron oscillation caused by the incident wave, and thus determines the direction and the amplitude of the transmitted or reflected wave. The permittivity tensor for a medium is written by the following expression,

$$\epsilon = \epsilon_0 + \epsilon_{br} + \epsilon_{op} \tag{3.7}$$

Where ϵ_0 is the permittivity of the isotropic media, ϵ_{br} is the permittivity of the bifringent part and ϵ_{op} is the permittivity of the optical activity part (such as the interaction of

magnetic moment with $\vec{E}$ vector). The permittivity tensor for an isotropic medium has zero non-diagonal elements, but this is not the case for anisotropic media such as a magnetic medium. The dependence of permittivity on magnetization is usually small and can be described in terms of a linear magneto-optic effect and additional quadratic terms;

$$\epsilon = \epsilon_{ij}^{0} + \sum_{K=1}^{3} K_{ijk} m_k + \sum_{K=1}^{3} \sum_{l=1}^{3} G_{ijkl} m_K m_l, \tag{3.8}$$

where K is first order magneto-optic tensor, G represents components of quadratic magneto-optic tensor with rank 4, and both of these terms have components connecting the magnetization of the material and the permittivity of the medium.

As an example, from (3.8) one can deduce the permittivity tensor for a cubic crystal and the permittivity tensor with the appropriate unit vector of magnetization; the final expression for the permittivity as a function of magnetization is described;

$$\epsilon = \epsilon_{iso} \begin{pmatrix} 1 & -iQ_v m_3 & -iQ_v m_2 \\ iQ_v m_3 & 1 & -iQ_v m_1 \\ iQ_v m_2 & -iQ_v m_1 & 1 \end{pmatrix} + \begin{pmatrix} B_1 m_1^2 & B_2 m_1 m_2 & B_2 m_1 m_3 \\ B_2 m_1 m_2 & B_1 m_2^2 & B_2 m_2 m_3 \\ B_2 m_1 m_3 & B_2 m_2 m_3 & B_1 m_3^2 \end{pmatrix} \tag{3.9}$$

The first part represents a linear term (gyroelectric quantities - bifringent/Kerr rotation), where the quantity Q_v is the Voigt magneto-optic constant, which is a material parameter describing the linear magneto-optic effects. The second expression is the quadratic term describing intrinsic magneto-optic effects such as the dependence of magneto-optic effect on crystal structure. B1 and B2 are called as intrinsic Voigt magneto-optic constant which depends on the crystal structure of the material and frequency [105].

By combining (3.3) and (3.9) one can obtain the solution for the propagation vector for refracted and reflected light; the complete derivation of the solution can be found in [104]. It is assumed that the magnetization and light propagation vector are in the same direction, it can be shown that the E_x and E_y component of the transmitted wave has a phase difference of $\pi/2$, which describes that a linear polarized light becoming a circular polarized light. Since the linear polarized light becomes circular polarized under transmission it can also be shown that there exist different refractive indices for left and

right circular polarization given by the following expression,

$$n_{\pm} = \sqrt{\epsilon_{iso}}(1 \pm Q_v/2) \tag{3.10}$$

This expression corresponds to a dichroic or bifringent effect from a macroscopic point of view and this phenomenon is valid for all wavelengths of the electromagnetic spectrum as long as the $\vec{E}$ field interacts with the $\vec{D}$ vector. This phenomenon can also be observed for example in X-ray dichroism which will be discussed in the next section. When the $\vec{E}$ vector undergoes a reflection as in MOKE, it can be shown that the reflection coefficient is also dependent on the refractive index and the polarization by the following expression:

$$r_{n_{\pm}} = \frac{1 - n_{\pm}}{1 + n_{\pm}} \tag{3.11}$$

Therefore, in an anisotropic magnetic medium with permittivity tensor having non-zero non-diagonal elements, one can expect the $\vec{E}_x$ and $\vec{E}_y$ to have different velocities. When an elliptical/linear polarized light interacts with a magnetic material there can be a phase difference between $\vec{E}_x$ and $\vec{E}_y$ resulting in a rotation of $\vec{E}$ from the principal axis before interaction and this effect is the circular bifringent effect (Kerr rotation), when the amplitude of E_x and E_y change due to an absorption process then it is known as circular dichroism effect (Kerr ellipticity). A schematic of both effects is shown in Fig. 3.6(b). When bifringent and dichroism occur in transmission, the process is called Faraday effect and in reflection it is called Kerr effect. So far it was assumed that the propagation vector of the incident light is in same direction as the magnetization but a more general dependence of Kerr effect on the incident light polarization direction and magnetization can be derived from the magneto-optic tensor (3.9). However, a simpler description based on the Lorentz velocity concept can be used to describe such dependence. By combining (3.6), (3.9) and rewriting the expression one can obtain,

$$\vec{D} = \epsilon_0 n^2[\vec{E} + iQ_v(\vec{m} \times \vec{E})] \tag{3.12}$$

Where the term $\vec{m} \times \vec{E}$ determines the Lorentz velocity associated with the propagating wave in transmission or in reflection. When the $\vec{E}$ vector is perpendicular to the magnetization vector, we get a velocity orthogonal to $\vec{E}$ and $\vec{m}$ and thus giving the maximum

rotation and higher sensitivity in measurements; this case is called polar configuration, suitable to measure the out-of-plane magnetization. To probe the in-plane components, the $\vec{E}$ vector should be incident at a grazing angle, the higher the grazing angle the more the rotation of the reflected light and the higher the sensitivity for the in-plane component (with a small grazing angle of incidence one probes both in-plane and out-of-plane magnetic moments); this configuration is called longitudinal configuration. In this thesis we use polar and longitudinal configurations to measure out-of-plane and in-plane magnetization respectively.

3.3.1 MOKE setup

In MOKE one can experimentally determine the Kerr rotation and ellipticity. With Kerr rotation one can expect a change in the polarization angle by 0.05° - 0.1°; in order to measure such small changes, a photoelastic modulator and a lock-in amplifier (LIA) is used. A description of the optical setup for longitudinal configuration to measure IP magnetization used in this thesis is shown in Fig. 3.6(a).

A linear polarized light beam impinges the magnetic material (normal or grazing angle) and, upon reflection, acquires a new rotation and ellipticity; the light then passes through a photoelastic modulator (PEM), which adds time modulated phase shift with a frequency which is then used as a reference signal for the LIA. After the PEM, the light passes through another polarized (analyzer) which is kept at 45° angle with respect to the first polarizer which determines the intensity of the light reaching the detector. The measured intensity has Kerr rotation and ellipticity components given by:

$$I(t) = I_0[1 + 2\theta_k \cos(A_0\omega t) - 2\epsilon_k \sin(A_0\omega t)] \tag{3.13}$$

where $I(t)$ is the intensity at the detector, measured by the LIA, I_0 is the DC intensity, θ_k is the Kerr rotation, ϵ_k is the Kerr ellipticity, $\omega = 2\pi f$ is the angular frequency, and A_0 is the retardation amplitude induced by PEM. Expanding the term with Fourier series, we get,

$$I(t) = I_0[1 + 2\theta_k J_0(A_0) - 4\epsilon_k J_1(A_0)\sin(\omega t) + 4\theta_k J_2(A_0)\cos(2\omega t)] \tag{3.14}$$

where J_n is the Bessel function of n^{th} term, and by setting the A_0 value to 2.405 rad, the second term (with J_0) goes to zero, by adjusting the harmonics in LIA one can obtain

the direct measure of the Kerr rotation and Kerr ellipticity.

$$\theta_k = \sqrt{2}V_{2f}/4J_2V_{DC} \tag{3.15}$$

$$\epsilon_k = \sqrt{2}V_{1f}/4J_1V_{DC} \tag{3.16}$$

V_{1f} and V_{2f} are the output voltage from the LIA, J_1 and J_2 can be calculated by expanding the Bessel function, whose values are 0.51915 and 0.43175 repectively (only if $A_0 = 2.405$ rad). The value of V_{DC} normalizes the signal and cancels out any intensity fluctuations from the light source. By measuring the rotation and ellipticity as a function of a sweeping magnetic field one can obtain a ferromagnetic hysteresis loop. A detailed description on this set-up can be found in Ref. [106]. The MOKE measurements for this thesis were carried out using a custom built MOKE set-up at the Surface/interface microscopy beamline, and the Durham Magneto Optics NanoMOKE3(R) system of the Laboratory for Mesoscopic Systems, ETH Zurich, Switzerland and the Laboratory for Multiscale Materials Experiments, Paul Scherrer Institut, Switzerland.

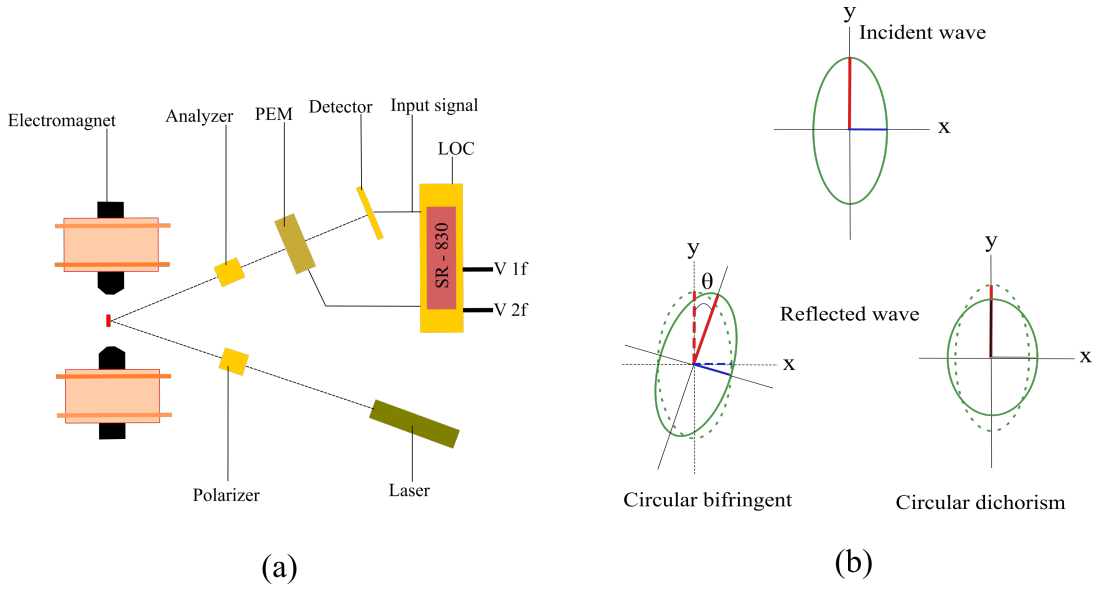

Figure 3.6: (a) Schematic illustration of longitudinal MOKE set-up. (b) Description of dichroic and bifringent effects.

3.4 X-ray characterization

Part of the description on synchrotron radiation described below was adapted from Ref. [107], where a detailed description of synchrotron physics is provided. X-ray characterization is a powerful tool as one can obtain information on structural, chemical and electronic states of a material down to the atomic level. In order to perform such detailed characterization, high quality X-ray sources with high brilliance and energy resolution are necessary which are not possible to achieve with a laboratory X-ray source. Therefore, such requirements led to the commissioning of synchrotron facilities. A schematic of the key components of a synchrotron is shown in Fig. 3.7. Most of the synchrotrons can produce photons with wavelengths from infrared (700 nm) to hard X-ray (0.1 Å) radiation and the energy can be tuned according to the experimental requirements. The starting point to create a synchrotron radiation is to produce electrons, usually by thermionic emission; then the electrons are accelerated by a linear accelerator and then in a booster ring, once the electrons have reached enough velocity, they are diverted to a storage ring to produce synchrotron radiation. The acceleration and focussing of electrons inside the storage ring is carried out by applying a strong magnetic field (> 1 T) from quadrapole, sextapole and bending magnets along with a Klystron and radio frequency microwave cavities.

Accelerated particles emit electromagnetic (EM) radiation (synchrotron radiation), when it is accelerated close to the speed of light the emitted radiation is elongated resulting in a collimated beam in the direction of motion as shown in Fig. 3.7 (marked in the red box). At certain regions of the storage ring there are bending magnets used to accelerate the electrons towards the center to make a circular path. At these regions the electron makes a curved path, resulting in the emission of synchrotron radiation tangentially towards the beamlines. Inside the storage ring the radiation produced by the electrons is polychromatic; monochromatic, high intense, coherent radiation can be obtained using insertion devices; such types of devices include wigglers and undulators.

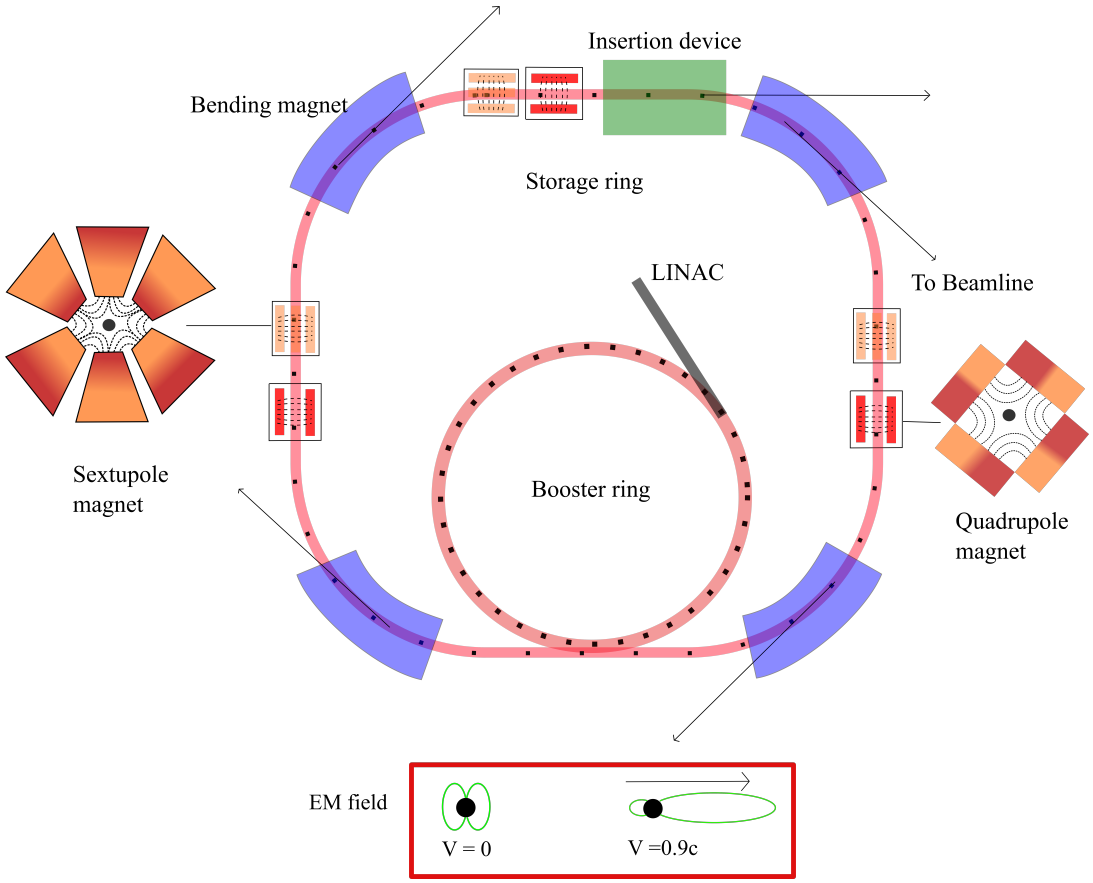

Figure 3.7: Schematic representation of a synchrotron facility.

Undulators consist of a large number of magnets arranged in alternative polarity similar to the schematic shown in Fig. 3.8. When electrons pass through an undulator, they are subjected to a sinusoidal path over the entire length of the undulator, being accelerated at every magnetic pole; this process leads to emission of radiation at each curve of the sine wave resulting in a highly intense and coherent radiation produced in the propagation direction. An undulator can be configured to produce fully polarized coherent photons. One type of undulators where the polarization can be effectively controlled are Advanced Planar Polarized Light Emitter (APPLE); a description of different configurations of such undulators and the corresponding polarization produced is shown in Fig. 3.8. A bending magnet also emits X-ray light, with different light polarizations at different solid angles. However, the light obtained from a bending magnet is not coherent and is less intense.

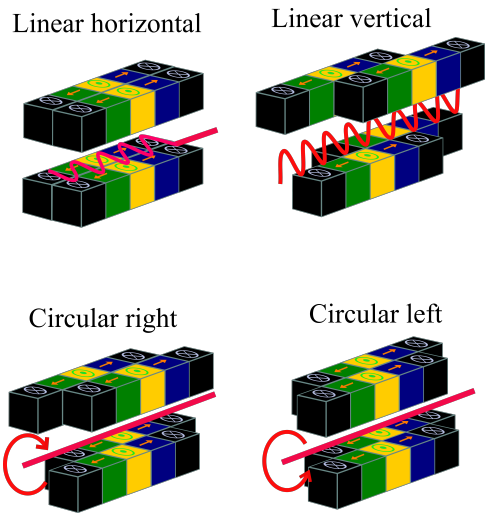

Figure 3.8: APPLE undulators.

XMCD effect

The description of the XMCD effect described here is adapted from Ref. [108]. The concept of magnetic circular dichroism in visible light was briefly introduced in the previous section. Here we discuss X-ray magnetic circular dichroism, which describes the microscopic origin of the magneto-optical effect due to the difference in absorption between two different circular light polarizations at absorption edges [109] [110] [111]. Absorption edges correspond to changes in light absorption when the photon energy equals the binding energy of core shell electrons, at which a sudden increase in the absorption of X-rays occurs. An absorption process results in an electron transition from a core shell to a higher energy state above the Fermi level. The electron transition from a lower energy state to a higher energy state is determined by (i) transition probability given by the Fermi's Golden rule, which describes the probability of a transition from initial to the final state, (ii) dipole selection rules which define the allowed and the forbidden transitions in an absorption process. Similar absorption processes can also occur when using visible light; however, with visible light, the asymmetry in the absorption is very small or non-existent compared to X-ray absorption, since an excitation of visible light can result in different electronic transition as it is not tuned to particular absorption edges. When an absorption of X-rays is measured over a wide range of X-ray photon energies it is known as an absorption spectrum. The X-ray absorption can be measured by three methods:

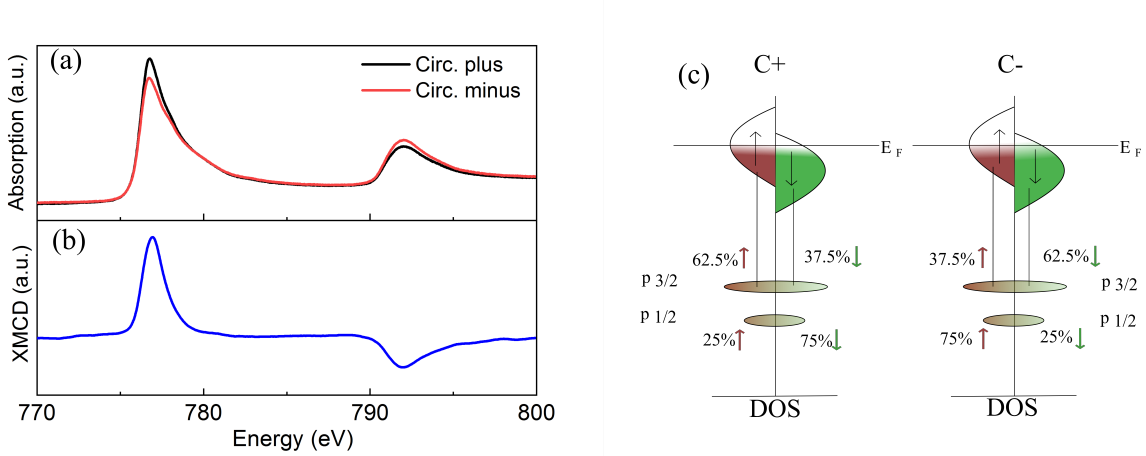

Figure 3.9: (a) XAS of C_+ and C_- polarization indicating the dichroic effect at the absorption edges. (b) XMCD spectra obtained from (a), by dividing the difference of the difference and the sum of C_+ and C_- polarization. (c) Schematic of electron transition of a magnetic material with different light polarization, the coloured region and white region represent occupied and unoccupied states respectively.

1. by measuring the transmission of X-rays through the sample if the sample is thin enough; 2. by measuring the drain current; or 3. by measuring the intensity of emitted photons due to fluorescence. An example of the dichroic effect observed from the X-ray absorption spectroscopy (XAS) of C_+ and C_- polarization obtained by measuring the drain current at X-treme beamline for Pt/Co/Pt heterostructures is shown in Fig. 3.9(a). The absorption spectra in the energy range from 770 eV to 825 eV is measured separately for C_+ and C_- light polarization; at 779 eV and 788 eV corresponding to Co L_3 and L_2 edges respectively, one can observe a difference in the X-ray absorption intensity. Fig. 3.9(b) shows the XMCD spectrum from which one can quantify the spin and orbital moments of the atoms of the magnetic material using sum rules [112]. The L_3 and L_2 edge resonance energies result in excitation of 2p electrons to empty $3d$ states, which is particularly suitable for measuring the magnetic properties of $3d$ transition metals, since in these systems magnetism is determined by the $3d$ electrons. Similarly, for $4f$ magnetic materials, energy corresponding to M shell binding energy can be used which results in a transition from the M shell to f states.

The details of the derivation of the XMCD effect can be found in [108] [113] [114]; it

can be described using a simple two step model. The p shell electrons have two energy levels ($p_{3/2}$ and $p_{1/2}$) due to the spin orbit coupling, resulting in different total angular momenta (J); which corresponds to the L_3 and L_2 edges. In the first step, a circular plus polarized photon with angular momentum $+q\hbar$ excites a p shell electron, with the angular momentum transferred to the orbital angular momentum of the electron. The change in the angular momentum changes the magnetic quantum number ($m_j = +J$ to $-J$ with integer steps). For the L_3 edge it can be shown that the change in magnetic quantum number can result in a transition probability of spin up electrons of 62.5 % and spin down electron of 37.5 % as determined from the Fermi's Golden rule and the dipole selection rules. Similarly, for the L_2 edge, the excitation probability is 25 % for spin up and 75 % for spin down, schematic of the transition probability with light polarization is shown in Fig. 3.9(c).

The second step in the XMCD process involves the transition to the final state at the empty d-shell; magnetic materials (Co, Ni or Fe) have different density of states for spin up and spin down electrons at Fermi level due to the exchange interaction. When the density of spin up electrons are higher, a higher absorption of C_+ light in L_3 edge follows, as it excites more spin up electrons, and in L_2 edge the absorption will be less with C_+ light, as more spin down electrons are excited. The opposite effect occurs with C_- polarization, which explains the difference in the absorption at the L_3 and L_2 edges with different light polarizations [Fig. 3.9(b)].

Similar to the Kerr effect, one can obtain the maximum XMCD effect when the X-ray propagation vector is in the same direction as the magnetization; if the X-ray propagation vector is orthogonal to the magnetization vector, there is no dichroism. The dichroic effect varies as the cosine function of the magnetization direction and X-ray propagation.

3.4.1 Imaging magnetic domains using XPEEM

One can also perform spectro-microscopy, where a spatially resolved absorption spectrum of the sample can be obtained. A schematic description of the XMCD spectra/image obtained from a sample with different local magnetization acquired in a detector is shown in Fig. 3.10.

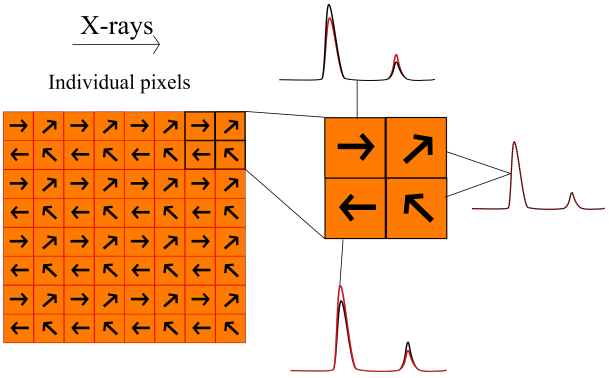

Figure 3.10: Schematic description of spatially resolved XMCD spectrum as a function of local magnetic moment.

One such technique is X-ray photoemission electron microscopy (XPEEM) where one can obtain a spatial resolution down to 30 nm [115]. Photoemission involves the excitation of the sample using photons such as X-rays or UV light; after the absorption process, an electron from a higher energy state fills up the core hole by emitting a photon (fluorescence) or an Auger electron which in turn can produce secondary electrons [116] [108]. The Auger or secondary electrons are then extracted from the surface by applying a high voltage from the sample towards the microscope. A schematic of the ELMITEC PEEM is shown in Fig. 3.11. Once the photoelectrons are extracted from the sample, they pass through a series of lenses for image magnification. The energy analyzer separates the electrons according to their kinetic energy by making the electrons with high kinetic energy to make a larger curvature than the ones with lower kinetic energy, thereby reducing the chromatic aberration. After the energy analyzer the final set of lenses directs the electrons towards a micro-channel plate (MCP). A MCP is an electron multiplier device which amplifies the photoelectron signal. After passing through MCP the electrons reach a phosphorus screen, and the light produced is imaged by a charge-coupled device (CCD) camera. At the detector, one can obtain a magnified image of the sample from the emitted photoelectrons and determine the local absorption from the image intensity.

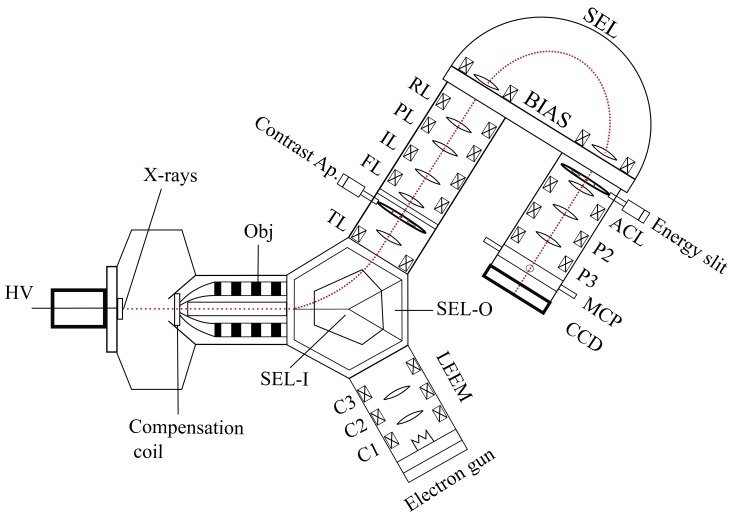

Figure 3.11: ELMITEC XPEEM set-up.

By using circular polarized light, one can obtain XMCD spectra (Fig. 3.10) or magnetic contrast images. For acquiring images, the photon energy is tuned to the L_3 or L_2 edge, and images with C_+ and C_- polarization are acquired separately; by performing the mathematical operation $(C_+ - C_-)/(C_+ + C_-)$ one can obtain the XMCD asymmetry value of individual pixels, which corresponds to the projection of the local magnetization with respect to the X-ray propagation direction. A magnetic contrast image obtained using XPEEM is shown in Fig. 3.12.

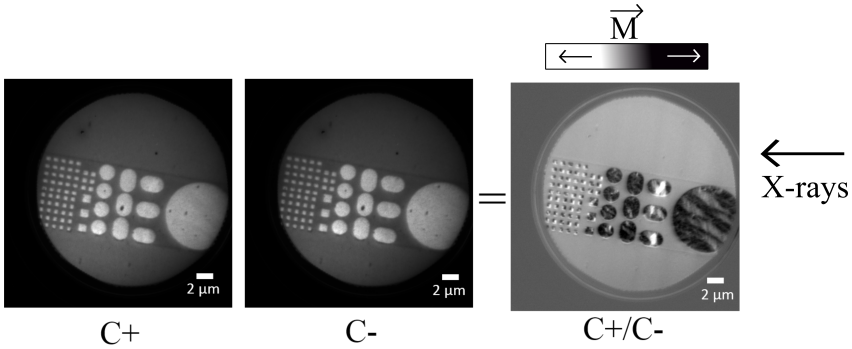

Figure 3.12: Magnetic contrast image obtained from C_+ and C_- polarization.

In this thesis we employ XPEEM for characterizing the magnetic domains and spin structure with sub 100 nm resolution in order to obtain a deeper insight of the magnetic effects happening at nm scale. The X-ray characterization was performed at the Surface/Interface: Microscopy (SIM) beamline [117] and at X-Treme beamline [118] at Swiss

Light Source, Paul Scherrer Institut. All the XPEEM measurements in this thesis were carried out at room temperature and under ultra high vacuum of $< 10^{-10}$ mbar. The XPEEM is equipped with high voltage power supply, and the sample holders have electrical contacts and an electromagnet, making it possible to apply electric and magnetic fields *in situ* [119]. Besides, the XPEEM is also suitable to perform time resolved pump and probe characterization [120].

Chapter 4

Exploration of strain mediated coupling for high frequency characterization

In this chapter we show the presence of strain mediated magnetoelectric coupling in $BaTiO_3$/Ni and $BaTiO_3$/Co heterostructures using X-ray photoemission electron microscopy (XPEEM). We optimized the $BaTiO_3$ deposition process and developed an appropriate fabrication method compatible for XPEEM characterization. We observe large changes in the magnetic spin structures in both Ni and Co structures. Despite the presence of a coupling, the lack of reproducibility in the control of the magnetization made the sample not suitable for time resolved characterization. In the last section we propose ways to improve the sample quality and other possible strain mediated coupling systems.[1]

[1]For this project, the $BaTiO_3$ was deposited by Dr. Nicolas S. Bingham, Dr. Milan Radovic, Dr. Stefan Muff and myself. The Lithography was carried out by Dr. Carlos A.F. Vaz and myself. The XPEEM characterization was carried out by Dr. Carlos A.F. Vaz, Dr. Ludovic Howald, Mr. David Bracher and myself. The atomic force microscopy characterization was performed by me.

4.1 Strain mediated coupling in ferromagnetic/$BaTiO_3$ heterostructures

Strain mediated magnetoelectric coupling provides a simple approach to control magnetism. In a well optimized system the changes in the magnetizition occur not just in a few atomic layers of the interfacing ferromagnetic material but up to 20 nm thickness or more. To realize a device with strain mediated coupling one requires a material that can change its dimension with electric field in contact with a ferromagnetic material. Many types of ferroelectric/ferromangnetic and piezoelectric/ferromagnetic exhibiting a strain mediated coupling [47] exist, and it has also been demonstrated in micro-electro-mechanical systems (MEMS) [121] [122]. Therefore, due to the simplicity in the sample preparation, strain mediated coupling phenomenon can be a good starting point to perform high frequency characterization. Many studies have shown the presence of strain mediated coupling with a ferroelectric being used as a substrate, which requires applying high voltages (sometimes 1000 V) to create the necessary strain. Hence, performing high frequency characterization in a ferroelectric substrate is difficult due to higher RC time constant as mentioned in chapter 2. Therefore, we considered depositing the ferroelectric films with the required thickness, the necessary rise time and cut off frequency. We use ferroelectric $BaTiO_3$ which has been extensively analysed, and capable of inducing significant strain at the interfacing ferromagnetic material.

Ferroelectric materials have very high permittivity and possess a spontaneous polarization. The presence of spontaneous polarization is due to the arrangement of ions within the unit cell. The application of the electric field move the ions and change the cell structure, hence ferroelectric material also exhibit piezoelectric effects. Ferroelectric $BaTiO_3$, used in this thesis, has a perovskite structure with cubic unit cell, however, in the polarized state, the unit cell is tetragonal as a consequence of the Ti ion displacement. A schematic of a polarized $BaTiO_3$ unit cell is shown in Fig. 4.1.

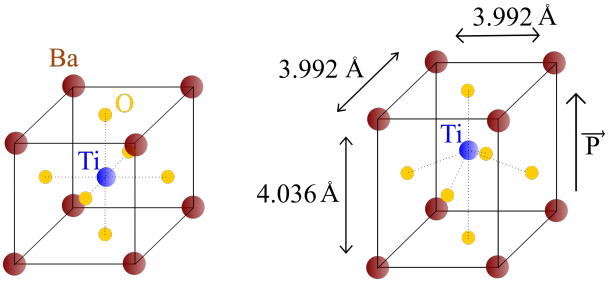

Figure 4.1: Schematic of $BaTiO_3$ in the unpolarized and polarized state.

In order to obtain the required ferroelectric/piezoelectic property, the deposited $BaTiO_3$ has to be in a crystalline (perovskite) form, therefore it is necessary that the deposition is made on a structurally similar substrate; we used perovskite $SrTiO_3$ as our substrate which has a comparable lattice constant as $BaTiO_3$. It has been demostrated by first principle calculation that a tetragonal phase of (001) oriented $BaTiO_3$ can be stabilized by the misfit strain with $SrTiO_3$ (001) [123] [124] [125] [126] and a buffer layer of $LaSrMnO_3$ before $BaTiO_3$ deposition can improve the epitaxy.

Commercially available single crystal (001) oriented $BaTiO_3$ substrate with ferroelectric domains have spontaneous polarization in-plane (IP) direction, and with an OOP electric field the IP polarization rotates IP by 90° or change from IP to OOP [57]. On the interfacing ferromagnetic material, the (001) orientation provides a biaxial strain (ϵ) in the $a-b$ plane of $\pm 1.1\%$. Therefore, for multiferroic structures with (001) oriented $BaTiO_3$ a bottom conducting electrode is required to form the capacitive structure, and conducting perovskite such as $LaSrMnO_3$ can be used. However, a thin $LaSrMnO_3$ conducting layer (about 20 nm) may have a large resistance, resulting in a large RC time constant for high frequency characterization, while with any other metal the $BaTiO_3$ may not have the perovskite structure. To solve this issue, we use electrodes in the IP geometry such that the $BaTiO_3$ can grow in between the electrodes forming the capacitive structure and still maintain the crystallinity. However, an applied IP electric field on (001) oriented $BaTiO_3$ will not result in a similar strain at the interface as obtained by applying an OOP electric field. Therefore, we considered to grow $BaTiO_3$ in (110) orientation. With the (110) orientation, the spontaneous polarization lies in-plane at [110] or [011] direction, and with the application of an IP electric field; similar magnitude of strain can be induced at the interface as in the case of (001) orientation. The values of the

strain caused by deformation in different direction (Δ = [original dimension - modified dimension]/original dimension) at the interface by (001) and (110) oriented $BaTiO_3$ as a function of change in polarization is summarized in Fig. 4.2 and Fig. 4.3, respectively.

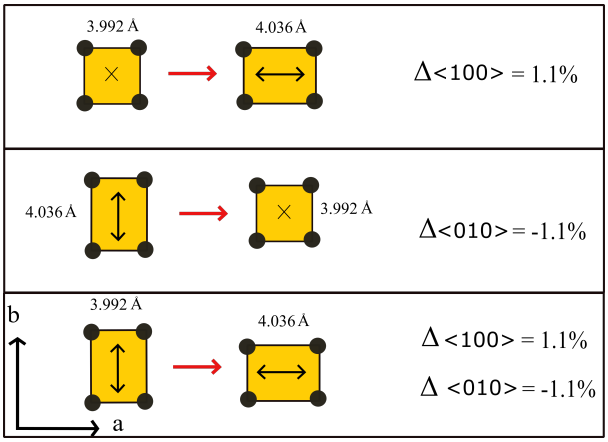

Figure 4.2: Deformation created by the change in polarization at the surface of (001) $BaTiO_3$ orientation which can lead to an interfacial strain.

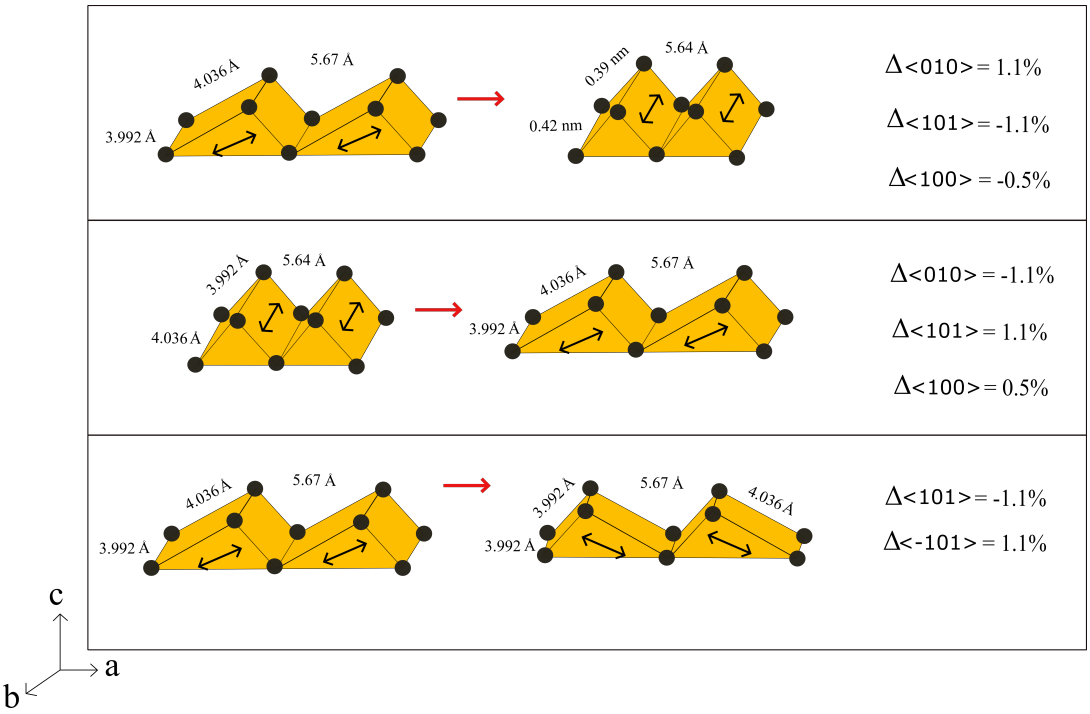

Figure 4.3: Deformation created by the change in polarization at the surface of (110) $BaTiO_3$ orientation leading to an interfacial strain.

4.1.1 Fabrication of $BaTiO_3$ heterostructures

$SrTiO_3$ (110) substrates were purchased from CrysTec GmbH. The substrates were cleaned with acetone and isopropyl alcohol before fabrication. The devices were fabricated using a four step lithography process as shown in Fig. 4.4. In the first step we pattern the electrodes by e-beam lithography, the thickness of Pt electrode is 50 nm and is deposited by magnetron sputtering. The distance between the two electrodes is kept at 5 μm, 10 μm and 15 μm, exposing the $SrTiO_3$ substrates for the $BaTiO_3$ to grow in crystalline form. In the second step, we deposit a 200 nm $BaTiO_3$ continuous layer using pulsed laser deposition at a substrate temperature of 700 °C, at a pressure of 10^{-4} mbar of O_2. Initial tests were performed to verify the stability of Pt structures on $SrTiO_3$ with temperature and we find that they were intact up to 900°C. The laser fluence used is 2.3 J/cm^2 and the repetition rate is kept at 3 pulse per second with the target $BaTiO_3$ rotating at 10°/s. Since the $BaTiO_3$ also covers the Pt contact pads necessary for the electrical contacts, the $BaTiO_3$ on top of the contact pads is removed by scratching with a diamond tip; in the third step we use e-beam lithography to pattern regions for the metal contacts in the regions where $BaTiO_3$ was scratched, consisting of 80 nm thick Au deposited by thermal evaporation. In the last step we pattern the magnetic islands in the middle of the Pt electrodes. On a single $SrTiO_3$ substrate about 10 capacitive devices were fabricated which were individually wire bonded to the XPEEM sample holder as illustrated in Fig. 4.5.

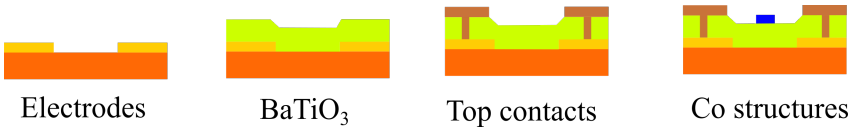

Figure 4.4: Schematic of $BaTiO_3$/Co heterostructure fabrication.

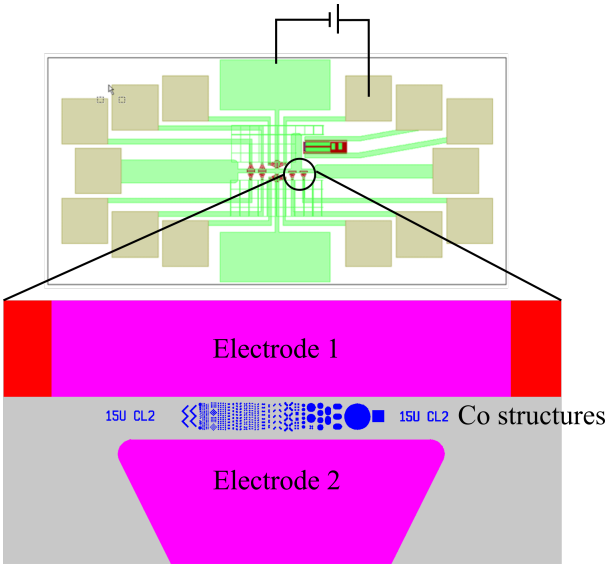

Figure 4.5: Schematic of the final fabricated sample with $BaTiO_3$/Co heterostructure.

The rise time of the lateral capacitive structure formed by Pt/$BaTiO_3$/Pt with gaps of 5 μm, 10 μm and 15 μm was found to be 3.3 ps, 1.6 ps and 1.1 ps respectively; keeping the electrodes wide apart reduces the possibility of leakage current.

We have also considered a simpler fabrication step which involved growing a continuous $BaTiO_3$ film first on $SrTiO_3$ and then carrying out the remaining fabrication process mentioned before and summarized in Fig. 4.4. However, measuring such types of devices in XPEEM resulted in many discharges due to the presence of sharp edges, damaging the sample. Covering the electrodes with $BaTiO_3$ resulted in less discharges and was better suited for XPEEM characterization.

4.1.2 XPEEM characterization of Co/$BaTiO_3$ and Ni/$BaTiO_3$

The fabricated sample was then mounted on an XPEEM sample holder with electrical contacts and an electromagnet used to apply magnetic fields *in situ*. The measurements were carried out at room temperature and under ultra high vacuum ($< 9 \times 10^{-10}$ mbar). Two different samples (i) Co (20 nm)/$BaTiO_3$ and (ii) Ni (20 nm)/$BaTiO_3$ were characterized. Sequences of X-ray magnetic circular dichorism (XMCD) images were acquired at the Co and Ni L_3 edges, respectively, and averaged to obtain a better signal to noise ratio. The elemental contrast and the initial XMCD image of the Co and Ni magnetic

structures are shown in Fig. 4.6 and Fig. 4.7, respectively. We find that the magnetic structures are unoxidized and have a multidomain state. Magnetic structures whose lateral dimension is < 300 nm do not show any magnetic contrast, as their magnetic moments fluctuate in the XMCD image sequence and appear with a grey contrast in the averaged XMCD image.

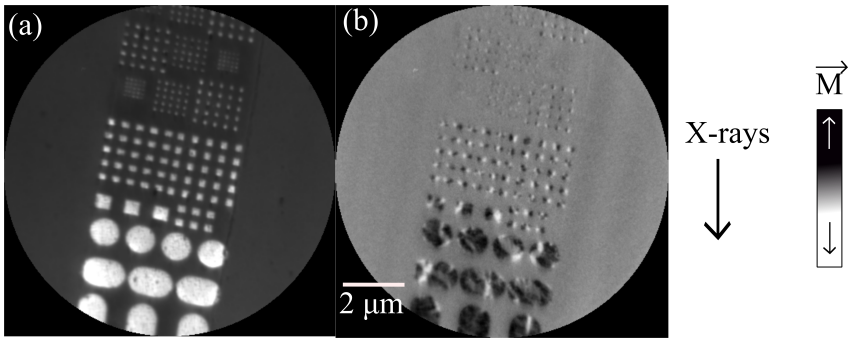

Figure 4.6: XPEEM image of $Co/BaTiO_3$ heterostructures: (a) Elemental contrast of Co structures and (b) Respective XMCD image.

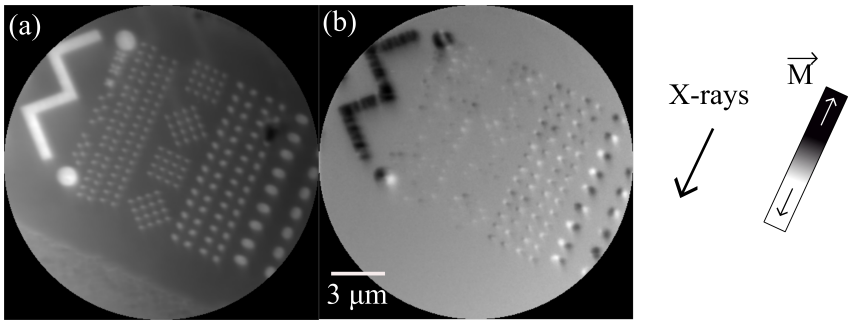

Figure 4.7: XPEEM image of $Ni/BaTiO_3$ heterostructures: (a) Elemental contrast image Ni structures and (b) Respective XMCD image.

Next, XMCD images were acquired at different applied voltages (± 5 V, ± 10 V, ± 20 V) to determine the changes in the magnetization with the electric field. The voltage was ramped up slowly at a rate of 100 mV/s. We initially observed no changes in the magnetization with the applied voltage. Then, the ramping rate was increased to more than 500 mV/sec and at this time we observe changes in the capacitive devices irrespective of the gap width (5, 10 or 15 μm) at +20 V. Figure 4.8 and Fig. 4.9 show the changes in the magnetic spin structure with applied voltages for Ni and Co magnetic structures,

respectively. We observe a change in Co and Ni magnetic configuration with sizes and shapes ranging from > 3 μm to 500 nm with applied voltage. A 20 V applied across 10 μm thick $BaTiO_3$ corresponds to an electric field of 2 MV/m. We find that at certain regions the local magnetization can change by 180° as seen in the intensity profile plotted as a function of applied voltage in both Fig. 4.8 and Fig. 4.9, suggesting a high level of strain created by the $BaTiO_3$. We find that the changes occuring in the magnetization within a single magnetic structure is not uniform and vary between the structures. This is different from the changes observed by Lahtinen et al. [57], López González et al. [127] or Buzzi et al. [59], where magnetic structures in a mono domain were present on a single ferroelectric domain. Hence, it is possible that the ferroelectric domains in our sample are spread randomly across the $BaTiO_3$ layer as observed from piezoresponse force microscopy on $BaTiO_3$(110) by Takao Shimizu et al. [128]. Therefore, it is possible that the strain created by the $BaTiO_3$ is not uniform, which in turn could result in random changes in a single magnetic structure. Due to the lack of a conducting substrate the sample cannot be used for piezoresponse force microscopy to characterize the ferroelectric domain distribution. By reversing the applied voltage (-20 V), the magnetization did not return to its initial state; we observe small changes in a few regions but the changes were not significant as what was observed with +20 V. For example, small changes in the magnetization when the voltage is reversed can be observed in the intensity profile of Ni/$BaTiO_3$ shown in Fig. 4.8. This indicates that the changes in the magnetization with the applied electric field is probably due to (1) an electrostrictive effect created by the $BaTiO_3$ and not the ferroelectric or piezoelectric switching or (2) the magnetic structures are pinned such that they cannot be modulated. To verify the surface roughness we characterized the same sample with atomic force microscopy.

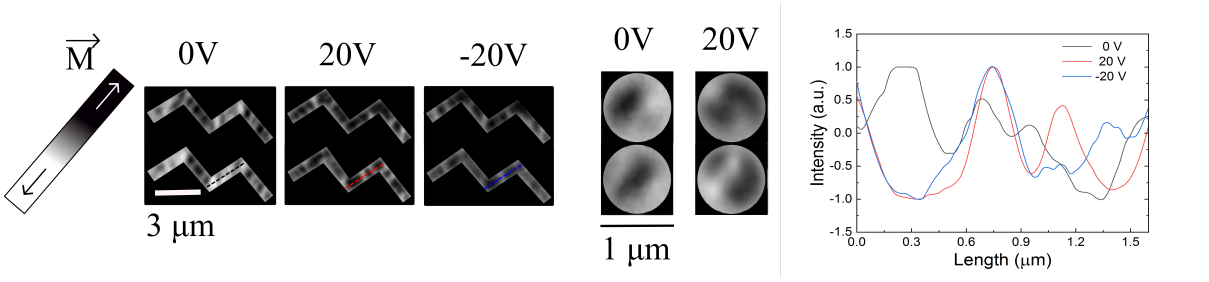

Figure 4.8: XMCD images of elements of Ni as a function of applied voltage. The plot represents the intensity profile of the black, red and blue dotted lines indicated shown on the picture at different applied voltages.

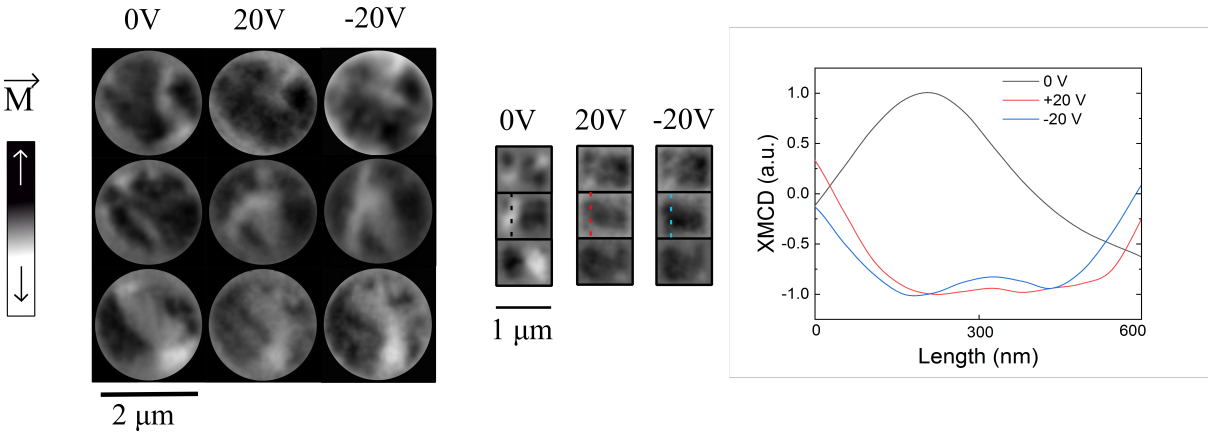

Figure 4.9: XMCD images of elements of Co dots as a function of applied voltage. The plot represents the intensity profile of the back, red and blue dotted lines shown on the picture at different applied voltages.

From the surface roughness characterization (Fig. 4.10), we find that the surface of the $BaTiO_3$ is indeed rough, with a roughness rms value of over 10 nm, which is half the thickness of the Co/Ni films; therefore it is possible that the magnetic structures are pinned to the $BaTiO_3$ layer which prevents the magnetization to change. Due to the lack of a reversible process, the samples are not suitable for high frequency pump and probe characterization.

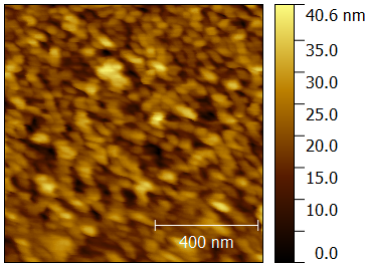

Figure 4.10: Surface topology of $BaTiO_3$ of the sample whose XPEEM data is shown in Fig. 4.6.

Discussion

Following these initial results, we carried out a detailed study on the sample preparation in order to improve the quality of the surface roughness of $BaTiO_3$ films. As a first step, we checked the quality of the $SrTiO_3(110)$ substrate. From atomic force microscopy, we find a smooth surface with some clusters of particles on the surface as shown in Fig. 4.11. These particles are over 1 nm in height, therefore it is possible that such particles interfere with the growth process. $SrTiO_3$ substrates can be treated with HF to obtain a smooth surface and this process etches SrO ions leaving a TiO_2 terminated substrate helpful for growing films with better crystallinity. The HF etching procedure was predominantly followed to grow $BaTiO_3$ on a $SrTiO_3(001)$ orientation and has not been employed for growing $BaTiO_3$ on $SrTiO_3(110)$ orientation. However, since our $BaTiO_3$ growth results in a high level of surface roughness, it is possible that the poor surface quality of the substate is affecting the growth process, hence we carried out HF treatment on (110) orientated substrate as well. For the $SrTiO_3$ treatment, we followed the protocol from Biswas et al. [129]. The process starts from cleaning the substrate using acetone and isoproyl alcohol in ultrasound for 10 minutes each followed by cleaning with demineralized water with ultrasound for 5 minutes. The substrate is then soaked with buffered hydrogen fluoride solution ($HF:NH_4F + HNO_3 = 1:7$ vol.) for 30 s, followed by annealing at 1000 °C under oxygen atmosphere for 2-3 hours. The surface of $SrTiO_3$ (110) substrate before and after chemical treatment measured by atomic force microscopy is shown in Fig. 4.11, where a clear difference on the surface topology and roughness can be noticed; the treated substrate has a better surface with no large particles.

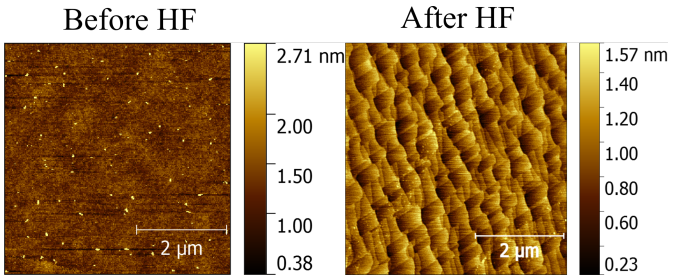

Figure 4.11: Surface topology of $SrTiO_3$ before and after etching with buffered HF.

In the next step we deposited the $BaTiO_3$ layer by pulsed laser deposition on the chemically etched $SrTiO_3$ substrate using similar parameters as before. Figure 4.12(a) shows the atomic force microscopy of the $BaTiO_3$ surface grown on a HF treated $SrTiO_3$, where it is clear that the surface of $BaTiO_3$ is different and much smoother than those obtained without HF etching, with smaller grain size and a surface roughness rms of about 5 nm, although we still find some regions with larger particles as observed in the previous sample (Fig. 4.10). With the new substrate treatment another sample was fabricated using a similar procedure as mentioned above and from XPEEM analysis we still find a lack of systematic control with the magnetization. Therefore, it is possible that the problem is arising from the $BaTiO_3$ deposition process or from the quality of $BaTiO_3$ film itself and not from the substrate. In the next step we tried to optimize the $BaTiO_3$ deposition process by varying the laser repetition rate, laser fluence, beam spot, substrate temperature and chamber pressure. We find that a slower repetition rate and smaller laser spot (diameter = 4-5 mm) on the target result in a much smoother $BaTiO_3$ surfaces [Fig. 4.12(b)]. One may anticipate that such films may result in a better magnetoelectric coupling.

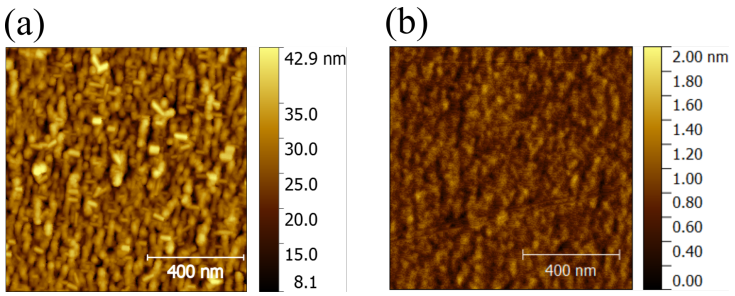

Figure 4.12: (a) Surface topology of $BaTiO_3$ on HF treated $SrTiO_3$ substrate. (b) Surface of $BaTiO_3$ grown on HF treated $SrTiO_3$ with low laser fluence and smaller beam spot.

4.2 Outlook and Future plans

For the last $BaTiO_3$ films, the growth parameters were optimized without the Pt electrodes, and to use such films, the electrodes would have to be made on the surface, making the sample not suitable for XPEEM. Therefore, we propose other characterization methods and also other possible strain mediated coupling systems which can potentially be less challenging. We propose the use of diffractive MOKE and/or Hall probe measurements. The samples which were described in the previous sections consist of lateral capacitive devices with a maximum gap of 15 μm, and containing in-between the magnetic structures of various sizes with IP magnetization; therefore performing longitudinal MOKE to probe the IP magnetization will be challenging as it is difficult to separate the reflected light from the magnetic structures for analysis. To overcome this issue, one can consider a large array of similar magnetic structures which can result in a diffractive pattern from the laser light reflection. However, we will again be limited by the small dimension of the capacitor. Hence, a simple two electrode capacitive structure can be replaced by an interdigitated capacitor structure, with arrays of magnetic structures in-between every pairs of electrodes, which can result in a much simpler and distinct diffractive pattern from reflected light. Similarly, one can also consider creating a wire-like magnetic structure from which the change in magnetoresistance can be measured, for example from a saturated state to a multidomain state. Fig. 4.13 shows a schematic of such sample design where one can measure both MOKE signal and magnetoresistance. Interdigitated electrodes were also used by Foester et al. [30] to study dynamics of strain mediated coupling by generating surface acoustic waves on a $LiNbO_3$ substrate.

Besides investigating ferroelectric-ferromagnetic heterostructures, we suggest piezoelectric-ferromagnetic heterostructures with AlN [60] or ZnO [61] as piezoelectric material, which can also form a suitable device for high frequency characterization. The deposition of AlN and ZnO is less complex and can offer more flexibility with the fabrication process. Even though the piezoelectric strain created is smaller than $BaTiO_3$, one can fabricate samples with different connectivities and thereby increase the strain from different axis. Another possible way to use such piezoelectric materials is in the form of micro-electro-mechanical systems (MEMS). We propose a simple design which requires a low stress silicon nitride

membrane as the substrate; these type of structures are already in use in microspeakers and can oscillate at frequencies of a few hundreds of kHz [130] [131] [132] [133], which can be enhanced further to reach higher frequencies. A schematic of a microspeaker-like device with a magnetic structure is shown in Fig. 4.14, where the membrane can be bent with an applied electric field. The bending is due to the electrostatic force between the two electrodes lying on the top and bottom part of the piezoelectric layer. The displacement of the membrane with the applied electric field can be as high as 10 μm, which can result in a large strain on the ferromagnetic material. The use of silicon nitride membrane provides the additional advantage of enabling one to characterize the magnetic material using transmission methods.

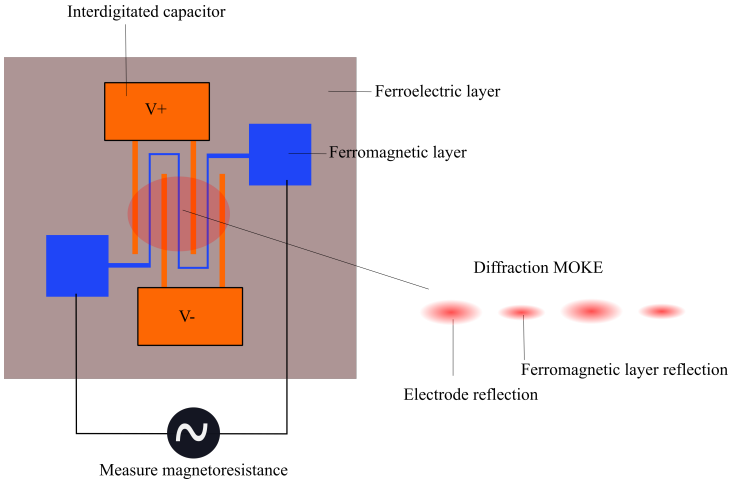

Figure 4.13: Schematic of interdigitated capacitor with a ferromagnetic layer in between the electrodes showing the diffractive MOKE signal and the measuring schematic of the magnetoresistance.

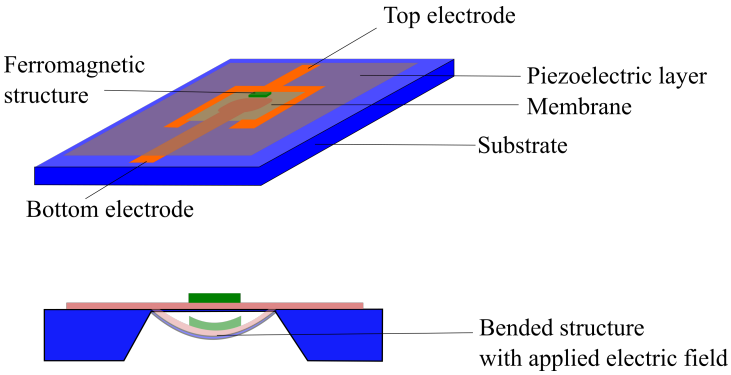

Figure 4.14: Strain mediated coupling using a microspeaker device.

In summary, we have fabricated artificial multiferroic heterostructures with Co and Ni magnetic structures on $BaTiO_3$ with magnetoelectric coupling. Due to the high level of surface roughness a systematic control of the magnetization was not possible. However, by changing the pulsed laser deposition parameters, we were able to optimize the growth process which could enable reproducible control of the magnetization. Furthermore, we have also proposed other systems such as piezoelectric/ferromagnetic or MEMS devices to investigate strain-mediated coupling which can be less challenging than the $BaTiO_3$-ferromagnetic structures. In the next chapter we discuss the charge-mediated magnetoelectric coupling mechanism and the possibility to perform high frequency characterization.

Chapter 5

Charge-mediated magnetoelectric coupling in Si_3N_4 gated ferromagnetic structures

This chapter describes the results of charge-mediated magnetoelectric coupling using Si_3N_4 gated Pt/Co/Pt heterostructures using X-ray photoemission electron microscopy (XPEEM). We observe a change in magnetic anisotropy in the form of domain wall nucleation and a change in the rate of domain wall fluctuation as a function of the applied electric field to the sample. We also observe the coexistence of in-plane and out of plane magnetization in Pt/Co/Pt heterostructures in a region around the spin reorientation transition whose formation is attributed to substrate surface roughness which is comparable to the film thickness; with such domain configuration, we find that the in-plane magnetization is more sensitive to the applied electric field than out of plane magnetization. Although we find an effective magnetoelectric coupling in our system, the presence of charge defects in the silicon nitride membranes hampers a systematic electrostatic control of the magnetization. The text, figures and results described in this chapter are adapted from [134].[1]

[1]The magneto-optic Kerr effect (MOKE) characterization, image analysis, sample preparation and fabrication was carried out by me, the film deposition by Mr. Michael Horisberger and myself. The XPEEM characterization was performed by Dr. Carlos A. F. Vaz, Mr. David Bracher, Mrs. Tatiana Savchenko and myself. The X-ray transmission measurement was performed by me with the help of Dr.

5.1 Coupling in Si_3N_4 and Pt/Co/Pt heterostructures

In chapter 2, we have introduced the charge mediated coupling phenomenon in ferroelectric/ferromagnetic interfaces. However, the use of a ferroelectric comes with many challenges, including the need for the growth of high quality ferroelectric films with good electrical properties and smooth surfaces, since sharp and smooth interfaces are important for large magnetoelectric couplings [135] [136]. We have also shown in the previous chapter the difficulties involved in optimizing the growth process of $BaTiO_3$ to obtain a smooth surface. To overcome these issues, the ferroelectric can be replaced by a dielectric whose growth process is simple and has been optimized. Although the permittivity of dielectrics is typically smaller than that of ferroelectrics, sizeable magnetoelectric couplings can still be found at the interface of ferromagnetic and various dielectric layers (MgO [137] [138], Al_2O_3 [72] [64], GdO_x [73] [74], ZnO [139] [61]) and also in dielectric stacks [140] [64].

In this section, we present the existence of a magnetoelectric coupling in silicon nitride membrane-gated Pt/Co/Pt heterostructures. The advantage of using silicon nitride is that it can be produced as a thin membrane, with good surface and insulating properties. Furthermore, with better insulating properties, higher electric fields can be applied that allow one to obtain charge modulations at the interface similar to that of high dielectric or ferroelectric materials. Silicon nitride was also considered in electrically read only memory or in flash memory devices and was proposed in 1967 [141]. Silicon nitride was used as a charge trapping device to store information [142], therefore providing additional motivation to investigate the possibility to combine magnetoelectric coupling in silicon nitride gated devices and its charge trapping effects for future MRAM or memory devices. We find that the cut off frequency associated with a 200 nm silicon nitride membrane was around 1 MHz, therefore making it suitable for high frequency characterization. With silicon nitride membranes one can perform transmission based X-ray measurements.
Pt/Co/Pt heterostructures are known to have a strong perpendicular magnetic anisotropy (PMA) due to surface and interface induced anisotropy energy contributions [143] [144] [145], whose strength can be modified by using electric fields [72]. To achieve a higher

Jan Dreiser, Dr. Micheal Studniarek and Dr. Niéli Daffé.

sensitivity of the magnetic state to an applied electric field and therefore higher susceptibilities, we consider here Pt/Co/Pt heterostructures with the Co thickness set to the spin reorientation transition (SRT), at around 6 Å, where a change in the magnetization direction occurs from out-of-plane (OOP) to in-plane (IP) [146] [147] [148] [149]. In addition, thermal excitations may lead to domain wall (DW) fluctuations [150] [151]. Real time DW fluctuations have been observed using XPEEM [152] [153], with an amplitude that was found to vary with film thickness [152] and temperature [151] [154]. For example, the rate/amplitude of DW fluctuation is higher near the SRT and becomes smaller away from the SRT. In this work, by acquiring sequences of XPEEM images with time, we show that we are able to control the anisotropy of the system electrostatically in Si_3N_4/Pt/Co/Pt heterostructures, which is manifested in a control of the DW fluctuations, of the domain configuration, and of the SRT. By increasing the Co thickness by about 0.5 Å around the SRT, we observe the simultaneous presence of IP and OOP domains with a controllable change in the domain pattern with the applied electric field. Finally, we show that the presence of charge defects in the silicon nitride membrane and its negative impact on the electric field control of the magnetic anisotropy.

5.1.1 Sample growth and characterization techniques

Silicon nitride membranes were used as a substrate and also as a gate dielectric to investigate the electric field control of magnetism in the Pt/Co/Pt system. High resistivity and low stress silicon nitride membranes with thickness of 200 nm and window size of 500 × 500 μm^2 and 1 μm thick membranes with window size of 1 × 1 mm^2 were used. Silicon nitride has a dielectric constant of about 7.5 and a band gap of 5 eV [155] and is commonly used as an insulator in electronic devices. From atomic force microscopy, we find that the membranes have a measured roughness value of 1.2 nm (rms) for 200 nm membranes to around 3.5 nm (rms) for 1 μm thick membranes. Before metal deposition, the membranes were cleaned in a piranha solution (H_2O_2 + H_2SO_4). The top electrode Cr (3 nm)/Cu (80 nm)/Cr (3 nm) and the bottom electrode Cr (3 nm)/Cu (50 nm)/Cr (3 nm) were deposited using thermal evaporation with a shadow mask. A layer of Cr is deposited before and after Cu deposition to increase the adhesion to the membrane and

prevent oxidation of Cu, respectively. At this thickness, the Cu layer does not strain the membrane, which was confirmed by checking with an optical microscope, since a strained membrane can be identified from folding at the edges. The Pt (10 Å)/Co (6 or 6.5 Å)/Pt (15 Å) layers are grown after the electrode deposition using magnetron sputtering with a base pressure of about 10^{-7} mbar. We find that the SRT for this heterostructure grown using our sputtering system occurs between 6 Å – 7 Å Co thickness. The bottom Pt layer is kept at a small value of 10 Å in order to maximise the magnetoelectric coupling effect and to protect the Co from contamination from any adsorbates on the silicon nitride membrane (deposition of Co directly on silicon nitride membrane resulted in oxidation of Co). Finally, reference marker structures for XPEEM made of Cr were patterned using e-beam lithography. The final fabricated samples appear similar to the schematic shown in Fig. 5.1(a).

The applied voltages are current-limited to 100 μA to avoid local sample heating. For applied voltages of 10 V on a 200 nm thick membrane, a power of around 0.4 nW/μm^2 and for a 1 μm thick membrane, a power of around 0.1 pW/μm^2 were estimated. The top electrode/surface of the sample is locally connected to the high voltage and the electric field is applied from the bottom electrode; therefore, with applied positive electric fields, the Pt/Si_3N_4 interface accumulates electrons. The experiments were carried out at room temperature and under ultrahigh vacuum ($<10^{-10}$ mbar). The samples were characterized with MOKE [Durham Magneto Optics NanoMOKE3(R)] at room temperature.

5.1.2 Electric field control of domain wall fluctuations at the SRT with PMA

Magnetic hysteresis curves of a Si_3N_4 (200 nm)/Pt (10 Å)/Co (6 Å)/Pt (15 Å) heterostructure obtained using MOKE are shown in Fig. 5.1(b). We observe the presence of a dominant PMA [143] [144] [145] [156] in the sample, as shown by the presence of a square loop in the OOP geometry and a hard axis loop in the IP geometry. The presence of a large coercivity and non-zero remanence in the IP hysteresis suggests that there exists an IP component in the magnetization. Before XPEEM characterization, the sample was saturated in a magnetic field of 4 kOe out of the plane. X-ray magnetic circular dichroism

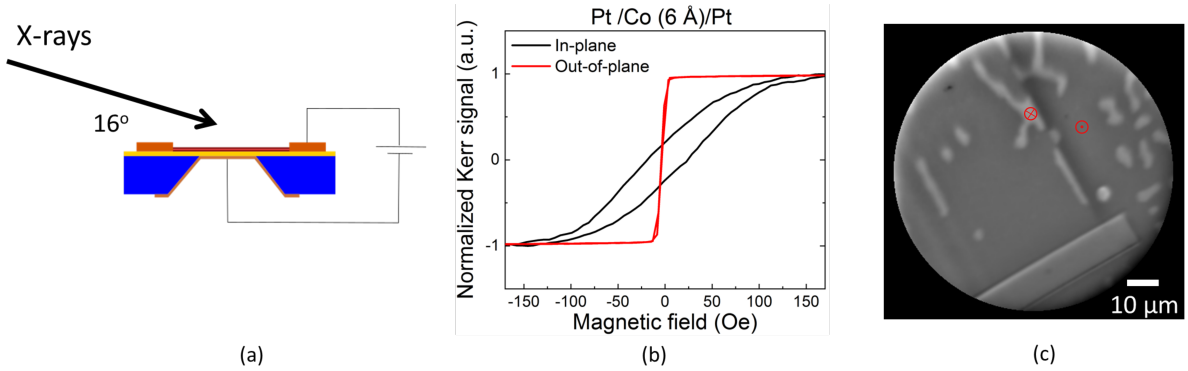

Figure 5.1: (a) Cross section of fabricated sample and measuring geometry, the blue region corresponds to Si, yellow to the Si_3N_4 membrane, electrodes are shown in brown and the tri-layer Pt/Co/Pt is present between the two top electrodes. (b) Longitudinal and polar MOKE signal as a function of applied magnetic field for Pt/Co(6 Å)/Pt. (c) XMCD image of Pt/Co/Pt heterostructures measured at Co L_3 edge (white contrast - spin down, dark contrast - spin up). Figure adapted from ref. [134].

(XMCD) images were acquired at Co L_3 edge. The initial domain pattern obtained from XPEEM is shown in Fig. 5.1(c).

From sequences of XMCD images we find that reverse domains were slowly nucleating, while fluctuations in the DW position in most parts of the imaged area could also be observed. XMCD image sequences were acquired as a function of applied voltage at ±6 V, ±10 V and ±15 V. At ±6 V, we find a decrease in the rate of fluctuation of the domain wall position. At +10 V we observe an increase in the DW fluctuation rate with larger fluctuation amplitudes (about 1 μm) and a much faster nucleation of magnetic domains (with an estimated DW velocity of about 0.15 μm/s). At -10 V we observe less fluctuations and no reverse domain nucleation, i.e., the DW was stable as long as the voltage was continuously applied. The control of the DW fluctuation rate confirms the presence of a magnetoelectric coupling between the silicon nitride dielectric and the Pt/Co/Pt. To understand further the control of the DW fluctuation as a function of electric field, XPEEM image sequences were processed to quantify the rate of change in the DW fluctuation rate and amplitude. The images are first corrected for drift, then from individual images the DW position was extracted by using the Canny edge detection method available in Matlab [157] [158]. After extracting the DW position from individual

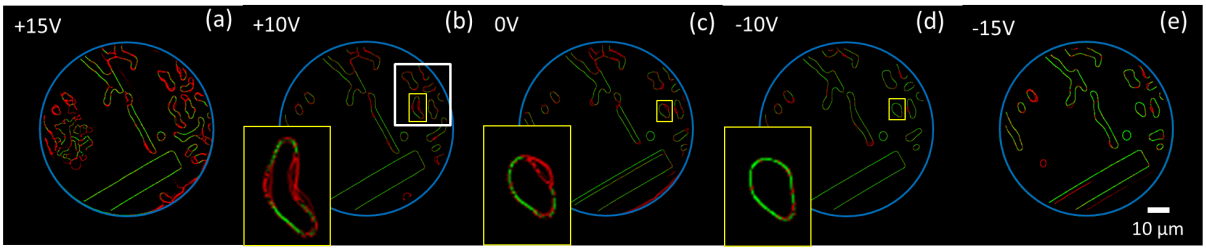

Figure 5.2: (a-b) Extracted domain wall summed over all images as a function of applied voltages. The red regions represent regions which moved once or more than once and the green regions are stable domain walls. The inset in the zoom-in image of the magnetic domain marked in yellow box. The domains enclosed in white box is used for the analysis and the zoom-in version is shown in Fig. 5.3. Figure adapted from ref. [134].

.

images, the images were summed to a single image, such that the regions where the DW overlap show a higher intensity than the regions where it fluctuates.

Figure. 5.2 (a-e) shows the processed image sequences taken at different applied voltages; the region marked in red represents regions where the DW moved once or more in a twenty image sequence, while green regions represent stable DWs; one can notice that at 10 V [Fig. 5.2(b)] and 0 V [Fig. 5.2(c)] there are more red regions than at -10 V [Fig. 5.2(d)]. The inset in the images shows the state of a single domain (within the purple box) for different applied voltages, showing in more detail that at -10 V the domain is very stable with no fluctuations while at +10 V a change in the shape of the domain occurs together with an increase in the DW fluctuation rate. To calculate the displacement of the DW in the image sequence, we calculate the relative change of the perimeter of the same domain wall with respect to the first image in the sequence; a positive value indicates nucleation and increase in size of the domain while a negative value corresponds to domain shrinking. The perimeter is calculated to first approximation by summing the number of pixels in the image, since the images with extracted DW have intensity '1' in the DW position, while the remaining part of the image has value '0'. The domain wall perimeter provides information about how much the domain shape has changed from the initial state and by how much per each image in the sequence. The domains enclosed in the white box shown in Fig. 5.2(b) are considered for this analysis and the zoomed in

image is shown in Fig. 5.3(a). The displacement of the DW, i.e. the change in perimeter of the DW with time, is shown in Fig. 5.3(b) for 0 V, +15 V and -15 V; the horizontal black lines correspond to the DW perimeter of the first image at the respective voltage. We find that the perimeter of the DW at 0 V and 15 V fluctuates with a larger amplitude and does not return to its initial state, indicating that the DW perimeter or the size of the domain is increasing with time. For -15 V, we observe small fluctuations, predominantly in the vicinity of the initial state, while the decrease in the perimeter of the DW from the initial state indicates that the domains are shrinking with time.

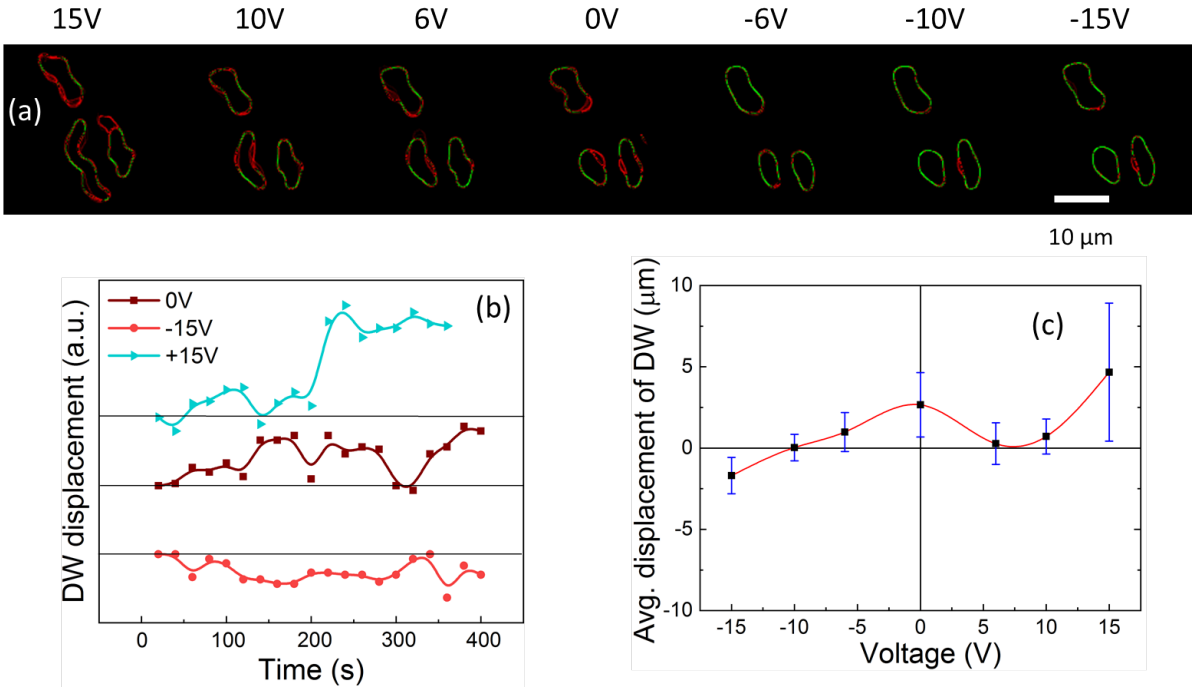

Figure 5.3: (a) Sequence of domain wall fluctuations as a function of applied voltage, red and green indicates that the region moved more than once and stable respectively. (b) Domain wall displacement with time as a function of applied voltage of the domain wall shown in (a). (c) Averaged domain wall displacement as a function of applied electric field of the domain wall shown in (a). Figure adapted from ref. [134].

Figure. 5.3(c) shows the average change in DW perimeter acquired as a function of the applied voltage, where it is clear that the positive electric field favors nucleation and negative electric field favors reverse nucleation. The video of the DW fluctuations as a function of electric field can be found in ref. [134]. Here, we also highlight the

possibility that the bottom Pt layer can be polarized due to the presence of Co, therefore the polarization is modulated at Pt layer by electric field which in turn can affect the anisotropy in Co [159] [160] [161] [162] [163]. However, since the thickness of all the layer combined is about 3.5 nm, one should consider the entire heterostructure as a single magnetic system.

A single XMCD image in the image sequence is acquired in 20 s and from the DW fluctuation rate, one can estimate the energy barrier (E_b) associated with the DW fluctuations using an Arrhenius equation $f = f_0.\exp[-E_b/k_BT]$, where f_0 is an attempt frequency (about 1.9×10^9 Hz) [164] [165], which is defined as the number of fluctuations a spin undergoes before it flips, k_B and T are the Boltzmann constant and temperature, respectively, and the experimental frequency f is obtained from the same DW at zero, positive and negative electric field. Using these values we obtain E_b about 0.61 eV for zero and positive electric field, and E_b about 0.68 eV for negative electric field, which corresponds to a change of about 10 % in the energy barrier height with the application of 10 V (50 MV/m). The equivalent change in the Fermi energy can be calculated from the charge modulation at the interface, $Q = V.\epsilon_r\epsilon_0 A/d$, where ϵ_r is the relative permittivity, ϵ_0 is the permittivity in vacuum, A (500×500 μm^2) is area and d (200 nm) is the silicon nitride thickness, from which we estimate the number of electrons modulated at the interface per unit area as about $\pm 2.07 \times 10^{12}$ e/cm^2 and for number of electrons modulated per atom of Co as $\pm 0.9 \times 10^{-3}$ e/atom. The latter could result in a change of Fermi level ($E_f = \Delta N/\mathrm{DOS}\times d_{Co}$) by 0.2 – 0.7 meV, where DOS is density of states of Co at the Fermi level, about 17.26 electrons/(atoms Ry spin) [166], and d_{Co} is the number of monolayers (1-3) corresponding to a Co thickness of 2 – 6 Å. A similar value was obtained by Maruyama et al. [64], which was enough to modify the anisotropy of a few monolayers (1-3) Fe layer using MgO as gate dielectric. Therefore, in Pt/Co(6 Å)/Pt with PMA, with positive electric field and zero electric field, the anisotropy energy is reduced, favoring the breaking down of the saturated domain into a multidomain state, while a negative electric field increases the anisotropy energy and favors a mono domain state, a result similar to that reported by Mantel et al. [140]. In order to rule out chemical modification of the Co state with the electric field, we measured the X-ray absorption spectra (XAS) of Co under the applied voltages, which are shown in Fig. 5.4(a). The

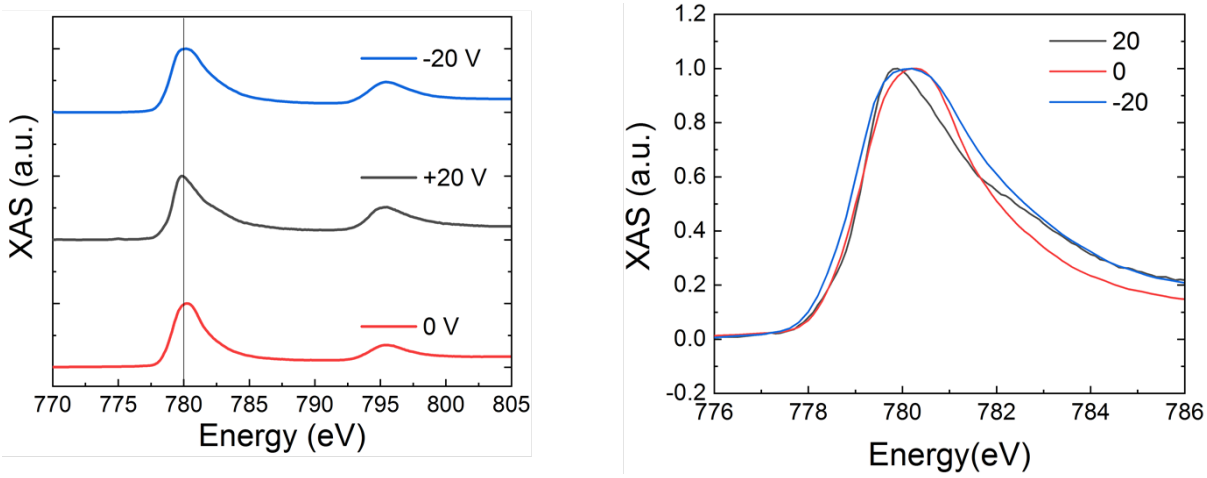

Figure 5.4: (a) XAS obtained from XPEEM acquired from the regions shown in Fig. 5.2 as a function of applied voltage. (b) Zoom-in spectra of Co L_3 edge shown in (a) as a function of applied voltage. Figure adapted from ref. [134].

XAS indicates no significant changes in the L_3 peak, such as formation of an oxide peak. However, from Fig. 5.4(b), we find that the peak becomes narrower with a small shoulder like feature away from the position of oxide peak (usually at 780 - 781 eV) for +20 V. Similarly, for -20 V we observe broadening of the L_3 edge. We attribute these changes to the change in Fermi energy or modifications in the multiplet structures. The trend consistent with what was observed in the average displacement of the DW with electric field 5.3(b).

5.1.3 Electric field control of the magnetic state at the SRT with coexisting IP and OOP domains

An increase in the Co thickness from 6 Å to 6.5 Å resulted in the presence of both IP and OOP magnetization components, as seen in the MOKE data shown in the Fig. 5.5(a), where we find a square hysteresis loop for both IP and OOP directions of the applied magnetic field, with the coercivity for OOP direction (about 20 Oe) being higher than that of the IP easy axis direction (about 10 Oe). We also see the presence of a uniaxial in-plane anisotropy from polar plots of the IP coercivity, as shown in Fig. 5.5(b), hence we cannot exclude the possibility that the easy axis is canted to certain OOP angle. Samples with 6.5 Å Co thickness were grown simultaneously on both 1 μm and on 200 nm thick

silicon nitride membranes. From XPEEM we find similar domain patterns for the films grown on both membrane thicknesses, even though the surface roughness is different by about 50%; here we show results for Si_3N_4(1 μm)/Pt (10 Å)/Co (6.5 Å)/Pt (15 Å). We performed electric field dependent MOKE measurements in both IP and OOP geometry to verify the changes in the magnetic anisotropy. First, we discuss the IP MOKE data as a function of electric field, shown in Fig. 5.5(c) as black squares; with the application of +5 V we observe that the coercivity of the IP hysteresis loop changes by about 2 Oe, then by removing the electric field the coercivity further reduces by 1 Oe, and with every subsequent voltage excitation we observe a change in the coercivity. We applied several cycles of voltages with different magnitude and find that the coercivity value tends to reduce, with some fluctuations. The drop in the coercivity indicates that the IP easy axis is changing towards a hard axis. During MOKE characterization we simultaneously imaged the surface of the membrane using the Nano-MOKE microscope and found no detectable straining of the membrane with the applied electric field. We also find that the coercivity does not change when there is no electric field applied, as shown in Fig. 5.5(c) as red squares; hence, we attribute the change in coercivity with electric field to charge modulation at the interface. After 50 voltage cycles the coercivity changed from 10 Oe to 1 Oe (a change of about 90%), reaching a hard axis behaviour, and further application of voltage excitations leads to no further changes in the magnetic response; the initial and the final hysteresis loop of IP geometry after applying 50 cycles of voltages is shown in Fig. 5.5(e). Similarly, we find that the change in OOP hysteresis loop as a function of applied voltage cycles was very small, with a change in coercivity of less than 2%, as shown in Fig. 5.5(d). Therefore, based on the MOKE characterization, a sample with both IP and OOP magnetization components can be manipulated by the electric field; however, we find that IP magnetization is more sensitive than the OOP magnetization, which we relate to the sensitivity of the magnetic state to the perpendicular magnetic anisotropy at this Co thickness. Considering the roughness of the membrane substrate, it is possible that the 1 nm thick Pt layer is not continuous, such that some regions of the Co layer may be in contact with the membrane; these Co regions may have weaker perpendicular magnetic anisotropy (more in-plane magnetization component) and see a stronger effect from the electric field in the dielectric substrate.

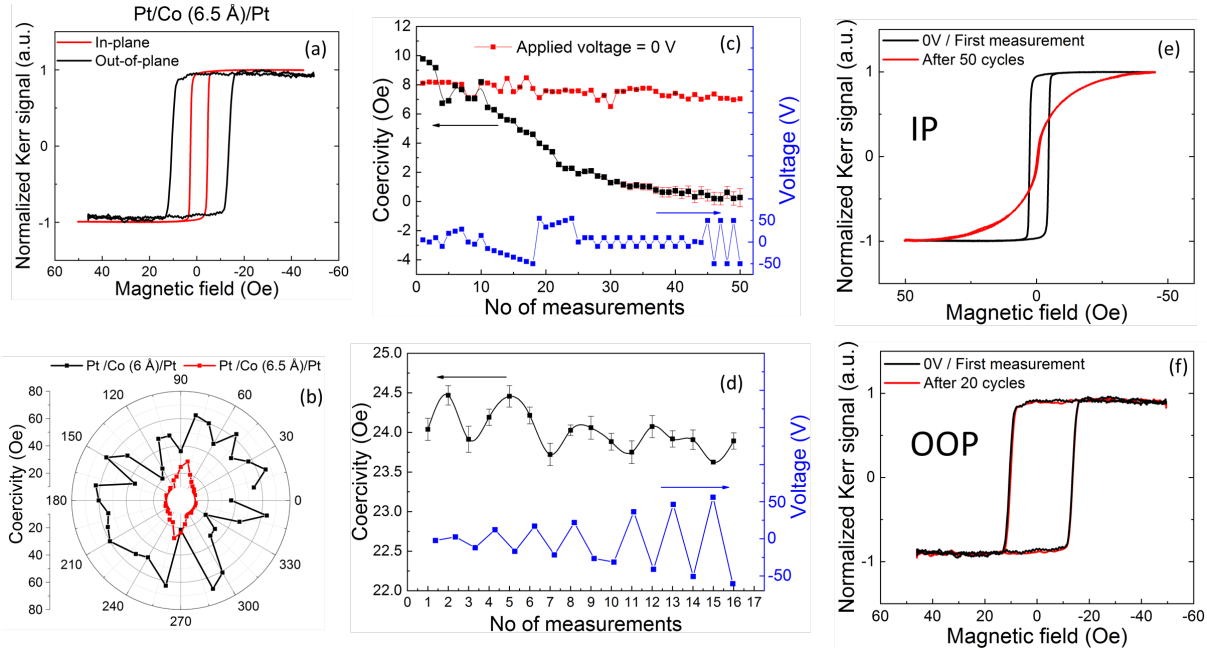

Figure 5.5: (a) MOKE characterization of IP and OOP geometry of Pt/Co (6.5 Å)/Pt. (b) Polar plot of the IP coercivity of Pt/Co (6 Å)/Pt and Pt/Co (6.5 Å)/Pt. (c,d) Change in IP and OOP coercivity as a function of electric field pulse sequence, respectively (lines are guides to the eye). (e) IP Hysteresis loops before and after the application of 50 voltage cycles shown in Fig. 5.5(c). (f) OOP Hysteresis loops before and after the application of 16 voltage cycles shown in Fig. 5.5(d). Figure adapted from ref. [134].

To understand the magnetic domain structure, the sample was first demagnetized using an in-plane AC magnetic field of about 15 mT and was imaged with XPEEM. We observe irregular shaped domain patterns as shown in Fig. 5.6(a), with a lateral dimension of the order of 1 μm. To verify the possible presence of IP and OOP magnetization, the sample was rotated azimuthally with respect to the X-ray beam direction as shown in Fig. 5.6(b). The XMCD effect is a magnetization vector dependent absorption process and the intensity of absorption is given by $I = \alpha.M.cos(\theta)$, where α is the X-ray propagation vector, M is the direction of magnetization and θ is the angle between α and M; the incidence angle of X-ray in XPEEM is 16°, which leads to a higher sensitivity to the IP magnetization. When the sample is rotated [Fig. 5.6(b)], the intensity of absorption of IP domains changes but not that of the OOP domains. The sample was imaged at 0° and 90° and the magnetic contrast images show regions where the magnetic contrast changes,

corresponding to IP domains, and regions where the magnetic contrast remains constant, corresponding to OOP domains. The latter are coloured in magenta in Fig. 5.6(a) and for this particular state, it represents about 1% of the overall area imaged. This observation confirms the coexistence of IP and OOP domains, which we attribute to the relatively large surface roughness of silicon nitride membrane, comparable to the thickness of the Co layer, and also possibly to a slight non-uniformity in the thickness of Co, which is around the SRT. The origin of such spin structure is described in the next chapter.

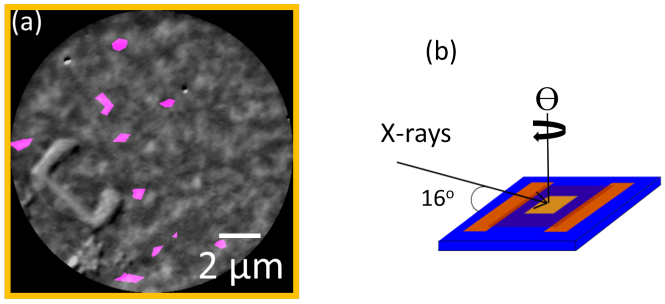

Figure 5.6: (a) XPEEM image of Pt/Co(6.5 Å)/Pt with IP and OOP domains where OOP domains are marked as magenta. (b) The measuring geometry and the angle of rotation with respect to the incoming X-rays. Figure adapted from ref. [134].

To learn more about the effect of the electric field in such a domain configuration, XMCD images as a function of the applied voltage were acquired and are shown in Fig. 5.7(a-l). We observe that the multidomain state gradually breaks down into smaller domains with increasing applied voltage and eventually the domain size becomes smaller than the microscope resolution. We observe the breaking down of domains to very small domains in both directions of the applied voltages which is in agreement with the MOKE data, which shows that the coercivity reduces with applied electric field in both positive and negative direction. In the image sequence shown in Fig. 5.7(a-l), one can observe, for positive voltages, that the transition from larger domain configuration to a very small domain configuration occurs at 9 V while for negative voltages it occurs at -6.5 V. Upon removal of the electric field we observe that the initial larger domain configuration reappears [Fig. 5.7(l)], and we find that there are some small, but observable changes in the IP domains while the OOP domains marked in magenta in Fig. 5.6(a) remain unchanged. This result agrees with the MOKE data, where we saw changes only in the

IP anisotropy. With 1 μm silicon nitride membrane and an applied voltage of about 10 V (10 MV/m), for the charge carrier modulation and change in Fermi energy, we expect a value to be lower by a factor of 10 compared to the 200 nm thick membranes. It is unclear why we observe similar changes for both directions of the applied electric field. Interface roughness could play a role, since the roughness of the substrate is comparable to the film thickness, and in fact surface induced changes in spin concentration has been demonstrated in Fe monolayers [167] and roughness induced band gap modification has also been discussed in oxides [168].

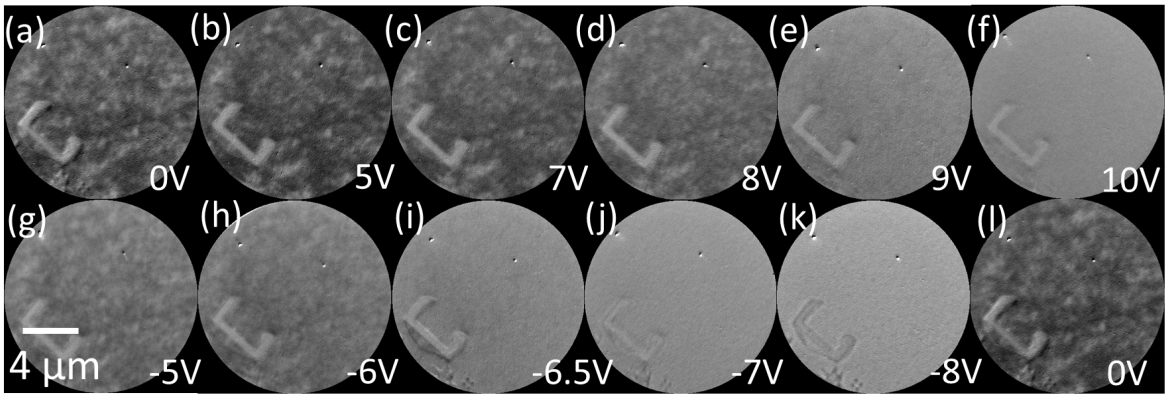

Figure 5.7: Domain pattern as a function of applied voltage for Pt/Co(6.5 Å)/Pt. Figure adapted from ref. [134].

5.1.4 X-ray transmission characterization

We also performed transmission XAS to supplement the XPEEM data carried out at X-Treme beamline. Spectroscopy characterization was performed on the sample grown on 200 nm thick silicon nitride membrane [Si_3N_4 (200 nm)/Pt (10 Å)/Co (6.5 Å)/Pt (15 Å)]. The measuring geometry is shown in Fig. 5.8(a). The X-rays are set normal to the sample surface and the absorption is measured by a photodiode placed behind the sample. The electric terminals from the sample and photodiode are isolated and do not interfere with the measured signal. The absorption was recorded in the photon energy range from 750 eV to 820 eV covering both L_3 and L_2 edges of Co. The sample was measured at normal incidence probing the OOP magnetization. To verify a change in the magnetization, XMCD spectra were measured at a 50 mT magnetic field applied

in the direction of the X-rays, which is sufficient to saturate the magnetization OOP. XAS spectra were measured with C_+ and C_- polarization and the XMCD spectra is calculated as $(C_+ - C_-)/(C_+ + C_-)$. By applying the electric field, we see a clear change in the XCMD spectra [Fig. 5.8(c)], indicating a change in the magnetic moment which is consistent with the breaking down of domains which we observe in XPEEM (Fig. 5.7). A maximum change of 33% was observed in XMCD L_3 peak. Similar to MOKE data, we see no direct relation with the applied electric field and the change in XMCD [Fig. 5.8(d)]. As observed in XPEEM, we find that the XAS of Co does not change significantly with the applied electric field [Fig. 5.8(b)], and a shift in the peak energy or broadening of peak was also not observed either, which we attribute to the lack of spatial resolution as we average over the entire sample. Due to the lack of systematic control over the magnetization, we were unable to perform time resolved XMCD characterization.

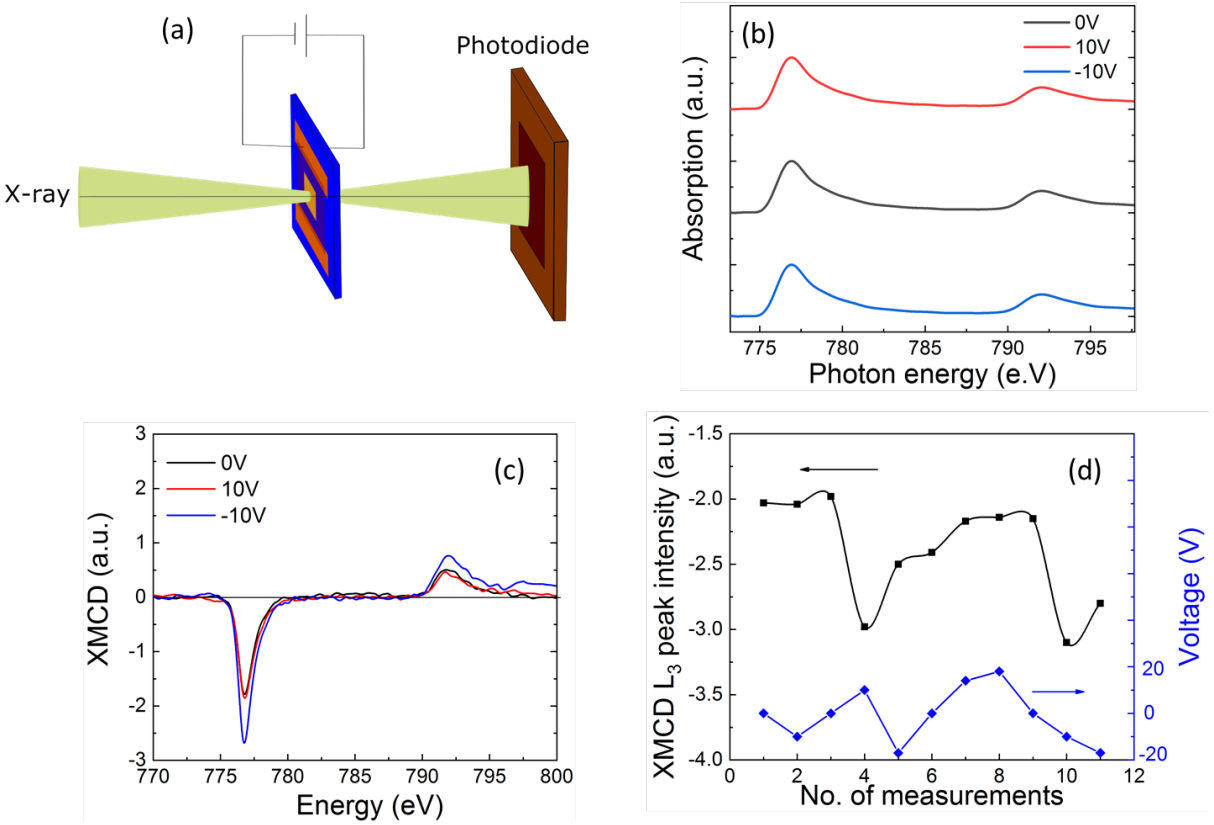

Figure 5.8: (a) Schematic of the transmission XAS measurement. (b) XAS for different values of applied electric field. (c) XMCD for different values of applied electric field (d) XMCD L_3 peak as a function of measurement sequence.

5.1.5 Dielectric characterization

Similar measurements were carried out in other Pt/Co/Pt heterostructures and we observe that most of the samples showed irreversible or random changes in domain configuration or coercivity with the applied electric field. To better understand this behavior, we characterized electrically the silicon nitride membranes by measuring the capacitance as a function of frequency using an LCR impedance meter; the results are shown in Fig. 5.9, where we find that the capacitance reduces with increasing frequency by almost a factor of 4 from 100 Hz to 100 kHz and to be compared to the ideal, frequency-independent capacitance of 86 pF (close to the value measured at 1 MHz, about 140 pF). At room temperature, the relative permittivity of silicon nitride does not change with frequency [169], hence, we attribute this effect to the presence charge defects/traps in the silicon nitride membranes. Even though silicon nitride is considered to be a good insulating material, the electrical and field effect properties can be affected by the deposition method, stoichiometry and the presence of oxygen used to produce low stress membranes. Such intrinsic defects result in the formation of charge traps [170] [171] [172] [173] [174] and efforts are being made to reduce/control the charge trap density [175] [176]. Since the mobility of carrier charges such as electrons is independent of the measuring frequency and we measure a higher capacitance at lower frequency, it is likely that we are also moving ions or possible vacancies in the Si_3N_4 with applied electric field along with the electrons, as ionic mobility with electric field is lower than electron mobility. Therefore, when an electric field is applied, we accumulate charges and/or ions at the interface and in turn change the interfacial anisotropy. Upon removal of the electric field, a number of charges remain trapped in the interface, pinning the Fermi level and the anisotropy in the modified state; further application of electric field leads to further accumulation of trapped charges at the interface and a new modification of the interfacial anisotropy in an irreversible manner (within the time of measurement), which can be related to our observations in MOKE and XPEEM. Therefore, for a systematic control of magnetization, the quality of the silicon nitride, especially the stoichiometry, should be taken into account for gated devices. In fact, as silicon nitride was considered for electrically read-only and flash memory devices [141], and also used as a charge trapping device to store informa-

tion [142], it may be possible to combine magnetoelectric coupling in silicon nitride gated devices and its charge trapping effects for future MRAM or memory devices. With defect free membranes, we expect a better magnetoelectric coupling which can be used for high frequency characterization and applications. Our result shows the importance of charge defects in dielectrics that can significantly affect the magnetoelectric coupling, therefore we perform electrical characterization using LCR meter on different dielectrics, and we find that all dielectrics including stoichiometric S_3N_4 shows significant charge defects or charge traps. A detailed description of the charge defects on dielectrics is described in chapter 7.

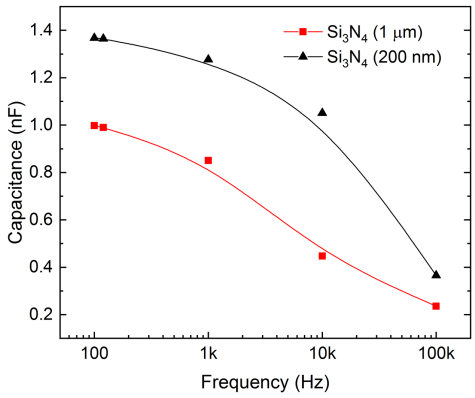

Figure 5.9: Capacitance of silicon nitride membranes as a function of frequency. Figure adapted from ref. [134].

In summary, we have demonstrated the presence of a magnetoelectric coupling in silicon nitride gated Pt/Co/Pt heterostructures using XPEEM and MOKE. From XPEEM we find that we can control the DW fluctuation rate and DW patterns using an electric field; in both cases we change the anisotropy of the system with an applied electric field. We also demonstrate the coexistence of both IP and OOP magnetization components which is attributed to surface roughness; in such systems, the IP magnetization is found to be more sensitive to the applied electric field and the control in domain wall pattern is systematic. Due to charge defects and charge traps hampering the systematic control in the magnetoelectric coupling, high frequency characterization cannot be performed. Therefore, it is important that good quality silicon nitride membranes are

used for gated devices. With optimized growth process, silicon nitride can be a potential candidate as gate dielectric in magnetoelectrically coupled devices for future electric field control MRAM or storage devices. In the next chapter, we investigate the magnetoelectric coupling in Si_3N_4 gated Ta/Co/Pt heterostructures with a net DMI and with a possible presence of skyrmions and also discuss the origin of the presence of IP and OOP domains.

Chapter 6

Spin structures and magnetoelectric coupling in Si_3N_4 gated Ta/Co/Pt heterostructures

Interfacing magnetic materials with non-magnetic metals such as Pt with large spin orbit coupling (SOC) results in an asymmetric exchange interaction at the interface due to the Dzyaloshinskii-Moriya interaction (DMI) which leads to the formation of skyrmions and topological spin structures. Until now, skyrmionic structures were only observed in magnetic multilayer thin films with out-of-plane (OOP) magnetic anisotropy and there are two types of skyrmions that have been experimentally observed, namely Bloch and Néel skyrmions. Skyrmionic structures have never been observed on samples with in-plane (IP) anisotropy. Here we demonstrate that, on a trilayer of Ta/Co/Pt thin film with DMI, in combination with surface roughness, one can obtain an OOP spin structure in a sample with IP anisotropy whose spin structure resemble the conventional Néel skyrmion. By using X-ray photoelectron emission microscopy (XPEEM), we observed OOP spin structures surrounded by IP spins, where the OOP spin structures have lateral dimensions from 200 nm to 2 μm. Furthermore, we find that these spin structures can be manipulated by electric fields similar to what was observed in the previous chapter, through a change in the interfacial anisotropy and possibly DMI.[1]

[1]The sample preparation, fabrication, magneto-optic Kerr effect (MOKE) characterization, atomic force microscopy was performed by me. XPEEM characterization was performed by Dr. Carlos A. F.

6.1 Magnetic spin structures of Ta/Co/Pt

Ta/Co/Pt heterostructures with perpendicular magnetic anisotropy have a net DMI and are known to form skyrmions [78] [177]. The origin of a net DMI in Ta/Co/Pt heterostructures is due to the asymmetric interface (in symmetric interfaces the DMI cancels out; however, for a symmetric interface such as Pt/Co/Pt small magnitude of DMI can still be present [178]). Skymions are usually present in samples with strong OOP anisotropy and to investigate skyrmions in Ta/Co/Pt heterostructures, a multilayer structrue is fabricated in order to obtain a strong perpendicular magnetic anisotropy. However, for investigating the charge-mediated magnetoelectric coupling, we keep the thickness small to maximize the magnetoelectric coupling effect. Until now skyrmionic structures in an IP anisotropy systems have not been reported, this is because thin films with in-plane anisotropy have Néel wall [84] and are expected to be non-chiral [77].

The coexistence of IP and OOP domains can be achieved by engineering the anisotropy of the system through surface roughness [179] [180], or in a multilayer stack of IP and OOP layer, where the OOP layer can induce an anisotropy in the IP layer through exchange bias effect [181] [182] or by a dipolar coupling [77]. The presence of IP and OOP components can also be observed in a single film at the spin reorientation transition (SRT) due to the easy axis pointing at a 45° angle to the surface [183] [184]. In the following section we show that OOP spin structures can be induced in dominant IP surrounding by DMI and such domains with larger dimension can then be stabilized by a rough surface.

The sample preparation follows the same procedure described in the previous chapter, except that the 1 nm Pt electrode interfacing the silicon nitride is replaced by 1 nm Ta layer. The thickness of Co layer is set to 6.5 Å. The sample was grown using magnetron sputtering with base pressure of 10^{-7} mbar.

6.1.1 OOP spin structures in a dominant IP surrounding

The sample with Ta/Co(6.5 Å)/Pt on Si_3N_4 was characterized with magneto-optic Kerr effect (MOKE) to verify the anisotropy of the system. Figure. 6.1(a-b) shows the MOKE

Vaz, Mr. David Bracher and me. Codes for image reconstruction were developed by me with the help from Dr. Carlos A. F. Vaz.

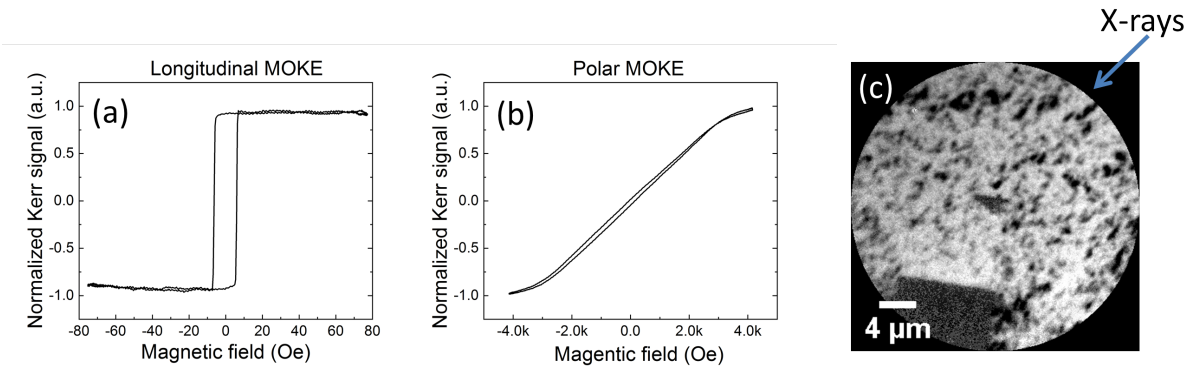

Figure 6.1: (a-b) MOKE characterization and (c) XMCD image of Ta/Co(6.5 Å)/Pt heterostructure.

characterization results where we observe an easy axis hysteresis in the longitudinal MOKE configuration and a hard axis hysteresis in the polar MOKE configuration, indicating a favourable IP anisotropy in the system. We also measured the saturation magnetization (M_s) from SQUID (superconducting quantum interference device) magnetometry and we calculated the anisotropy energy values using the equation $K_u = H_{sat}M_s/2 - 2\pi M_s^2$ ($\vec{H}$ is applied OOP plane to the sample), where H_{sat} is the saturation magnetic field determined from MOKE; when $K_u > 0$, the easy axis points OOP, with the effective anisotropy overcoming the shape anisotropy. We estimate for Ta/Co(6.5 Å)/Pt, K_u(OOP) = -11.1 $\times$ 10^6 erg/cm^3 suggesting that the easy axis is still IP and the sample still has a strong OOP anisotropy (shape anisotropy = 13.5 $\times$ 10^6 erg/cm^3), however not enough to overcome the shape anisotropy. By applying $\vec{H}$ in IP easy and hard axis we find the IP anisotropy to be K_u(IP) = 1.26 $\times$ 10^5 erg/cm^3.

Before XPEEM characterization, the sample was demagnetized using a 15 mT AC magnetic field and XPEEM characterization was performed at room temperature under ultra high vacuum ($< 10^{-10}$ mbar). Fig. 6.1(c) shows the X-ray magnetic circular dichroism (XMCD) image of the domain structure of a Ta/Co(6.5 Å)/Pt heterostructure, where we observe irregular shaped dark contrast domains in a white background.

To investigate the possible presence of skyrmions we rotated the samples with respect to the X-ray propagation direction, as performed in the previous chapter to determine the IP and OOP spins. If the dark contrast domains were Bloch type skyrmions, the absorption within the structure should change when the sample is rotated with respect

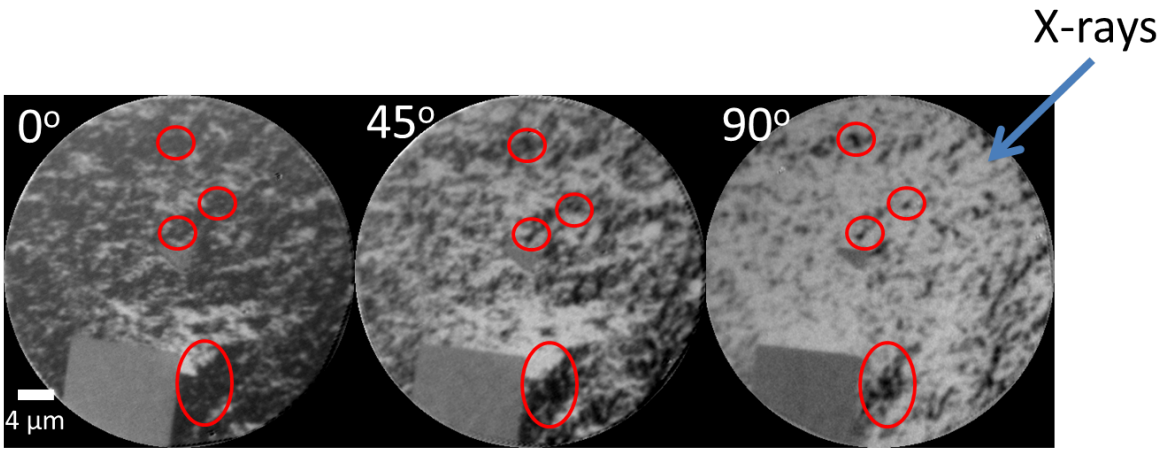

Figure 6.2: XMCD image of Ta/Co(6.5 Å)/Pt acquired at different angles.

to the X-rays, while if the spin structures are Néel type skyrmions, the absorption in the domain wall will change due to IP Néel wall as observed in ref. [115] [96]. Figure. 6.2 shows the XMCD images of the Ta/Co/Pt sample imaged at 0°, 45° and 90° with respect to the X-rays. From these images one can find that the majority of the regions change magnetic contrast, indicating an IP magnetization, while certain dark contrast domains encircled in red show no change in magnetic contrast indicating OOP magnetization; we also find certain OOP domains with white contrast to remain unchanged at different angles. From these observations it is clear that the domains which did not change the magnetic contrast are not Bloch type skyrmion and at the same time since changes in the domain wall cannot be resolved we cannot conclude whether the structures are Néel type skyrmions. With the given anisotropy value, and keeping the exchange stiffness 1×10^{-11} J/m [78] we obtain for the width of the domain wall ($t = \sqrt{A/K_{eff}}$) about 3 nm.

Nevertheless, even though the spin structure cannot be resolved to confirm the presence of skyrmions, it is clear that the sample shows the simultaneous presence of both IP and OOP domains. In the previous chapter, we identified the presence of IP and OOP domains by visual analysis, here, we perform a quantitative analysis of the images (Fig. 6.2) to extract the components of the magnetization vector (M_x, M_y and M_z) from each pixel and obtain a clear insight into these spin structures. To extract the magnetization components one needs to solve the angular variation of the X-ray absorption at each pixel.

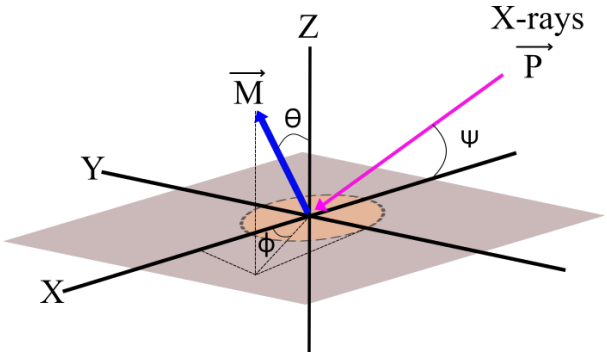

Figure 6.3: Measuring geometry and magnetization vectors in polar coordinates.

The magnetization components can be expressed in polar coordinates (Fig. 6.3) as

$$M_x = M\cos\Phi\sin\theta, M_y = M\sin\Phi\sin\theta, M_z = M\cos\theta \tag{6.1}$$

where θ is the polar angle and Φ is the azimuthal angle. Here M corresponds to the intensity of individual pixels. The polarization vector can be written as,

$$\vec{P} = P(\cos\psi, 0, \sin\psi) \tag{6.2}$$

where ψ is the incident angle of the X-rays (16°), and the intensity at a pixel at different angles is given by,

$$I_{0°,45°,90°} \propto \vec{M}_{x,y,z}.\vec{P} \tag{6.3}$$

By solving the three linear equations derived from the above general expressions, one can extract the magnetization components at each pixel. Before performing the analysis, the images are corrected for drift and lens distortion; due to thermal fluctuations or domain nucleation, some regions on the images are not considered for the analysis. The analysis was performed using Matlab codes developed in-house [185]. The extracted vectors are then converted into a format suitable to be visualized in the OOMMF micromagnetics and Paraview software. After extracting the magnetization vector, the total magnetization amplitude $M = (M_x + M_y + M_z)^{1/2}$ was analysed. If the domains were not moving with time, M should be constant throughout the sample, however, due to the issues related to the normalization and intensity fluctuations a 20% variation was allowed, and the regions whose M value is within this margin is extracted. Figure. 6.4(a-c) shows the zoom-in image of XPEEM images used for the analysis along with the reconstructed image (Fig. 6.4) visualized with the OOMMF software. The reconstructed image shows

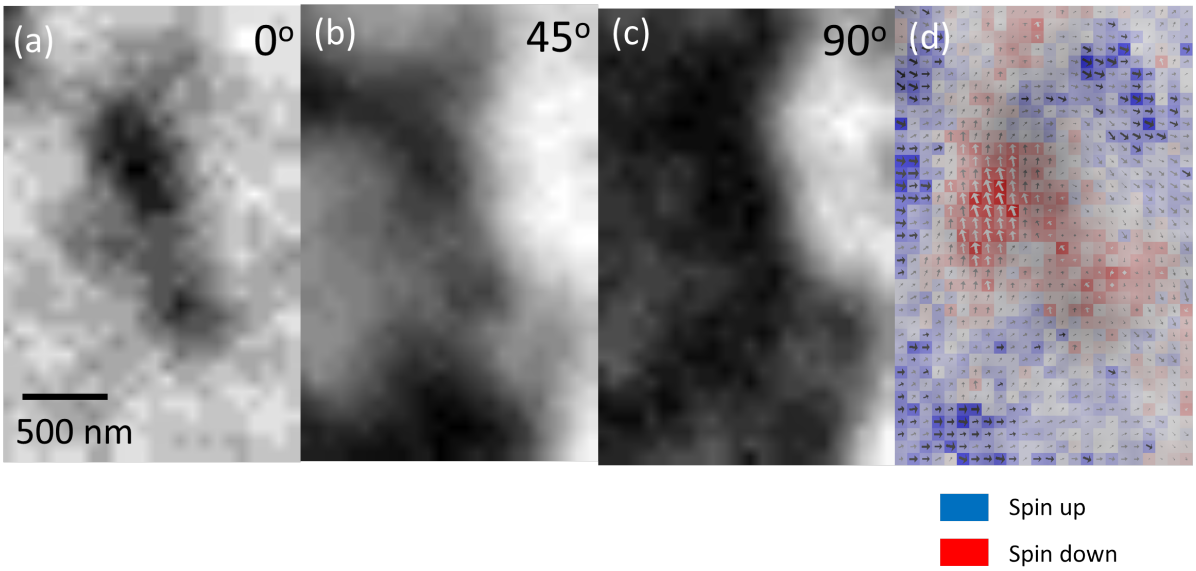

Figure 6.4: Zoomed in XMCD images of the Ta/Co(6.5 Å)/Pt heterostructure acquired at different angles and the corresponding image of the reconstructed magnetization vector.

more accurately the regions which have perfect OOP spins as indicated by red and blue colour, corresponding to spin up and down respectively. The OOP spin structures have a lateral dimension varying from 200 nm to about 2 μm. To confirm that the OOP spin structures are not created due to pinning sites, we imaged the same spot many times after demagnetizing the sample and find new domain structure with different distribution of OOP spin structures.

A series of samples with fixed Ta, Pt layer and different Co thickness varying from 3 Å to 10 Å were produced and characterized using XPEEM. The presence of simultaneous IP and OOP spin structures is observed from Co thickness of 5.5 Å up to 7-8 Å. At 10 Å thick Co all the domains were IP. The domain patterns acquired for different Co thickness is shown in Fig. 6.5.

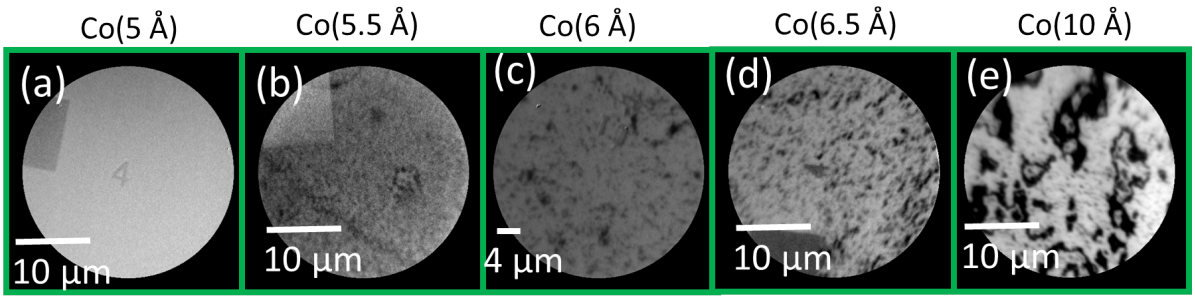

Figure 6.5: XMCD images of Ta/Co/Pt with Co thickness from 5 Å to 10 Å.

6.1.2 Effect on Magnetic field

To extract the DMI value of a skyrmion, magnetic field pulses are applied to the sample, and based on the domain wall velocity the DMI value is extracted, this method is known as symmetric bubble expansion method [178], and it is employed to find the DMI for both Bloch type and Néel type skyrmions. However, with applied pulse magnetic field to our sample, the changes in the domain wall was not observed. Therefore, we characterized the OOP spin structure with applied DC magnetic field.

Effect of IP plane magnetic field

The IP magnetic field was ramped up in small steps up to 2 mT which is above the coercive field (1.8-1.9 mT) of the Ta/Co/Pt sample, and XMCD images acquired at 0 mT and at 2 mT are shown in Fig. 6.6(a). With IP magnetic field of 2 mT the IP magnetization on the sample rotated towards the direction of the magnetic field, which is accompanied with a change in the OOP magnetization from spin up to spin down or vice versa; this indicates that there is a coupling between the IP and OOP spins [a zoomed in image is shown in Fig. 6.6(b-c)].

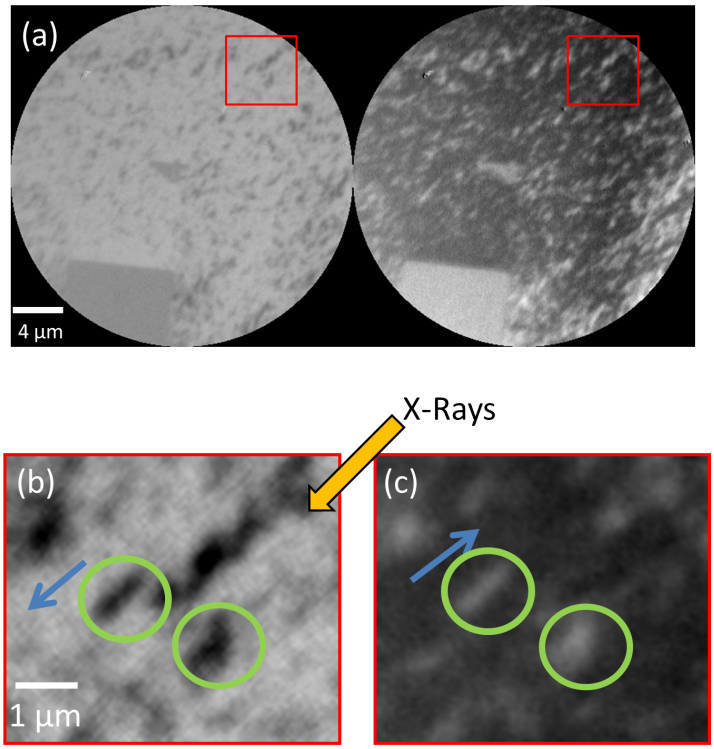

Figure 6.6: (a) XMCD image of Ta/Co/Pt acquired at 0 mT and after applying 2 mT of IP magnetic field. (b-c) Zoomed in image of 0 mT and 2 mT of the red square in (a); the blue arrow indicates the direction of the IP spins and green circle indicates the OOP spins.

This process was reproducible and the OOP spin always flipped when the IP spins change. At sufficiently large IP magnetic field strength, the OOP domains rotate to IP and do not reappear when the IP magnetic field was reversed. In the next step we investigate the effects of the OOP magnetic field.

Effect of OOP plane magnetic field

An OOP magnetic field up to 2.5 mT was applied in small steps and the corresponding XMCD images were acquired. From the XPEEM images shown in Fig. 6.7(a) we find that the OOP magnetic field have no effect on the IP spins, however at 2.5 mT we find almost all OOP spin structures change contrast from white to black.

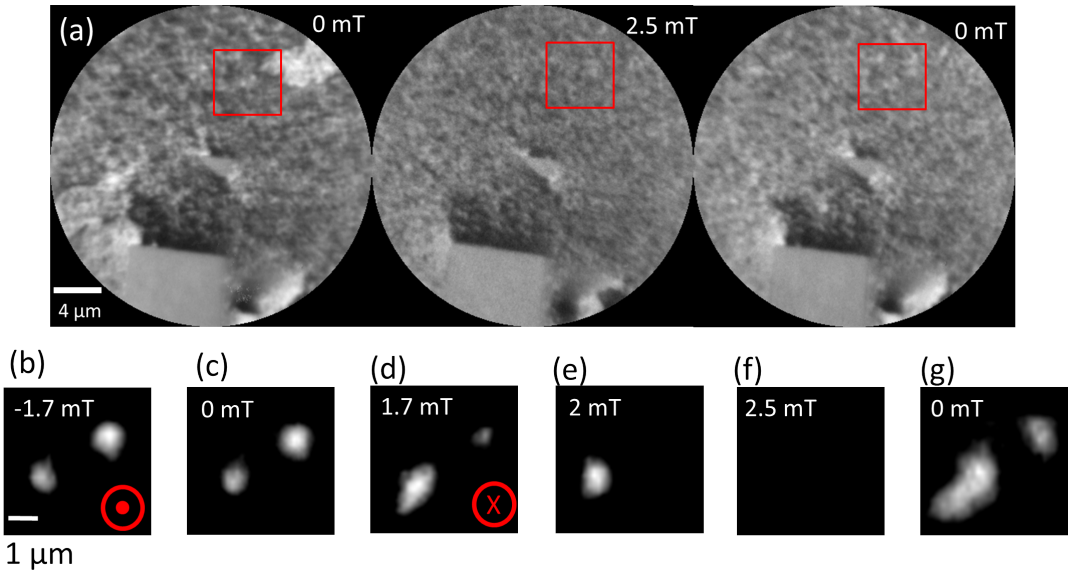

Figure 6.7: (a)XMCD images acquired at 0 mT, 2.5 mT and 0 mT. (b-g) XMCD images of an OOP spin structure in Ta/Co/Pt as a function of OOP magnetic field.

Figure 6.7(b-g) shows a zoomed-in image sequence of OOP spins with OOP magnetic field from -1.7 mT to 2.5 mT. When the magnetic field was in the direction of the OOP spin orientation (at -1.7 mT), we find that the OOP spin structure remain largely unchanged [Fig.6.7(b-c)]. However, by reversing the magnetic field we were able to change the shape of the OOP spin structure and at about 2.5 mT, the OOP spin structure flipped and remained in the same state until the magnetic field was removed. Then, upon removal of the magnetic field, the OOP spin structure flipped back to its initial configuration. This effect is reproducible and again confirms that the IP and the OOP spins are coupled. The orientation of the OOP spins is dependent on the IP spins and the OOP plane spins remain in the same orientation as long as the IP spins are unchanged and change only by applying a IP magnetic field. Such behaviour suggest the presence of a possible chirality between the IP and OOP spins.

6.1.3 Origin of such OOP spin structures

To understand the origin of the simultaneous existence of IP and OOP spin structures, we consider the effect of roughness and the presence of DMI in the system. Therefore, we make a comparative investigation on Pt/Co/Pt and Ta/Co/Pt heterostructures grown

on smooth SiO_x substrate with a roughness value rms of < 0.5 nm and on silicon nitride membrane with a roughness value rms of over 1.2 nm. Figure 6.8 shows the atomic force microscopy images and the roughness profile of SiO_x substrate and Si_3N_4 membrane, where a clear difference in the surface morphology and roughness can be observed.

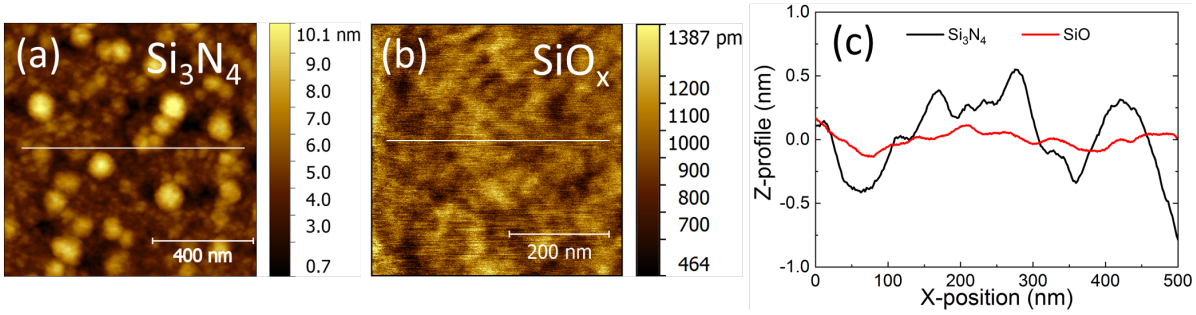

Figure 6.8: Surface topology of (a) silicon nitride membrane and (b) silicon substrate. (c) Roughness profile of silicon nitride membrane and of the silicon substrate.

After the deposition, the samples are then characterized using MOKE to determine the magnetic anisotropy of the system. Figure. 6.9(a,b) shows the longitudinal and polar MOKE characterization of Ta/Co/Pt on Si_3N_4 and on SiO_x. We observe that the longitudinal hysteresis on Ta/Co/Pt on SiO_x is smaller than on Si_3N_4, and for the polar MOKE, the hard axis has a saturation field of over 4 kOe in the Ta/Co/Pt grown on Si_3N_4 while a saturation field of Ta/Co/Pt grown on SiO_x is 2 kOe, which confirms that the system has a stronger IP anisotropy on Si_3N_4. The samples were grown simultaneously, therefore we attribute the difference in behaviour to the surface roughness.

Similarly, Fig. 6.9(c,d) shows the longitudinal and polar MOKE characterization of Pt/Co/Pt on Si_3N_4 and SiO_x; we find that the Pt/Co/Pt shows OOP anisotropy on SiO_x substrate and simultaneous IP and OOP easy axis hysteresis loop on Si_3N_4 substrate. On the Si_3N_4 substrate, we observe that the coercivity of the IP easy axis hysteresis is larger than the OOP easy axis hysteresis which further indicates that the rough surface forces the system to have a strong IP anisotropy irrespective of the bottom metal layer (Ta or Pt).

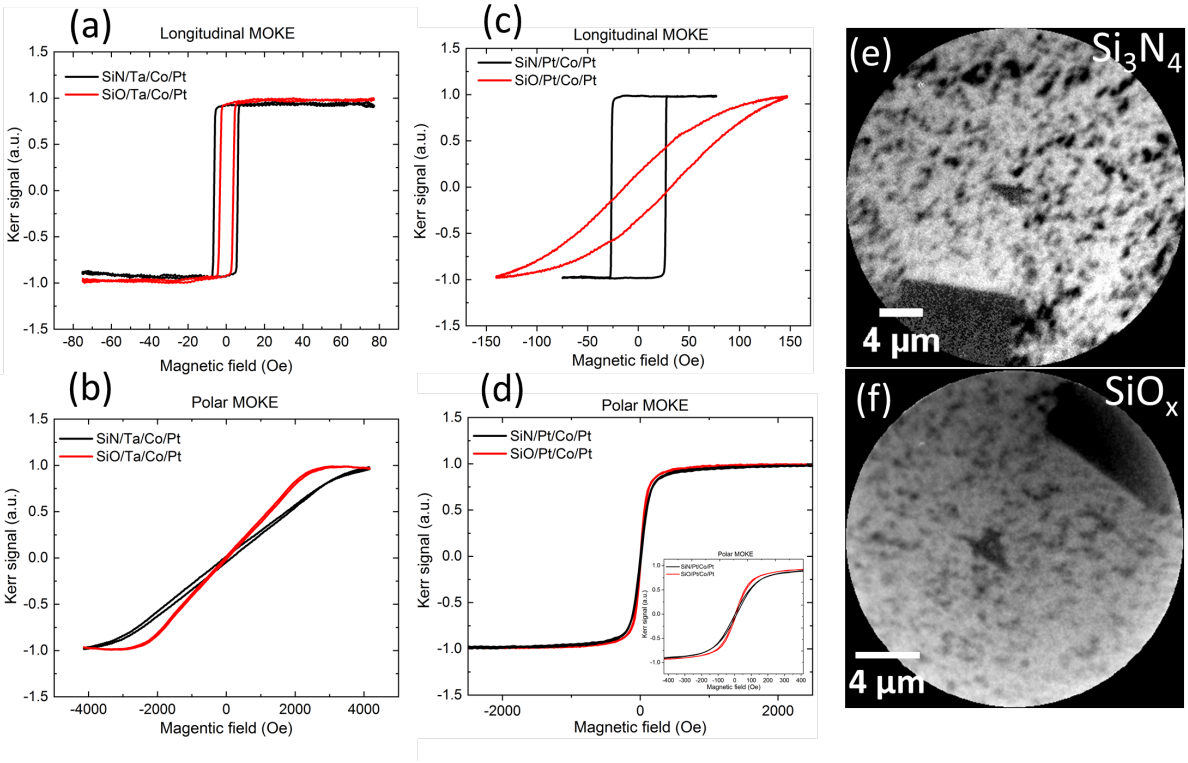

Figure 6.9: (a,b) Longitudinal and polar MOKE characterization of Ta/Co/Pt heterostructure grown on Si_3N_4 and SiO_x. (c,d) Longitudinal and polar MOKE characterization of Pt/Co/Pt grown on Si_3N_4 and SiO_x. (e-f) XMCD image of Ta/Co/Pt grown on (e) silicon nitride membrane (f) silicon substrate.

The sample was demagnetized and then characterized in XPEEM. Figure. 6.9(e,f) shows the domain configuration of Ta/Co/Pt on Si_3N_3 and SiO_x, where we find a similar domain configuration with dark contrast OOP domain surrounded by bright contrast domains from IP spins. By analysing the XPEEM image sequence, we find that the OOP spin structures on SiO_x are unstable due to thermal fluctuations while on Si_3N_4 the structures appear more stable with no or less thermal fluctuations. We also find that the size of the OOP spin structure on Si_3N_4 is comparatively larger than on SiO_x. Applying an IP magnetic field on the sample grown on SiO_x resulted in similar behaviour such that the OOP magnetization flipped when the surrounding IP spins rotate as shown in Fig. 6.10, however the change in the OOP spins with OOP magnetic field could not be resolved. The XPEEM data together with atomic force microscopy and MOKE confirms that roughness induces an IP anisotropy and is necessary to stabilize larger dimension

OOP spin structures as observed on samples grown on Si_3N_4. Since we also observe the OOP spin structures on smoother SiO_x substrate, therefore the formation of OOP spin structure in dominant IP spins is attributed to the presence of DMI induced by the asymmetric interface, and the surface roughness being a less critical factor. Similarly, the strong coupling between the IP and the OOP spins observed when an magnetic field was applied is also attributed to the presence of DMI as we observe the same effect on smooth and rough surfaces.

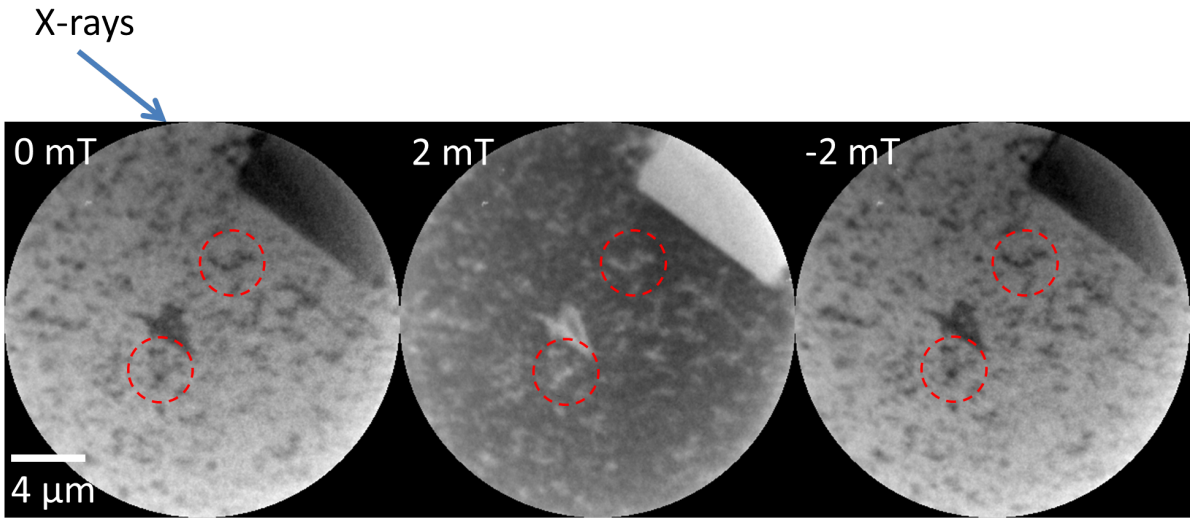

Figure 6.10: XPEEM image sequence of Ta/Co/Pt on SiO_x, where the OOP spin structures (indicated in red circles) flip from up to down depending the surrounding IP spins.

Next we make a comparison between the XPEEM images of Pt/Co/Pt and Ta/Co/Pt heterostructures. Figure. 6.11(a-b) shows the domain structure of Pt/Co/Pt heterostructures for Co thickness of 6 Å and 6.5 Å. The former have a dominant OOP anisotropy with a labyrinth like domain structure, while the latter shows the coexistence of IP and OOP spins; for Co thickness < 6 Å a strong OOP anisotropy with a monodomain state is found. The Ta/Co/Pt series shown in Fig. 6.5, however, display a coexistence of IP and OOP spins already at 5.5 Å. The OOP spin structures on Ta/Co/Pt are much larger and stable, while they are smaller in Pt/Co/Pt samples and observed only at a thickness very close to the SRT. Taking these clear differences into account, it is clear that the presence of DMI induced by the asymmetric interfaces is responsible for the formation of the OOP spin structures. The Pt/Co(6.5 Å)/Pt structures discussed in the previous chapter, have

coexistence of IP and OOP domains despite having a symmetric interface. In this case we attribute the formation of such spins structures to the combination of SRT, rough surface and also to the possible presence of DMI, as symmetric interfaces can also have a small non-zero DMI value [178].

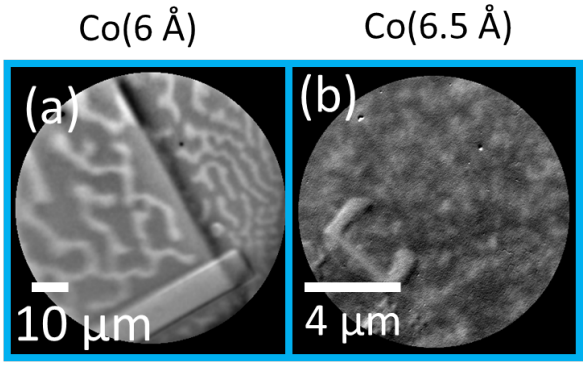

Figure 6.11: XMCD image sequence of Pt/Co/Pt with Co thickness of 6 Å and 6.5 Å.

Based on the XPEEM results, a DMI is required to have an OOP spin structure in dominant IP spins. Therefore, it is possible that these spin structure can be skyrmionic or topological in nature and may resemble a Néel skyrmion like structure. There are two possibilities that such OOP spin structure can be formed, if the OOP spin structures have Néel wall and spins are aligned as shown in Fig. 6.12(a) then the structure is topological in nature with $Q = +1/2$, however, if the domain wall of the structure is similar to Fig. 6.12(b), then the OOP spin structures are not topological. Micromagnetic simulation in principle could help to address the nature of the domain wall.

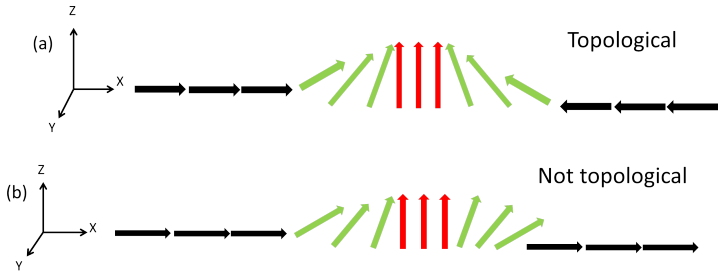

Figure 6.12: Spin orientation of OOP spin structure in IP surrounding: (a) represents the case with topological number as +1/2 and (b) represents the case which is non-topological.

6.2 Electric field control of the magnetic spin structure

The previous section described the type of spin structure that can form in a Ta/Co/Pt heterostructures grown on silicon nitride membranes. In this section we discuss the possibility of controlling such spin structures using electric fields. The ability to control skyrmions and skyrmionic structures using electric currents has been demostrated [79], however using electric field instead of electric currents can be more energy efficient and is therefore of high interest scientifically and technologically. Previous studies have demostrated that skyrmionic bubble stabilized under an applied magnetic field can be contolled by an applied electric field using different gate dielectrics [23] [24] [25] [26]. Here, we present the electric field control of the possible OOP skyrmion like spin structure stabilized under no magnetic field using XPEEM. The measurement geometry for this sample is same as that shown in the previous chapter. Here we show the results for the Ta/Co(6 Å)/Pt heterostructures. The domain configuration is similar to what was observed in Ta/Co(6.5 Å)/Pt, whose domain structure is shown in the previous section.

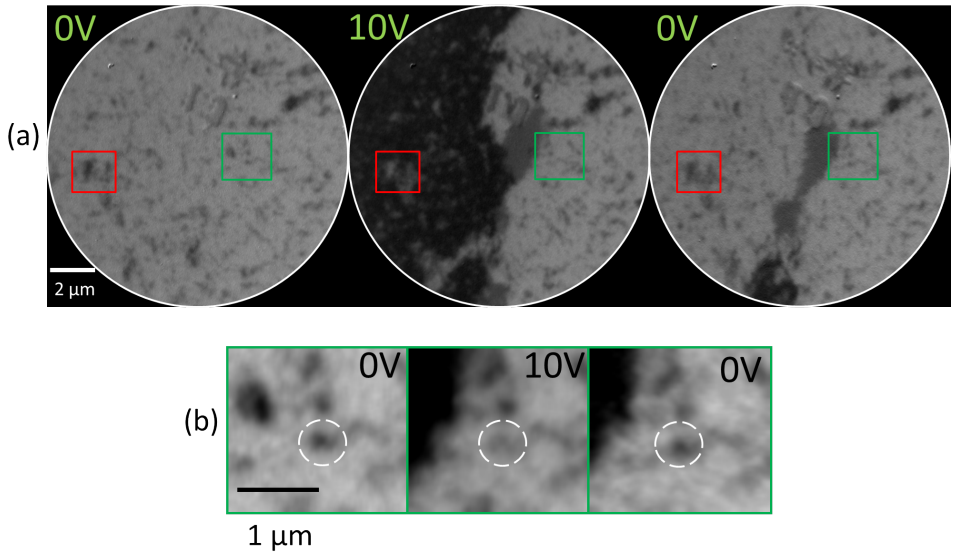

Figure 6.13: (a) XMCD image sequence of Ta/Co/Pt as a function of electric field. (b) Electric field control of OOP spin structure indicated by the green box in (a).

Figure 6.13(a) shows the image sequence of the magnetic spin structures acquired in

the voltage sequence of 0 V, 10 V and 0 V; from the image sequence, one can observe that the application of 10 V resulted in the formation of a dark contrast IP reverse magnetic domain covering half of the entire imaged area. In the regions where the IP reverse domain nucleated we observe the OOP spins to flip (Fig. 6.13(a) marked in red square), which suggests that the IP and OOP spins are still coupled. By removing the electric field, we find that the domains structure reappears going to initial configuration with some regions modified, a process which was found to be reproducible. We attribute the changes in the magnetization to the modulation of interfacial anisotropy similar to what was described in chapter 5, except we find larger changes in the IP magnetization, which we attribute to the possible influence of DMI. While most of the OOP spins can only be changed by changing the neighbouring IP spins, few OOP spin structures did respond to the applied electric field with no change in the neighbouring IP spins. Figure 6.13(b) shows a zoomed-in image sequence of an OOP spin structure marked in a green square in Fig. 6.13(a), where the OOP spin structure is annihilated with the applied electric field even when there is no change in the surrounding IP spins and reappear on the same spot upon removal of the electric field. We attribute these changes in the OOP spin structure to a change in the local anisotropy with the applied electric field and possibly DMI, as described by Schott et al. [24]; more experiments and simulations are required to obtain a quantitative estimate of the change in the DMI with electric field.

In summary, we have observed from XPEEM the simultaneous presence of IP and OOP spin structures at room temperature and at zero external magnetic field. We find that the formation of such spin structures is due to the presence of DMI and surface roughness is less critical. Due to the presence of DMI, it is possible that such spin structures are topological in nature. From magnetic field experiments we find that the OOP and IP spins are coupled, such that the OOP spins can only be controlled by changing the neighbouring IP spins. It appears that the OOP spins have a preferable orientation which is dependent on the surrounding IP spins indicating the presence of chirality. Finally we also demonstrated that such OOP spin structures can be controlled by applying an electric field by changing the overall anisotropy of the system and possibly the DMI. Our results suggest the possibility to engineer skyrmionic structures and their sizes by specifically inducing roughness on the substrate.

Chapter 7

HF characterization of dielectrics

In chapter 4 and 5, we showed that in strain- and charge-mediated magnetoelectric coupling no systematic control of magnetization could be obtained due to the high surface roughness and presence of charge defects, respectively, which prevented us to perform high frequency characterization. Therefore, in this chapter we investigate the electrical properties of different dielectrics and determine their potential for high frequency characterization of magnetoelectric coupling in composite structures. We characterized the dielectrics using an LCR impedance meter and vector network analyser as a function of frequency and gate voltage. We find that the capacitance of all dielectrics, both stoichiometric and non-stoichiometric, decreases with increasing frequency, suggesting the presence of an additional capacitance due to surface oxides or interfacial traps. We also find the presence of a negative voltage coefficient of capacitance in stoichiometric silicon nitride membrane from 3 kHz to 1 MHz, due to which the capacitance reduces with the applied gate voltage. Our results suggest that all dielectrics (Si_3N_4, MgO_x, AlN, Al_2O_x, $BaTiO_3$) could behave differently from the ideal dielectric at high frequency, therefore the electrical properties at high frequencies of a dielectric should be determined before considering it for a magnetoelectric coupling device for high frequency operation. [1]

[1]The sample preparation and fabrication was done by me. The dielectric deposition was done by Mr. Michael Horisberger, Dr. Laura Maurel Velazquez and me. The VNA measurements were carried out by Dr. Marcus Gaspar and myself. The LCR measurements were performed by me.

7.1 Charge defects and interfacial charge traps in dielectrics

Charge defects are point defects in a dielectric material which arise due to the presence of impurities or absence of an atom in the crystal lattice (vacancy). Such point defects can be charged and can affect significanlty the transport properties, thermal diffusion rates, trapping and recombination rates of electrons and holes [186]. Vacancies in general are positively charged species similar to holes, however their mobility under applied voltage is not similar to holes or any charge carriers. Vacancies are usually mobile at high temperatures, however, in thin films, vacancies can be mobile with the application of a large electric field [40]. Charge traps, on the other hand, are caused by the presence of interfacial states between the conduction and valence band. Most often these charge traps are present at the interface between a dielectric/semiconductor or dielectric/metal. The charge traps can trap charges or ions. The presence of interfacial charge traps can result in the modulation of the Fermi level or in pinning of the Fermi level [187]. For semiconductor devices, such charge traps are removed by performing chemical, thermal or plasma treatments. Vacancy charge traps have also been reported in dielectrics such as in HfO_2 [188], and it has also been shown that the presence of vacancies can also be a source of induced charge traps [189]. In magnetoelectric devices the electrical properties of the dielectric is often neglected or not properly characterized, as most of the characterizations are performed using DC voltages.

Most multiferroic heterostructures are fabricated with the ferromagnetic material directly interfacing the dielectric/ferroelectric material. While most such composites show a magnetoelectric coupling, the origin of such effect, whether due to charge modulation created by the ideal capacitance or by the possible native oxide/ interfacial oxide or even by the oxygen ion vacancy diffusion, is not differentiated. Such devices can indeed have a large magnetoelectric coupling, but the magnitude of the coupling may decrease at higher frequency as other charged particles such as ions or oxygen vacancies no longer influence the coupling as they do not respond to high frequency excitations.

The interfacial oxides/states can be considered as an additional capacitor in the circuit which increases the overall capacitance of the system by modulating more charges

along with the charges modulated by the ideal capacitance [187]. This phenomenon is commonly observed at the metal-oxide-semiconductor interface, where applying a gate voltage results in the formation of a dead oxide layer increasing the overall capacitance. Such interfacial states can also exist inside the dielectric and not necessarily on the surface. One way to identify such additional capacitance is to characterize the capacitance of the device as a function of frequency, as explained in detail in the next section.

7.2 Characterization techniques

One type of capacitance vs frequency measurement used to characterize the interfacial states is known as Castagné–Vapaille method [190] which is widely used to characterize interfacial states [187] [191] [192]. The principle behind this measurement is that, at low frequency, the capacitance measured will be a combination of the ideal capacitance (C_{ideal}) without contributions from defects and the capacitance caused by the interfacial states; at higher frequency, the interfacial states do not respond, resulting in the measured capacitance to be only from the ideal term. Then the capacitance due to interfacial charges can be calculated from the expression;

$$C_{IT} = C_{ideal}\left(\frac{C_{LF}}{C_{ideal} - C_{LF}} - \frac{C_{HF}}{C_{ideal} - C_{HF}}\right) \tag{7.1}$$

where C_{IT} is the capacitance due to interfacial states, and C_{LF} is the capacitance at low frequency, C_{HF} is the capacitance at high frequency. The value obtained here quantifies the overall interfacial states in the dielectric and cannot discriminate the location, for example, whether it is present on the surface or deep inside the material.

To characterize the capacitance with frequency we use an LCR impedance meter operating in the frequency range from 20 Hz to 1 MHz and a vector network analyzer (VNA) for the frequency range from 300 kHz to 100 MHz. The LCR and VNA measure the impedance (Z) of the device. The working principle of LCR meter may vary between instruments; a simple mesurement set-up may resemble a Wheatstone bridge with a reference impedence from which the impedence of the sample is measured [193]. Similarly, a VNA also measures the impedance of the material using transmission line theory, where the impedance is measured in the form of a scattering parameter (S) which is analysed

to extract the impedence (Z), from which other lumped elements including capacitance (C) can be extracted [194]. The VNA is more sensitive than LCR meter, however a VNA requires a more accurate and careful calibration to extract the correct value of the capacitance (or other elements). Small details such as the length of the bonding wire can result in a wrong measurement.

The LCR measurements were carried out using BK Precision model 895 and VNA measurements were performed using Hewlett Packard model 8753B network analyser. Prior to the measurements the instruments were calibrated using a reference sample holder without the sample or the wire bonds.

7.3 Sample preparation

For characterizing silicon nitride, we used the samples that were characterized in the previous chapters. As a reference, stoichiometric silicon nitride membranes with the same dimensions (thickness 200 nm, area of the window, 500 $\times$ 500 μm^2) were purchased from Norcada Inc and a similar deposition process was performed to fabricate the top and bottom electrodes. The low stress silicon nitride membrane and the stoichiometric silicon nitride membranes both have a Pt/Co/Pt layer as one of the electrodes. Other dielectrics which were prepared include Al_2O_x, AlN_x, MgO_x deposited by reactive sputtering, and $BaTiO_3$ deposited by pulsed laser deposition. All the dielectrics except the silicon nitride have a thickness of 50 nm and area of 300 $\times$ 300 μm^2. The fabrication process is shown in Fig. 7.1. In the first step we pattern the bottom electrode by e-beam lithography with 15 nm thick Pt, since at this thickness the surface roughness of Pt is similar to the bottom Si substrate and the resistance of the Pt layer is $< 10\ \Omega$. In the second step, the dielectric was deposited at the center of the substrate. In the last step a 100 nm Cu top electrode was patterned. The samples are then mounted on a sample holder (from the PolluX beamline) which has a coplanar wave guide for electrical contacts, suitable for high frequency characterization.

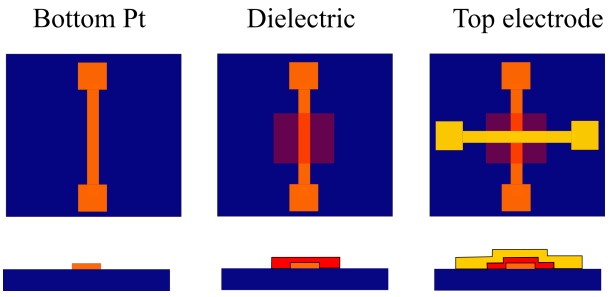

Figure 7.1: Sample preparation process for dielectric characterization.

7.4 Capacitance vs Frequency

Figure 7.2 shows the C vs Hz dependence of different dielectrics measured using the LCR impedance meter, where all the dielectrics show a similar trend of a decrease in capacitance with increase in frequency. All dielectrics, except the stoichiometric silicon nitride membrane, showed a change in capacitance by a factor of 4 or even by two orders of magnitude between 20 Hz and 1 MHz. For Al_2O_x and AlN_x we find that the capacitance is saturating at around 500 kHz and 100 kHz, respectively; for MgO the capacitance starts to saturates at 100 kHz and for stoichiometric Si_3N_4 the capacitance starts to saturate from 1 kHz. The capacitance of $BaTiO_3$ and non-stoichiometric Si_3N_4 did not saturate up to 1 MHz and we find that the capacitance continues to decrease further. The capacitance value of all the dielectrics at 20 Hz and 1 MHz, the ideal capacitance, and the interfacial states thus obtained are summarized in Table. 7.4, where we find that stoichiometric silicon nitride has the lowest capacitance arising from the interfacial charge traps, and the value of interfacial capacitance for other dielectrics are comparable to the capacitance measured at low frequency. The interfacial capacitance for the other dielectrics is significantly higher than the ideal value itself, suggesting a significant amount of charge defects within the dielectric, as the contribution from the surface oxides to the total capacitance is very small (about 6.14 pF as observed in stoichiometric membrane). The presence of large charge defects is attributed to off-stoichiometry in the chemical composition of the sample, as most of these samples are prepared by reactive sputtering. Our results confirm the requirement for a stoichiometric dielectric so as to obtain a consistent charge displacement at the interface at both low and high frequency range,

required in a magnetoelectric device. In the next step we characterize the capacitance variation with frequency at different bias voltages.

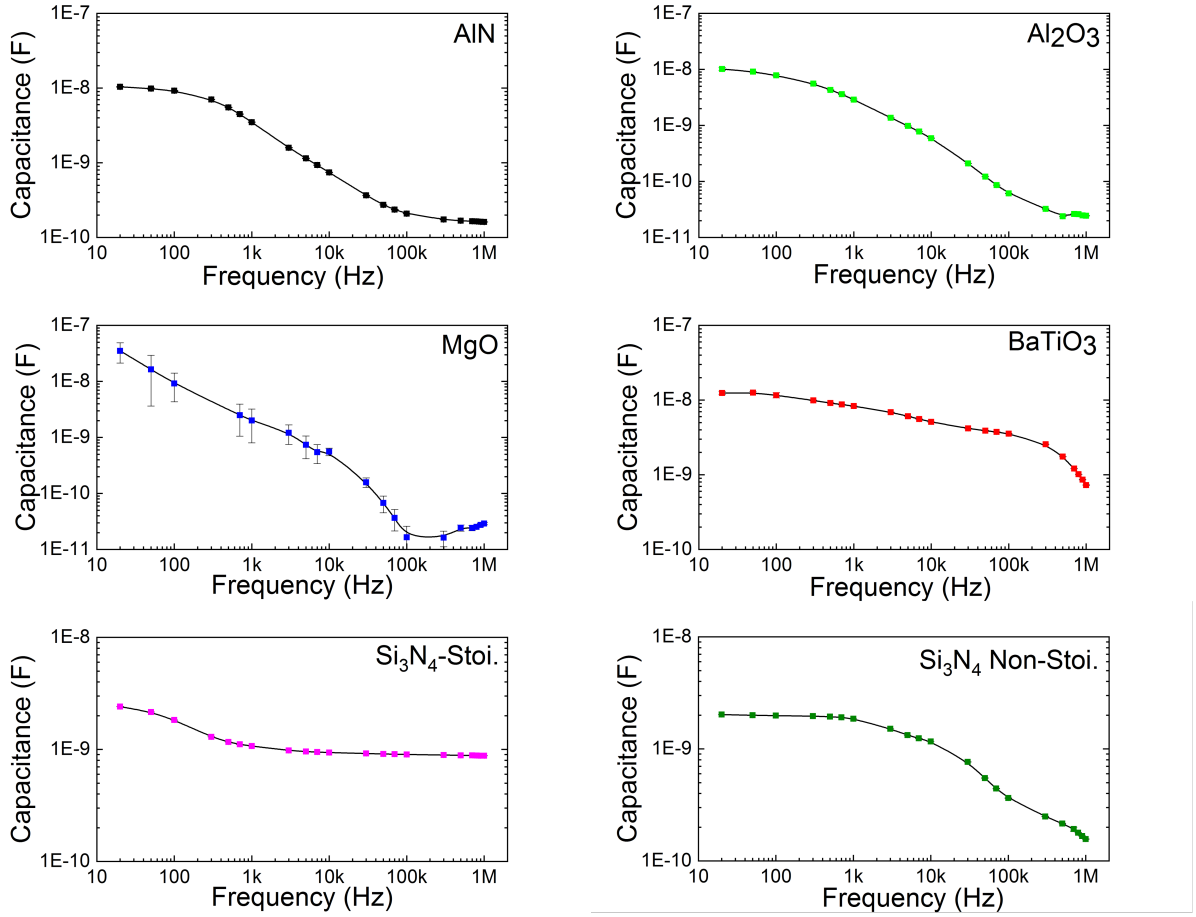

Figure 7.2: C vs Hz for different dielectrics measured using the LCR impedance meter.

Dielectric	ϵ	C_{LF} (nF)	C_{HF} (nF)	C_{IT} (nF)	Ideal value (nF)
Si_3N_4 Stoichiometric	7.5	2.4	0.8 (saturates)	6.14 $\times 10^{-3}$	0.086*
Si_3N_4 Non-stoichiometric	7.5	2.02	0.15 (saturates)	0.1	0.086
MgO	9.5	35.1	0.03	0.18	0.15
$BaTiO_3$	100#	12.4	0.72	8.6	1.59
AlN	8.5	10.4 nF	0.16(saturates)	0.69	0.13
Al_2O_x	9.5	10.1	0.02 (saturates)	0.18	0.15

Table 7.1: Summary of capacitance values, C_{LF}, C_{HF} obtained from Fig. 7.2 together with the ideal value and capacitance of interfacial states (C_{IT}). *The ideal capacitance calculated may not be accurate as the silicon frame in stoichiometric membrane has low resistivity, which means that the real area of the capacitor may not be 500×500 μm^2. #The dielectric constant is taken for amorphous $BaTiO_3$ [195].

7.5 Capacitance vs Voltage

Figure 7.3 shows the capacitance vs voltage measured at different frequencies for stoichiometric and non-stoichiometric Si_3N_4 membranes. For stoichiometric Si_3N_4 we find that the capacitance decreases with both positive and negative applied voltage and is consistent from 3 kHz to 1 MHz, while the non-stoichiometric Si_3N_4 show an increase in capacitance with negative voltage and a decrease with positive voltage up to 50 kHz; for frequencies $>$ 100 kHz the capacitance no longer changes with the applied voltage. For an ideal capacitor the capacitance should not change with applied DC bias voltage, however, in an non-ideal case or a capacitor with a high dielectric constant, a change in capacitance may be expected.

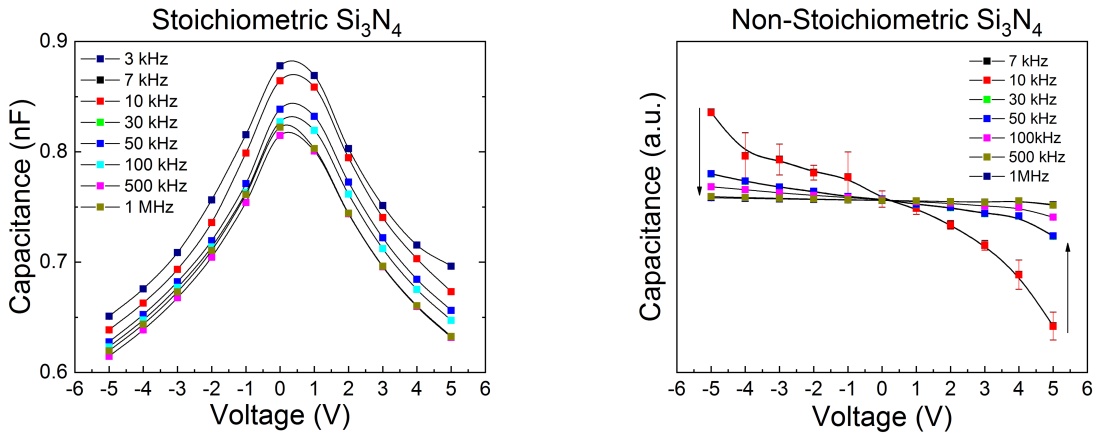

Figure 7.3: C vs V at various frequencies for stoichiometric and non-stoichiometric silicon nitride membranes.

The dependence of the capacitance on the applied voltage is given by the voltage coefficient of the capacitor as [196] [197] [198]:

$$C(V) = C(0) + \beta V + \alpha V^2 \tag{7.2}$$

where $C(0)$ is the capacitance under zero bias, α and β are the quadratic or linear voltage coefficients respectively, which vary for different materials. A positive quadratic value of α is due to ionic polarization arising from induced dipoles, while a negative α is due to the orientation of the permanent dipoles [198]. A positve α results in an increase in capacitance with applied electric field in both directions and the opposite occurs with negative α value. For capacitive devices, it is important to have α close to zero as possible; although such values can be obtained in low dielectric constant materials, for high dielectric constant material, obtaining a zero value for α is difficult. A negative value of α has been observed in $SrTiO_3$ [197] and SiO_2 [199], which have been proposed to be used in combination with positive value α material to bring the overall α to zero.

As the next step we fit eqn.(7.2) with C-V measurement, fit performed for the stoichiometric membrane is shown in Fig. 7.4, where we were not able to obtain a perfect fit for the curve even though the stoichiometric silicon nitride membranes show a trend with a negative value of α. This behaviour is different from what was reported in [197] [199] [198] and the origin is unclear.

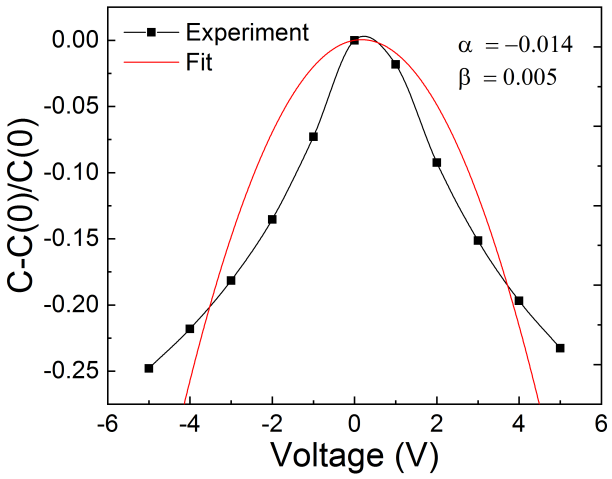

Figure 7.4: Normalized capacitanve vs V at 1 MHz and the fit using capacitance voltage coefficient represented in eqn.(7.2).

The fit performed for non-stoitiometric Si_3N_4 is shown in Fig. 7.5; from the fit we find a small and negative value of α and β, however a perfect fit can be obtained by introducing a third cubic term χV^3 in the polynomial. We attribute such behaviour to the possible presence of ionic or vacancy movements in the capacitor, which accumulates and depletes from the interface resulting in an increase or decrease in capacitance which are not taken into account in eqn.(7.2). A low stress Si_3N_4 membrane has a significant concentration of oxygen, which is introduced in the deposition process to make the surface flat (as highlighted in chapter 5), therefore it is possible that oxygen vacancies are influencing the capacitance leading to a non-linear behaviour [197]. We expect the bottom side of the membrane to have more oxygen vacancies due to its exposure to the chemical etching process (using KOH), which could be the possible reason for the asymmetric behaviour, for example at ± 5 V where an equal and opposite change in capacitance was not observed. An important observation here is that at higher frequencies, the capacitance behave as a perfect ideal capacitor with no change in the capacitance with electric field.

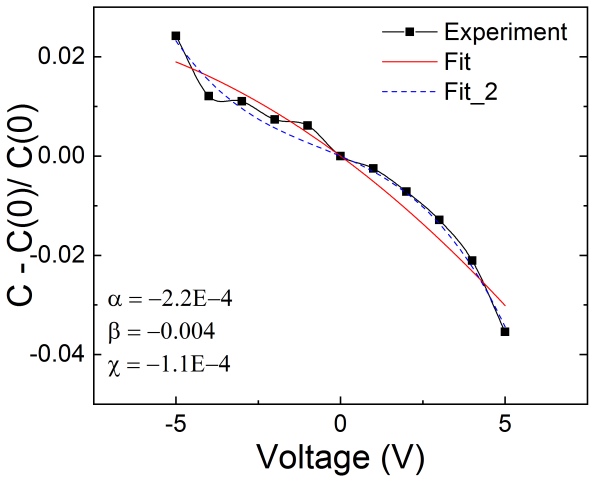

Figure 7.5: Normalized capacitanve vs V at 10 kHz of non-stoichiometric Si_3N_4 and fits to the data indicated by red and blue dotted lines. The fit shown in red line include first (β) and second (α) order coefficients and the blue line is fitted with first (β), second (α) and third (χ) order coefficients.

7.6 Characterizing charge traps

In the previous two sections, we understood how a capacitance can change at high frequency. However, in chapter 5, we observe that the charge accumulation is occurring in a single direction causing a non-reversible change in the interfacing magnetization. Therefore, as a next measurement, we verify the capacitance variation with the voltage cycles. Figure 7.6 shows the results of the capacitance measurements for stoichiometric and non-stoichiometric silicon nitride membrane with the applied voltage sequence, shown as blue squares. For non-stoichiometric silicon nitride membranes at 1 kHz we find a non-systematic behaviour in the capacitance with applied voltage. At 7 kHz, we observe a systematic of capacitance with voltage cycle. Besides this, we also observe that the capacitance is reducing at all the points measured at 0 V marked in red arrows (a change of 20 pF) and does not appear to increase after 20 voltage cycles, which is in agreement with the continuous decrease in the coercivity in Si_3N_4 gated Pt/Co/Pt with applied voltage cycles which is attributed to the continuous accumulation of charges

at the interface (shown in Fig. 5.5); at lower frequency, with the possibility of oxygen vacancy mobility, we can expect large changes in the capacitance. At 1 MHz we see no change in the capacitance with the applied voltage, which indicates no mobility in vacancies and at the same time the absence of the capacitance variation with voltage.

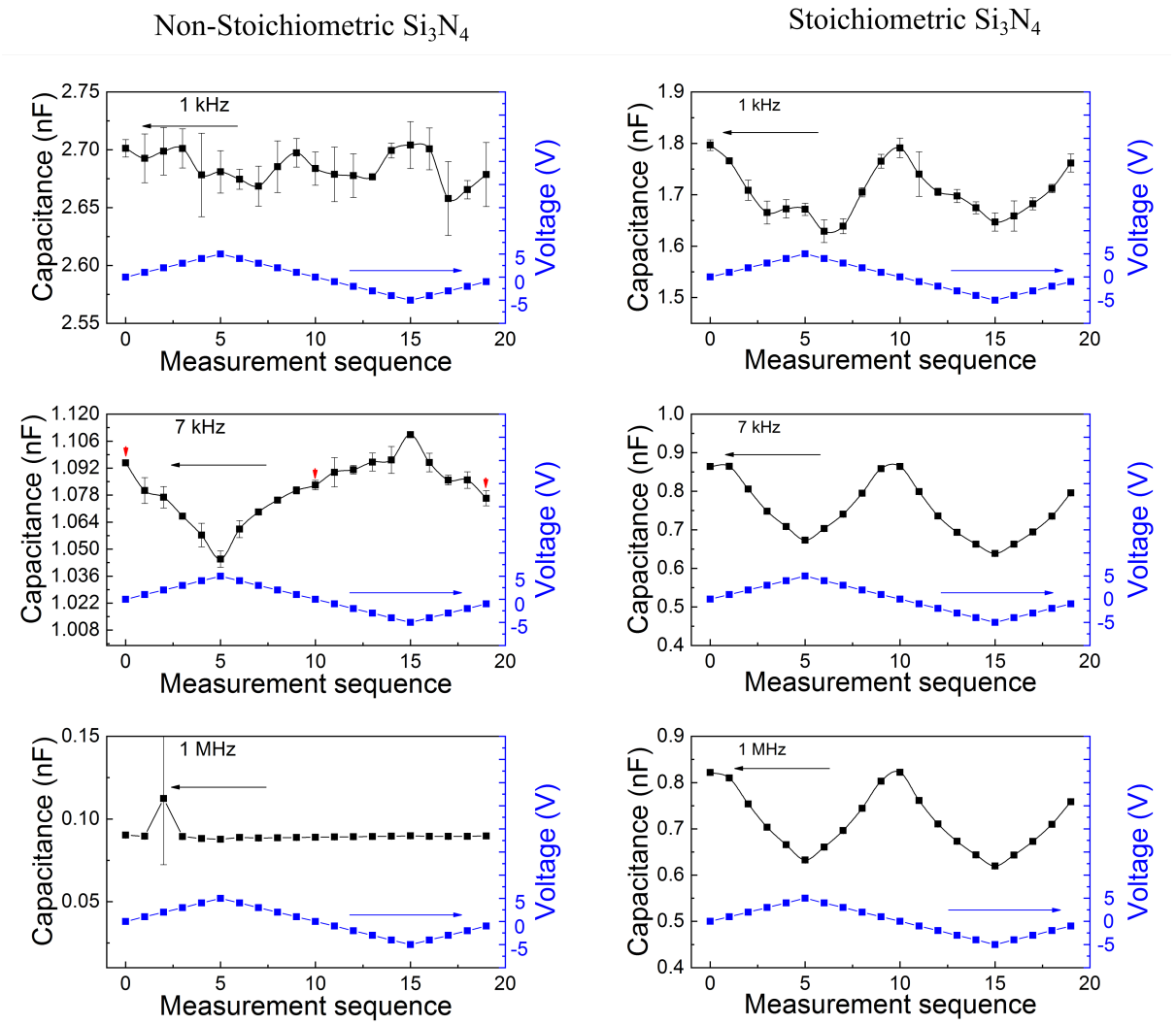

Figure 7.6: C vs V for different voltage cycle and frequencies for stoichiometric and non-stoichiometric membranes.

For stoichiometric silicon nitride membranes, we observe a consistent behaviour of the change in capacitance with applied electric field from 1 kHz to 1 MHz (Fig. 7.6). We also find a change in capacitance of about 10 pF from the initial and final applied voltage at 7 kHz and even at 1 MHz. We attribute this effect to the presence of electron charge traps, which are well known to occur in Si_3N_4. In summary, we find that the capacitance

decreases with voltage cycling, in both stoichiometric and non-stoichiometric membranes; for the stoichiometric membrane we attribute this effect to the electron charge traps as we can observe this effect even at higher frequencies, while for the non-stoichiometric membrane we attribute it to the impurities and oxygen vacancies.

7.7 Capacitance characterization using vector network analyzer

To characterize the capacitance at frequencies higher than 1 MHz, we employed a VNA. Figure 7.7 show the C-f characterization measured using the VNA. From the plot we find that the capacitance values are higher than what was measured with the LCR meter at 1 MHz, which we attribute to mis-calibration, and/or presence of bonding wires connecting the holder and the sample which is also contributing to the overall impedance measured with the VNA. In LCR measurements, we find that the capacitance is saturating already at frequency in the order of kHz, however, in VNA measurements we observe the capacitance to reduce even after 1 MHz. Therefore, it is possible that the inductive impedance (X_L) is interfering with the measured impedance (Z) at higher frequencies. New sample holders and a better calibration kit is required to obtain a more reliable characterization.

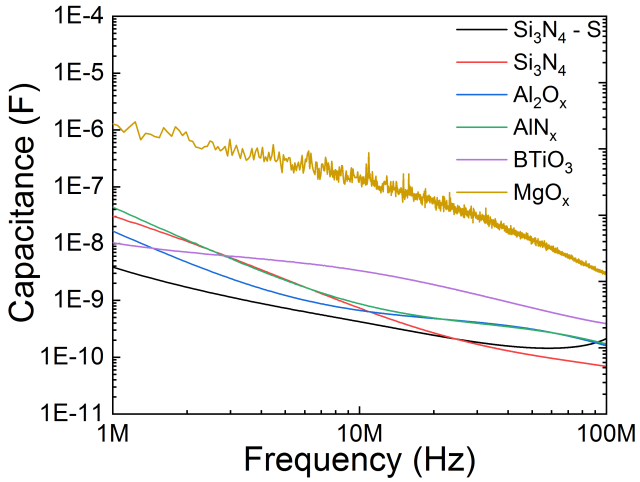

Figure 7.7: C vs Hz for different dielectrics using VNA.

In summary, we have analysed the C-f and C-V characteristics of six different dielectrics and we find that interfacial states are present in all of them. The presence of interfacial states in stoichiometric dielectrics may be due to the possible surface contamination, however for non-stoichiometric dielectrics we attribute the formation of interfacial states to intrinsic charge defects as well as surface contaminants. The second issue that may arise at high frequency, is the capacitance dependence on applied voltage, such that a dielectric even if it is stoichiometric can have a varying capacitance with the applied voltage. For stoichiometric silicon nitride membrane we find a change of about 200 pF with 5 V. Therefore, the C-V characteristics need to be measured to verify the suitability of the dielectric for high frequency voltage dependent applications. Finally, from voltage cycle measurements, we find the capacitance to decrease with voltage cycles; for stoichiometric silicon nitride membranes we attribute this effect to the presence of electron charge traps, while for non-stoichiometric membrane this effect may arise from a combination of vacancies and charge traps. Our results highlight the importance of high frequency characterization of dielectric for use in magnetoelectric coupling devices.

Chapter 8

Summary and Outlook

For many years, the presence of a magnetoelectric coupling in different artificial multiferroics have been demonstrated, however, only recently has their high frequency characterization been given importance. Until now most of the high frequency characterization was still performed in systems containing ferroelectric or pizoelectric substrates which have low time response, and high frequency characterization of magnetoelectric couplings on small size devices has still not been realized. Such small structures can become a good starting point to make devices for applications. Artificial multiferroics can be a suitable alternative for many applications in storage devices or sensor devices, however, there are many challenges that need to be overcome to make these viable systems to work at fast time scales similar to other silicon based electronics. In this thesis, we have found methods to fabricate multiferroic devices which can be used to test the high frequency characteristics. However, we conclude that the magnetoelectric coupling is hindered in the systems investigated by the presence of many material related defects, especially arising from the ferroelectric and dielectric components.

In chapter 4, we fabricated Ni/Co on $BaTiO_3$ heterostructures to form a strain-mediated coupling devices with a short capacitive rise time and suitable connectivity. Despite the presence of magnetoelectric coupling, a systematic control of magnetization was not possible due to the large surface roughness from the $BaTiO_3$. After many trials of adjusting the growth parameters, we achieved a better surface roughness on $BaTiO_3$ films grown on $SrTiO_3$. We expect to have a better magnetoelectric coupling in the optimized $BaTiO_3$ film with better high frequency performance. We also proposed alternative

systems to investigate high frequency characterization using piezoelectric/ferromagnetic and MEMS type devices.

Similarly, in chapter 5, we fabricated a charge-mediated coupling device using a commercially available silicon nitride membrane and Pt/Co/Pt heterostructures. Silicon nitride can be scaled down and small size magnetoelectric coupling devices can be made. We demonstrate the presence of a magnetoelectric coupling which is manifested in the form of electric field dependent domain wall fluctuations and domain wall nucleation. In addition we find the presence of OOP spin structure with dominant IP surrounding, as described in chapter 6. The formation of such spin structures is attributed to the presence of DMI and the stabilization of such spin structure is ascribed to the large surface roughness. A Ta/Co/Pt heterostructure with a net DMI has more density and relatively more stable OOP spin structures in a dominant IP surrounding than Pt/Co/Pt. We were also able to control the OOP spin structures by modulating the interfacial anisotropy in turn changing the overall anisotropy of the system. The low stress silicon nitride have a large concentration of oxygen, which is introduced during the deposition process to reduce the stress. As silicon nitride is known to have a large density of charge traps, and are enhanced with the presence of possible oxygen ion vacancies, which we identified from the capacitance vs frequency measurements. The presence of charge traps could still lead to a magnetoelectric coupling, however the changes in the magnetization was unidirectional and could not be reversed.

Since the lack of chemical stoichiometry can result in a large concentration of charge traps, in chapter 7, we characterized different dielectrics which have a potential to be used in multiferroic devices. Many multiferroic devices with identical dielectrics have shown the presence of magnetoelectric couplings, however, the origin of the charge modulation, whether it is from carrier charges, or vacancies or ions are not differentiated. Our result suggest that all the dielectrics studied here (Al_3O_x, AlN, MgO_x, $BaTiO_3$, Si_3N_4) have a significant amount of surface oxides and interfacial states which respond at low frequencies but not at high frequency. Therefore, besides the requirement for a stoichiometric dielectric, it is important that the surface of the dielectric is cleaned before metal deposition. For non-stoichiometric dielectrics, we find that the presence of both defects and vacancies affect the electrical properties. Although the stoichiometric silicon nitride show

less charge defects, we find that the dielectric can change with the applied voltage due to voltage dependent capacitance coefficient.

In conclusion, we have fabricated samples for strain- and charge-mediated magnetoelectric coupling suitable for high frequency characterization. We were unable to perform high frequency magnetoelectric dynamical characterization due to issues related to the ferroelectric and dielectric components. As the next step, more focus should be given to the sample deposition and fabrication process. The dielectric deposited should be chemically stoichiometric and at the same time with good electrical properties at high frequency. The presence of surface oxides or interfacial states can be reduced if the dielectric and the ferromagnetic material is grown in a single step without the sample being taken out to ambient atmosphere, or cleaned *in situ* by a plasma before depositing the ferromagnetic layers. We expect the stoichiometric Si_3N_4 to produce reproducible changes in the magnetization and be suitable for time resolved characterization. For strain mediated coupling, especially when using ferroelectrics, surface roughness has to be characterized, which should also be followed by electrical characterization. In addition, piezoforce microscopy characterization can be essential to check the ferroelectric nature of the film. New designs and sample fabrication methods should be considered for a large and effective strain-mediated coupling. A full dielectric/ferroelectric characterization need to be carried out before it can be considered for magnetoelectric coupling devices. With well characterized dielectrics and ferroelectrics, high frequency characterization of magnetoelectric coupling is not far from reach.

Acknowledgements

This project is never possible without the contribution from many people from PSI for their support with the experiment as well as scientific inputs, therefore it is important that each one is properly acknowledged and I thank each and everyone of you.

Family

I thank my parents, my sister, brother-in-law and my nephew for constant support.

Main Supervisors

Dr. Carlos A. F. Vaz and Prof. Frithjof Nolting, thank you very much for teaching me, mentoring me and helping me throughout in all aspects during the last four years.

Colleagues from Microscopy and Magnetism group

Colleagues from SIM beamline

Dr. Armin Kleibert : For teaching me how to use PEEM, letting me participate in Nanoparticle project and other cool projects at the beamline, helping with the bureaucracy in PSI.

Dr. Ludovic Howald : For his support and teaching with femto second laser and beamtime support during the first year.

Mrs. Tanya Savchenko: For her support in the beamtime for multiferroic project, nanoparticle project, SEM.

Mr. David Bracher: For his active support with most of the beamtime, and his scientific inputs.

Mr. Pascal Schifferle: For all the technical support from soldering to teaching me how to handle vacuum systems.

Colleagues from X-Treme beamline

Dr. Shridhar Avula Vekata Reddy: For his support in the beamtime, and letting me participate with his beamtime at X-Treme and all personal help.
Dr. Jan Dreiser : For being my Gotti, helping me get an office in SLS, when I was walking with crutches and my office is at the about 500 m, offering me the X-Treme beamtimes during the last stages of my thesis which was helpful.
Dr. Cinthia Piamonteze: For her initial teaching on XMCD, during the beamtime, letting me part of her projects.
Mr. Stefan Zeugan : for his help with sample holder preparation.

Other colleagues from Microscopy and magnetism group

Dr. Urs Staub, Dr. Michelle Buzzi, Ms. Nazaret Ortiz, Mr. Martin Decker, Dr. Sergii Parchenko and the rest of the people from the past.
Prof. Phil Willmott: For accepting me as a teaching assistant for online EdX course and also teaching me about synchrotron, latex.
Dr. Simone Finizio: For scientific inputs and lots of useful suggestions.

Colleagues who helped me with sample preparation and measurements

Mr. Michael Horisberger : Thank you very much for growing all the samples and also letting me use your machine, with out you all projects will be a disaster.
Dr. Nicolas S. Bingham : For his help is growing the $BaTiO_3$ sample, and teaching me PLD and giving me access to the labs.
Dr. Laura Maurel Velazquez : For her help is growing the $BaTiO_3$ sample during the last

few months.
Dr. Euginie Kirk : For her timely help to let me use the sputtering system when Michaels machine was broken.
Dr. Milan Radovic : For his help is growing $BaTiO_3$ films. I will fabricate your sample and one day we will have some results from it.
Dr. Marcos Gaspar : For his help with VNA measurement, teaching me HF measurements and making the calibration kits.

Laboratory for Multiscale Materials Experiments

Prof. Dr. Laura J. Heyderman : Thank you very much for letting me use all your instruments, which was indispensable in the projects.
Dr. Oles Sendisenki and Dr. Valerio Scagnoli : For teaching me how to use nano-MOKE and your support with the measurements.
Dr. Ana Suzka : For helping me with the sputtering machine and support in the lab.
Dr. Susmita Saha : For her help with SQUID and her scientific inputs especially in MOKE.
Mr. Hanu Arava : Letting me be part of his project, scientific talks, helping with AFM.
Others: Dr. Claire Donelly, Ms. Namrata Gurung, Mr. Kein Hofhouis, Dr. Naemi leo, Dr. Ales Hrabec, Dr. Jizai cui, Dr. Zhaochu Luo.

Laboratory of Micro and nanotechnology

Having spent most of my time at the clean room I met the most amazing people, had great conversations and huge support from everyone in every problem I had both scientific and personal.
Dr. Vitaliy Guzenko : He is like my second supervisor and Goti!! Thank you for teaching me about E-beam and lot of other things, especially our conversation after 5 pm before we left as the last people from the cleanroom.

Dr. Martin Bednarzik and Mr. Dario Marty : For teaching me one how to behave in the cleanroom and lot of other instruments and chemicals.
Others: Mr. Konrad, Mr. Eugen Deckardt, Mr. Thomas Neiger, Mr. Chistofer Wild, Mr. Rolf Schelldorfer, Ms. Jana Lehman, Mr. Stefan Stutz, Dr. Rajeev Ramachandran, Dr. Dimitrios Kazazis.

Office mates

Had a chance to share the office with people from seven different nationalities in a span of 4 years: Christoforos Moutafis (Greek), Nan Zu (Chinese), Simone Finizio (Italian), Luiz (Brazilian), Daria (Russian), Katharina Witte (German), Nicolas (French).

Others from PSI

PhD and postdoc association, Guesthouse people, late night bus members.

Curriculum Vitae

Personal Information

Name: Jaianth Vijayakumar

Date of birth: 24.09.1991

Nationality: Indian

Education

- Paul Scherrer Institut/ University of Basel, Switzerland:
  PhD Experimental Physics, Apr. 2015 – Mar. 2019
- Aalto University, Finland:
  M.Sc. Engineering Physics, Sept. 2012 – Mar. 2015
- University of Madras, India:
  B.Sc. Physics, Jun. 2009 – Aug. 2012

List of publications

1. Qi Hang, Laura Äkäslompolo, Noora Tuomisto, Lide Yao, Sayani Majumdar, **Jaianth Vijayakumar**, Arianna Casiraghi, et al. "Resistive Switching in All-Oxide Ferroelectric Tunnel Junctions with Ionic Interfaces." *Advanced Materials*, 6852–59 (2016).
2. Arava, Hanu, Peter M. Derlet, **Jaianth Vijayakumar**, Jizhai Cui, Nicholas S. Bingham, Armin Kleibert, and Laura J. Heyderman. "Computational Logic with

Square Rings of Nanomagnets." *Nanotechnology*, 29 (26) (2018).

3. Avula, S. R. V., J. Heidler, J. Dreiser, **J. Vijayakumar**, L. Howald, F. Nolting, and C. Piamonteze. "Study of Magneto-Electric Coupling between Ultra-Thin Fe Films and PMN-PT Using X-Ray Magnetic Circular Dichroism." *Journal of Applied Physics*, 123 (6) (2018)

4. J. Mendil, M. Trassin, Q. Bu, J. Schaab, M. Baumgartner, C. Murer, P. T. Dao, **J. Vijayakumar**, C. Bouillet, C. A. F. Vaz, M. Fiebig, and P. Gambardella, "Magnetic properties and domain structure of ultrathin Yttrium iron garnet/Pt bilayers." *Physical Review Materials*, 3, 034403 (2019)

5. **Jaianth Vijayakumar**, David bracher, Tatiana M. Savchenko, Michael Horisberger, Frithjof Nolting, C.A.F. Vaz, "Electric field control of magnetism in Si_3N_4 gated Pt/Co/Pt heterostructures." *Journal of Applied physics*, 125, 114101 (2019)

6. Zhaochu Luo, Trong Phuong Dao, Aleš Hrabec, **Jaianth Vijayakumar**, Armin Kleibert, Manuel Baumgartner, Eugenie Kirk, Jizhai Cui, Tatiana Savchenko, Gunasheel Krishnaswamy, Laura J. Heyderman, Pietro Gambardella, "Chirally Coupled Nanomagnets." *Science*, 363, 6434, pp. 1435-1439 (2019)

7. H. Arava, N.R. Leo, D. Schildknecht, J.Cui, **J.Vijayakumar**, P.M. Derlet, A. Kleibert, L.J. Heyderman, "Engineering Relaxation Pathways in Building Blocks of Artificial Spin Ice for Computation", (2019) (Submitted)

8. **Jaianth Vijayakumar**, Tatiana M. Savchenko, Armand Béché, Johan Verbeeck, Frithjof Nolting, C.A.F. Vaz, Armin Kleibert, "Morphology and magnetic characterization of Co nanoparticles under controlled oxidation using XPEEM and HR-TEM." (2019) (In preparation)

9. **Jaianth Vijayakumar**, Yu Li, David Bracher, Craig Burton, Michael Horisberger, Christoforos Moutafis, Frithjof Nolting, and C.A.F. Vaz, "Roughness induced out-of-plane spin structures in in-plane anisotropy magnetic thin films." (2019) (In preparation)

10. **Jaianth Vijayakumar**, Nicolas Bingham, Stefan Muff, Laura Murel, Ludovic Howald, Shridhar Avula Venkata Reddy, Milan Radovic, Laura J Haydermann, Frithjof Nolting, Carlos A. F. Vaz, "Strain mediated magnetoelectric coupling in $BaTiO_3$ (110)/Co heterostructures" (2019) (In preparation)

11. **Jaianth Vijayakumar**, Marcos Gaspar, Michael Horisberger, Frithjof Nolting, and C.A.F. Vaz, "High Frequency and electric field characterization of thin film capacitors." (2019) (In preparation)

12. Tatiana M. Savchenko, Michele Buzzi, **Jaianth Vijayakumar**, Martin Timm, Ludovic Howald, David Bracher, Carlos A. F. Vaz, Frithjof Nolting, and Armin Kleibert, "Effect of ultrashort laser pulse on the magnetic and chemical state of individual Co nanoparticles probed by X-PEEM." (2019) (In preparation)

Bibliography

[1] Melvin M. Vopson. Fundamentals of multiferroic materials and their possible applications. *Critical Reviews in Solid State and Materials Sciences*, 40(4):223–250, 2015.

[2] Shuxiang Dong, J. F. Li, D. Viehland, J. Cheng, and L. E. Cross. A strong magnetoelectric voltage gain effect in magnetostrictive- piezoelectric composite. *Applied Physics Letters*, 85(16):3534–3536, 2004.

[3] Yao Wang, Jiamian Hu, Yuanhua Lin, and Ce Wen Nan. Multiferroic magnetoelectric composite nanostructures. *NPG Asia Materials*, 2(2):61–68, 2010.

[4] G. Lawes and G. Srinivasan. Introduction to magnetoelectric coupling and multiferroic films. *Journal of Physics D: Applied Physics*, 44(24), 2011.

[5] G. Srinivasan. Magnetoelectric Composites. *Annual Review of Materials Research*, 40(1):153–178, 2010.

[6] Ce Wen Nan, M. I. Bichurin, Shuxiang Dong, D. Viehland, and G. Srinivasan. Multiferroic magnetoelectric composites: Historical perspective, status, and future directions. *Journal of Applied Physics*, 103(3), 2008.

[7] Fenglong Wang, Cai Zhou, Chao Zhang, Chunhui Dong, Chengcheng Yang, Changjun Jiang, Chenglong Jia, and Desheng Xue. Piezoelectric control of magnetic dynamics in Co/Pb($Mg_{1/3}$ Nb $_{2/3}$ O_3-$PbTiO_3$) heterostructure. *Applied Physics Letters*, 105(6), 2014.

[8] Y. K. Fetisov and G. Srinivasan. Electrically tunable ferrite-ferroelectric microwave delay lines. *Applied Physics Letters*, 87(10):1–4, 2005.

[9] Alexey B. Ustinov and G. Srinivasan. Subterahertz excitations and magnetoelectric effects in hexaferrite-piezoelectric bilayers. *Applied Physics Letters*, 93(14), 2008.

[10] Martin Gajek, Manuel Bibes, Stéphane Fusil, Karim Bouzehouane, Josep Fontcuberta, Agnès Barthélémy, and Albert Fert. Tunnel junctions with multiferroic barriers. *Nature Materials*, 6(4):296–302, 2007.

[11] Manuel Bibes. Towards a Magnetoelectric memory. *Nature Materials*, 7:1–2, 2008.

[12] Ashok Kumar, Ram S. Katiyar, and James F. Scott. Novel room temperature multiferroics for random access memory elements. *IEEE Transactions on Ultrasonics, Ferroelectrics, and Frequency Control*, 57(10):2237–2242, 2010.

[13] R. Nechache, C. Harnagea, S. Licoccia, E. Traversa, A. Ruediger, A. Pignolet, and F. Rosei. Photovoltaic properties of Bi_2FeCrO_6 epitaxial thin films. *Applied Physics Letters*, 98(20):2009–2012, 2011.

[14] Martin A. Green, S. R. Wenham, and A. W. Blakers. Recent Advances in High Efficiency Silicon Solar Cells. *Conference Record of the IEEE Photovoltaic Specialists Conference*, 024103(2012):6–12, 1987.

[15] Lei Wang and F. G. Yuan. Vibration energy harvesting by magnetostrictive material. *Smart Materials and Structures*, 17(4), 2008.

[16] Mauro Zucca, Oriano Bottauscio, Cinzia Beatrice, and Fausto Fiorillo. Modeling amorphous ribbons in energy harvesting applications. *IEEE Transactions on Magnetics*, 47(10):4421–4424, 2011.

[17] Thomas Lafont, L. Gimeno, J. Delamare, G. A. Lebedev, D. I. Zakharov, B. Viala, O. Cugat, N. Galopin, L. Garbuio, and O. Geoffroy. Magnetostrictive-piezoelectric composite structures for energy harvesting. *Journal of Micromechanics and Microengineering*, 22(9), 2012.

[18] R. Wood. The feasibility of magnetic recording at 1 terabit per square inch. *IEEE Transactions on Magnetics*, 36(1):36–42, 2000.

[19] E. Grochowski and D. A. Thompson. Outlook for maintaining areal density growth in magnetic recording. *IEEE Transactions on Magnetics*, 30(6):3797–3800, 1994.

[20] M. Mallary, A. Torabi, and M. Benakli. One terabit per square inch perpendicular recording conceptual design. *IEEE Transactions on Magnetics*, 38(4):1719–1724, 2002.

[21] Sining Mao et al. Commercial tmr heads for hard disk drives: characterization and extendibility at 300 gbit2. *IEEE Transactions on Magnetics*, 42(2):97–102, 2006.

[22] S. Tehrani, J. M. Slaughter, E. Chen, M. Durlam, J. Shi, and M. Deherrera. Progress and outlook for mram technology. *IEEE Transactions on Magnetics*, 35(5):2814–2819, 1999.

[23] Titiksha Srivastava, Marine Schott, Roméo Juge, Viola Křižáková, Mohamed Belmeguenai, Yves Roussigné, Anne Bernand-Mantel, Laurent Ranno, Stefania Pizzini, Salim-Mourad Chérif, Andrey Stashkevich, Stéphane Auffret, Olivier Boulle, Gilles Gaudin, Mairbek Chshiev, Claire Baraduc, and Hélène Béa. Large-voltage tuning of dzyaloshinskii–moriya interactions: A route toward dynamic control of skyrmion chirality. *Nano Letters*, 18(8):4871–4877, 2018.

[24] Marine Schott, Anne Bernand-Mantel, Laurent Ranno, Stefania Pizzini, Jan Vogel, Hélène Béa, Claire Baraduc, Stéphane Auffret, Gilles Gaudin, and Dominique Givord. The skyrmion switch: Turning magnetic skyrmion bubbles on and off with an electric field. *Nano Letters*, 17(5):3006–3012, 2017.

[25] Zidong Wang, Zhao Ma, and Malcolm J. Grimson. Magnetoelectric coupling and the manipulation of magnetic bloch skyrmions. *Applied Physics Letters*, 113(10):102403, 2018.

[26] W. Zhang, H. Zhong, R. Zang, Y. Zhang, S. Yu, G. Han, G. L. Liu, S. S. Yan, S. Kang, and L. M. Mei. Electrical field enhanced interfacial Dzyaloshinskii-Moriya interaction in MgO/Fe/Pt system. *Applied Physics Letters*, 113(12):122406, 2018.

[27] C.A.F. Vaz and Urs Staub. Artificial multiferroic heterostructures. *J. Mater. Chem. C*, 1:6731–6742, 2013.

[28] Ondřej Vlašín, Romain Jarrier, Rémi Arras, Lionel Calmels, Bénédicte Warot-Fonrose, Cécile Marcelot, Matthieu Jamet, Philippe Ohresser, Fabrice Scheurer, Riccardo Hertel, Gervasi Herranz, and Salia Cherifi-Hertel. Interface Magnetoelectric Coupling in Co/Pb(Zr,Ti)O3. *ACS Applied Materials and Interfaces*, 8(11):7553–7563, 2016.

[29] Scott Newacheck, Taylor Webster, and George Youssef. The effect of multidirectional bias magnetic fields on the converse magnetoelectric response of multiferroic concentric composite ring. *Applied Physics Letters*, 113(17):172902, 2018.

[30] Michael Foerster, Ferran Macià, Nahuel Statuto, Simone Finizio, Alberto Hernández-Mínguez, Sergi Lendínez, Paulo V. Santos, Josep Fontcuberta, Joan Manel Hernàndez, Mathias Kläui, and Lucia Aballe. Direct imaging of delayed magneto-dynamic modes induced by surface acoustic waves. *Nature Communications*, 8(1):1–6, 2017.

[31] William H. Shepherd. Electrical Characteristics of Ferroelectric PZT Thin Films for DRAM Applications. *IEEE Transactions on Electron Devices*, 39(9):2044–2049, 1992.

[32] G. W. Dietz, M. Schumacher, R. Waser, S. K. Streiffer, C. Basceri, and A. I. Kingon. Leakage currents in $Ba_{0.7}Sr_{0.3}TiO_3$ thin films for ultrahigh-density dynamic random access memories. *Journal of Applied Physics*, 82(5):2359–2364, 1997.

[33] M. Dawber, K. M. Rabe, and J. F. Scott. Physics of thin-film ferroelectric oxides. *Rev. Mod. Phys.*, 77:1083–1130, 2005.

[34] J. F. Scott. High-dielectric constant thin films for dynamic random access memories (dram). *Annual Review of Materials Science*, 28(1):79–100, 1998.

[35] B Lengeler, H Lüth, W Mönch, and J Pollmann. *Formation of Semiconductor Interfaces*. WORLD SCIENTIFIC, 1994.

[36] David E. Kotecki. A review of high dielectric materials for dram capacitors. *Integrated Ferroelectrics*, 16(1-4):1–19, 1997.

[37] C.A.F. Vaz, Y. Segal, J. Hoffman, F. J. Walker, and C. H. Ahn. Growth and characterization of PZT/LSMO multiferroic heterostructures. *Journal of Vacuum Science & Technology B, Nanotechnology and Microelectronics: Materials, Processing, Measurement, and Phenomena*, 28(4), 2010.

[38] C.A.F. Vaz, F. J. Walker, C. H. Ahn, and S. Ismail-Beigi. Intrinsic interfacial phenomena in manganite heterostructures. *Journal of Physics Condensed Matter*, 27(12), 2015.

[39] Javier Junquera and Philippe Ghosez. Critical thickness for ferroelectricity in perovskite ultrathin films. *Nature*, 422(6931):506–509, 2003.

[40] Qi Hang Qin, Laura Äkäslompolo, Noora Tuomisto, Lide Yao, Sayani Majumdar, Jaianth Vijayakumar, Arianna Casiraghi, Sampo Inkinen, Binbin Chen, Asier Zugarramurdi, Martti Puska, and Sebastiaan van Dijken. Resistive Switching in All-Oxide Ferroelectric Tunnel Junctions with Ionic Interfaces. *Advanced Materials*, 28:6852–6859, 2016.

[41] J.-E Wegrowe, D Kelly, Y Jaccard, Ph Guittienne, and J.-Ph Ansermet. Current-induced magnetization reversal in magnetic nanowires. *Europhysics Letters (EPL)*, 45(5):626–632, 1999.

[42] E. B. Myers, D. C. Ralph, J. A. Katine, R. N. Louie, and R. A. Buhrman. Current-induced switching of domains in magnetic multilayer devices. *Science*, 285(5429):867–870, 1999.

[43] D.C. Ralph and M.D. Stiles. Spin transfer torques. *Journal of Magnetism and Magnetic Materials*, 320(7):1190 – 1216, 2008.

[44] Jonathan Ehrler, Miao He, Maxim V. Shugaev, Nikolay I. Polushkin, Sebastian Wintz, Vico Liersch, Steffen Cornelius, René Hübner, Kay Potzger, Jürgen Lindner, Jürgen Fassbender, Ahmet A. Ünal, Sergio Valencia, Florian Kronast, Leonid V. Zhigilei, and Rantej Bali. Laser-rewriteable ferromagnetism at thin-film surfaces. *ACS Applied Materials & Interfaces*, 10(17):15232–15239, 2018.

[45] O. Sandig, Y. A. Shokr, J. Vogel, S. Valencia, F. Kronast, and W. Kuch. Movement of magnetic domain walls induced by single femtosecond laser pulses. *Phys. Rev. B*, 94:054414, 2016.

[46] Ashima Arora, Mohamad-Assaad Mawass, Oliver Sandig, Chen Luo, Ahmet A. Ünal, Florin Radu, Sergio Valencia, Florian Kronast. Spatially resolved investigation of all optical magnetization switching in TbFe alloys. *Scientific Reports*, 7:9456, 2017.

[47] C.A.F. Vaz. Electric field control of magnetism in multiferroic heterostructures. *Journal of Physics Condensed Matter*, 24(33):333201, 2012.

[48] Manfred Fiebig. Revival of the magnetoelectric effect. *Journal of Physics D: Applied Physics*, 38(8):R123–R152, 2005.

[49] Shuai Dong, Jun Ming Liu, Sang Wook Cheong, and Zhifeng Ren. Multiferroic materials and magnetoelectric physics: Symmetry, entanglement, excitation, and topology. *Advances in Physics*, 64(5-6):519–626, 2015.

[50] G. T. Rado and V. J. Folen. Magnetoelectric effects in antiferromagnetics. *Journal of Applied Physics*, 33(3):1126–1132, 1962.

[51] L. D. Landau and E. M.Lifshitz. *Electrodynamics of Continuous Media*. PERGAMON PRESS, Oxford, Londaon, New York, Paris, 1960.

[52] A. N. Kalinkin and V. M. Skorikov. BiFeO3 films and single crystals as a promising inorganic material for spintronics. *Russian Journal of Inorganic Chemistry*, 55(11):1794–1809, 2010.

[53] M. B. Holcomb, S. Polisetty, A. Fraile Rorígquez, V. Gopalan, and R. Ramesh. Investigating Electric Field Control of Magnetism With Neutron Scattering, Nonlinear Optics and Synchrotron X-Ray Spectromicroscopy. *International Journal of Modern Physics B*, 26(10):1230004, 2012.

[54] Josep Fontcuberta. Multiferroic $RMnO_3$ thin films. *Comptes Rendus Physique*, 16(2):204–226, 2015.

[55] D. Sando, Bin Xu, L. Bellaiche, and V. Nagarajan. A multiferroic on the brink: Uncovering the nuances of strain-induced transitions in $BiFeO_3$. *Applied Physics Reviews*, 3(1):011106, 2016.

[56] R. Ramesh and Nicola A. Spaldin. Multiferroics: Progress and prospects in thin films. *Nature Materials*, 6(1):21–29, 2007.

[57] Sebastiaan van Dijken Tuomas H. E. Lahtinen, Kevin J. A. Franke. Electric-field control of magnetic domain wall motion and local magnetization reversal. *Scientific Reports*, 2:258:1–6, 2012.

[58] Sarbeswar Sahoo, Srinivas Polisetty, Chun-Gang Duan, Sitaram S. Jaswal, Evgeny Y. Tsymbal, and Christian Binek. Ferroelectric control of magnetism in $BaTio_3Fe$ heterostructures via interface strain coupling. *Phys. Rev. B*, 76:092108, 2007.

[59] M. Buzzi, R. V. Chopdekar, J. L. Hockel, A. Bur, T. Wu, N. Pilet, P. Warnicke, G. P. Carman, L. J. Heyderman, and F. Nolting. Single domain spin manipulation by electric fields in strain coupled artificial multiferroic nanostructures. *Phys. Rev. Lett.*, 111:027204, 2013.

[60] S. Narendra Babu, Seong-Gi Min, Amin Yourdkhani, Gabriel Caruntu, and Leszek Malkinski. Magnetoelectric effect in AlN/CoFe bi-layer thin film composites. *Journal of Applied Physics*, 111(7):07C720, 2012.

[61] Wen-Chin Lin, Po-Chun Chang, Cheng-Jui Tsai, Tsung-Chun Shieh, and Fang-Yuh Lo. Voltage-induced reversible changes in the magnetic coercivity of Fe/ZnO heterostructures. *Applied Physics Letters*, 104(6):062411, 2014.

[62] Robert C.O' Hangley. *Modern Magnetic Materials*. John Wiley and Sons, USA and Canada, 2000.

[63] M. Stengel J. M. Rondinelli and N. A. Spaldin. Carrier-mediated magnetoelectricity in complex oxide heterostructures. *Nature Nanotechnology*, 3(1):46–50, 2008.

[64] T. Maruyama, Y. Shiota, T. Nozaki, K. Ohta, N. Toda, M. Mizuguchi, A. A. Tulapurkar, T. Shinjo, M. Shiraishi, S. Mizukami, Y. Ando, and Y. Suzuki. Large voltage-induced magnetic anisotropy change in a few atomic layers of iron. *Nature Nanotechnology*, 4(3):158–161, 2009.

[65] H. Lu, T. A. George, Y. Wang, I. Ketsman, J. D. Burton, C.-W. Bark, S. Ryu, D. J. Kim, J. Wang, C. Binek, P. A. Dowben, A. Sokolov, C.-B. Eom, E. Y. Tsymbal, and A. Gruverman. Electric modulation of magnetization at the $BaTiO_3$ /$La_{0.67}Sr_{0.33}$/ MnO_3 interfaces. *Applied Physics Letters*, 100(23):232904, 2012.

[66] Philipp M. Leufke, Robert Kruk, Richard A. Brand, and Horst Hahn. In situ magnetometry studies of magnetoelectric LSMO/PZT heterostructures. *Physical Review B - Condensed Matter and Materials Physics*, 87(9):1–9, 2013.

[67] C. A. F. Vaz, J. Hoffman, Y. Segal, M. S. J. Marshall, J. W. Reiner, Z. Zhang, R. D. Grober, F. J. Walker, and C. H. Ahn. Control of magnetism in $Pb(Zr_{0.2}Ti_{0.8})O_3$ /$La_{0.8}Sr_{0.2}MnO_3$ multiferroic heterostructures (invited). *Journal of Applied Physics*, 109(7):07D905, 2011.

[68] Hajo J.A. Molegraaf, Jason Hoffman, Carlos A.F. Vaz, Stefano Gariglio, Dirk Van Der Morel, Charles H. Ahn, and Jean Marc Triscone. Magnetoelectric effects in complex oxides with competing ground states. *Advanced Materials*, 21(34):1–5, 2009.

[69] C.A.F. Vaz, Y. Segal, J. Hoffman, R.D. Grober, F.J. Walker, and C.H. Ahn. Temperature dependence of the magnetoelectric effect in $Pb(Zr_{0.2}Ti_{0.8})O_3/La_{0.8}Sr_{0.2}MnO_3$ multiferroic heterostructures. *Applied Physics Letters*, 97(4):130–132, 2010.

[70] X. Ma, A. Kumar, S. Dussan, H. Zhai, F. Fang, H. B. Zhao, J. F. Scott, R. S. Katiyar, and G. Lüpke. Charge control of antiferromagnetism at $PbZr_{0.52}Ti_{0.48}O_3/La_{0.67}Sr_{0.33}MnO_3$ interface. *Applied Physics Letters*, 104(13):0–4, 2014.

[71] S. R. V. Avula, J. Heidler, J. Dreiser, J. Vijayakumar, L. Howald, F. Nolting, and C. Piamonteze. Study of magneto-electric coupling between ultra-thin Fe films and PMN-PT using X-ray magnetic circular dichroism. *Journal of Applied Physics*, 123(6):064103, 2018.

[72] A. J. Schellekens, A. Van Den Brink, J. H. Franken, H. J.M. Swagten, and B. Koopmans. Electric-field control of domain wall motion in perpendicularly magnetized materials. *Nature Communications*, 3:845–847, 2012.

[73] Uwe Bauer, Satoru Emori, and Geoffrey S.D. Beach. Voltage-controlled domain wall traps in ferromagnetic nanowires. *Nature Nanotechnology*, 8(6):411–416, 2013.

[74] Uwe Bauer, Lide Yao, Aik Jun Tan, Parnika Agrawal, Satoru Emori, Harry L. Tuller, Sebastiaan Van Dijken, and Geoffrey S.D. Beach. Magneto-ionic control of interfacial magnetism. *Nature Materials*, 14(2):174–181, 2015.

[75] R.E. Newnham, D.P. Skinner and L.E. Cross. Connectivity and piezoelectric-pyroelectric composites. *Mat. Res. Bull.*, 13:525–536, 1978.

[76] Alex Hubert and Rudolf Schäfer. *Magnetic Domains*. Springer-Verlag Berlin Heidelberg, 1998.

[77] Gong Chen, Sang Pyo Kang, Colin Ophus, Alpha T. N'Diaye, Hee Young Kwon, Ryan T. Qiu, Changyeon Won, Kai Liu, Yizheng Wu, and Andreas K. Schmid. Out-of-plane chiral domain wall spin-structures in ultrathin in-plane magnets. *Nature Communications*, 8:1–7, 2017.

[78] C. Moreau-Luchaire, C. Moutafis, N. Reyren, J. Sampaio, C.A.F. Vaz, N. Van Horne, K. Bouzehouane, K. Garcia, C. Deranlot, P. Warnicke, P. Wohlhüter, J. M. George, M. Weigand, J. Raabe, V. Cros, and A. Fert. Additive interfacial chiral interaction in multilayers for stabilization of small individual skyrmions at room temperature. *Nature Nanotechnology*, 11(5):444–448, 2016.

[79] Frances Hellman, Axel Hoffmann, Yaroslav Tserkovnyak, Geoffrey S D Beach, Eric E Fullerton, Chris Leighton, Allan H MacDonald, Daniel C Ralph, Dario A

Arena, Hermann A Dürr, Peter Fischer, Julie Grollier, Joseph P Heremans, Tomas Jungwirth, Alexey V Kimel, Bert Koopmans, Ilya N Krivorotov, Steven J May, Amanda K Petford-Long, James M Rondinelli, Nitin Samarth, Ivan K Schuller, Andrei N Slavin, Mark D Stiles, Oleg Tchernyshyov, André Thiaville, and Barry L Zink. Interface-Induced Phenomena in Magnetism. *Reviews of modern physics*, 89(2):1–79, 2017.

[80] A.N. Bogdanov and D.A. Yablonskii. Thermodynamically stable "vortices" in magnetically ordered crystals. The mixed state of magnets. *Zh. Eksp. Teor. Fiz*, 95(1):178, 1989.

[81] A. Neubauer, C. Pfleiderer, B. Binz, A. Rosch, R. Ritz, P. G. Niklowitz, and P. Böni. Topological hall effect in the *a* phase of mnsi. *Phys. Rev. Lett.*, 102:186602, 2009.

[82] S. Mühlbauer, B. Binz, F. Jonietz, C. Pfleiderer, A. Rosch, A. Neubauer, R. Georgii, and P. Böni. Skyrmion lattice in a chiral magnet. *Science*, 323(5916):915–919, 2009.

[83] C. Pappas, E. Lelièvre-Berna, P. Falus, P. M. Bentley, E. Moskvin, S. Grigoriev, P. Fouquet, and B. Farago. Chiral paramagnetic skyrmion-like phase in mnsi. *Phys. Rev. Lett.*, 102:197202, 2009.

[84] Soshin Chikazumi. *Physics of Ferromagnetism*. Wiley, New York, 1997.

[85] I. Dzyaloshinsky. A thermodynamic theory of "weak" ferromagnetism of antiferromagnetics. *Journal of Physics and Chemistry of Solids*, 4(4):241–255, 1958.

[86] Tôru Moriya. Anisotropic superexchange interaction and weak ferromagnetism. *Phys. Rev.*, 120:91–98, 1960.

[87] Wanjun Jiang, Gong Chen, Kai Liu, Jiadong Zang, Suzanne G.E. te Velthuis, and Axel Hoffmann. Skyrmions in magnetic multilayers. *Physics Reports*, 704:1 – 49, 2017.

[88] Anjan Soumyanarayanan, M. Raju, A. L.Gonzalez Oyarce, Anthony K.C. Tan, Mi Young Im, A. P. Petrovic, Pin Ho, K. H. Khoo, M. Tran, C. K. Gan, F. Ernult, and C. Panagopoulos. Tunable room-temperature magnetic skyrmions in Ir/Fe/Co/Pt multilayers. *Nature Materials*, 16(9):898–904, 2017.

[89] J. Sampaio, V. Cros, S. Rohart, A. Thiaville, and A. Fert. Nucleation, stability and current-induced motion of isolated magnetic skyrmions in nanostructures. *Nature Nanotechnology*, 8(11):839–844, 2013.

[90] S. Rohart, J. Miltat, and A. Thiaville. Path to collapse for an isolated néel skyrmion. *Phys. Rev. B*, 93:214412, 2016.

[91] Hans-Benjamin Braun. Topological effects in nanomagnetism: from superparamagnetism to chiral quantum solitons. *Advances in Physics*, 61(1):1–116, 2012.

[92] Tokura Yoshinori Nagaosa, Naoto. Topological properties and dynamics of magnetic skyrmions. *Nature Nanotechnology*, 8(899), 2013.

[93] Wanjun Jiang, Xichao Zhang, Guoqiang Yu, Wei Zhang, Xiao Wang, M Benjamin Jungfleisch, John E Pearson, Xuemei Cheng, Olle Heinonen, Kang L Wang, Yan Zhou, Axel Ho, and Suzanne G E Velthuis. Direct observation of the skyrmion hall effect. *Nature Physics*, 13(162), 2016.

[94] Felix Büttner, C. Moutafis, M. Schneider, B. Krüger, C. M. Günther, J. Geilhufe, C. V.Korff Schmising, J. Mohanty, B. Pfau, S. Schaffert, A. Bisig, M. Foerster, T. Schulz, C. A.F. Vaz, J. H. Franken, H. J.M. Swagten, M. Kläui, and S. Eisebitt. Dynamics and inertia of skyrmionic spin structures. *Nature Physics*, 11(3):225–228, 2015.

[95] G. Chen, J. Zhu, A. Quesada, J. Li, A. T. N'Diaye, Y. Huo, T. P. Ma, Y. Chen, H. Y. Kwon, C. Won, Z. Q. Qiu, A. K. Schmid, and Y. Z. Wu. Novel chiral magnetic domain wall structure in Fe/Ni/Cu(001) films. *Phys. Rev. Lett.*, 110:177204, 2013.

[96] M. J. Benitez, A. Hrabec, A. P. Mihai, T. A. Moore, G. Burnell, D. Mcgrouther, C. H. Marrows, and S. McVitie. Magnetic microscopy and topological stability of homochiral Néel domain walls in a Pt/Co/AlO x trilayer. *Nature Communications*, 6:1–7, 2015.

[97] S. Meckler, N. Mikuszeit, A. Preßler, E. Y. Vedmedenko, O. Pietzsch, and R. Wiesendanger. Real-space observation of a right-rotating inhomogeneous cy-

cloidal spin spiral by spin-polarized scanning tunneling microscopy in a triple axes vector magnet. *Phys. Rev. Lett.*, 103:157201, 2009.

[98] Kasturi Lal Chopra and Inderjeet KaurJ. *Thin Film Device Applications*. Plenum Press, New York, 1983.

[99] Hamid R. Khan Hartmut Frey. *Handbook of Thin-Film Technology*. Springer-Verlag Berlin Heidelberg, 2015.

[100] Niculae N. Puscas Mihai Stafe, Aurelian Marcu. *Pulsed Laser Ablation of Solids, Basic, Theory and Applications*. Springer-Verlag Berlin Heidelberg, 2014.

[101] Mohammad Ali Mohammad, Mustafa Muhammad, Steven K. Dew, and Maria Stepanova. *Fundamentals of Electron Beam Exposure and Development*, pages 11–41. Springer Vienna, Vienna, 2012.

[102] István Mohácsi. *Double-sided fresnel zone plates as high performance optics in X-ray microscopy*. PhD thesis, University of Basel, 2015.

[103] Wolfgang Kuch, Rudolf Schafer, Peter Fischer, Franz Ulrich Hillebrecht. *Magnetic Microscopy of Layered Structures*. Springer-Heidelberg New York Dordrecht London, 2015.

[104] Thompson B. Visnovsky, S. *Optics in Magnetic Multilayers and Nanostructures*. Taylor Francis, Boca Raton, 2006.

[105] G. Traeger, L. Wenzel, and A. Hubert. Computer experiments on the information depth and the figure of merit in magnetooptics. *physica status solidi (a)*, 131(1):201–227, 1992.

[106] http://www.hindsinstruments.com/wp-content/uploads/magneto-optic-kerr-effect.pdf.

[107] P. Willmott. *An introduction to synchrotron radiation: Techniques and applications*. Jhon Wiley and Sons Ltd, UK, 2011.

[108] J.Stohr, H.C. Siegmann. *Magnetism: From Fundamentals to Nanoscale Dynamics*. Springer Berlin Heidelberg, 2006.

[109] Gerrit van der Laan, Bernard T. Thole, George A. Sawatzky, Jeroen B. Goedkoop, John C. Fuggle, Jean-Marc Esteva, Ramesh Karnatak, J. P. Remeika, and Hanna A. Dabkowska. Experimental proof of magnetic x-ray dichroism. *Phys. Rev. B*, 34:6529–6531, 1986.

[110] B. T. Thole, G. van der Laan, and G. A. Sawatzky. Strong magnetic dichroism predicted in the $M_{4,5}$ x-ray absorption spectra of magnetic rare-earth materials. *Phys. Rev. Lett.*, 55:2086–2088, 1985.

[111] Pieter Kuiper, Barry G. Searle, Petra Rudolf, L. H. Tjeng, and C. T. Chen. X-ray magnetic dichroism of antiferromagnet fe_2o_3: The orientation of magnetic moments observed by fe 2p x-ray absorption spectroscopy. *Phys. Rev. Lett.*, 70:1549–1552, 1993.

[112] C. Chen, Y. Idzerda, H.-J. Lin, N. Smith, G. Meigs, E. Chaban, G. Ho, E. Pellegrin, and F. Sette. Experimental Confirmation of the X-Ray Magnetic Circular Dichroism Sum Rules for Iron and Cobalt. *Phys. Rev. Lett.*, 75(1):152–155, 1995.

[113] E. Beaurepaire et al. *Magnetism and Synchrotron Radiation.* Springer - Verlag Berlin Heidelberg, 2010.

[114] Jakoba Kolumbine Heidler. *Ferroelectric control of magnetism in artificial multiferroic composites.* PhD thesis, University of Basel, 2015.

[115] Olivier Boulle, Jan Vogel, Hongxin Yang, Stefania Pizzini, Dayane De Souza Chaves, Andrea Locatelli, Tevfik Onur Menteş, Alessandro Sala, Liliana D. Buda-Prejbeanu, Olivier Klein, Mohamed Belmeguenai, Yves Roussigné, Andrey Stashkevich, Salim Mourad Chérif, Lucia Aballe, Michael Foerster, Mairbek Chshiev, Stéphane Auffret, Ioan Mihai Miron, and Gilles Gaudin. Room-temperature chiral magnetic skyrmions in ultrathin magnetic nanostructures. *Nature Nanotechnology*, 11(5):449–454, 2016.

[116] B. P. Tonner and G. R. Harp. Photoelectron microscopy with synchrotron radiation. *Review of Scientific Instruments*, 59(6):853–858, 1988.

[117] U. Flechsig, F. Nolting, A. Fraile Rodríguez, J. Krempaský, C. Quitmann, T. Schmidt, S. Spielmann, and D. Zimoch. Performance measurements at the sls sim beamline. *AIP Conference Proceedings*, 1234(1):319–322, 2010.

[118] Cinthia Piamonteze, Uwe Flechsig, Stefano Rusponi, Jan Dreiser, Jakoba Heidler, Marcus Schmidt, Reto Wetter, Marco Calvi, Thomas Schmidt, Helena Pruchova, Juraj Krempasky, Christoph Quitmann, Harald Brune, and Frithjof Nolting. X-Treme beamline at SLS: X-ray magnetic circular and linear dichroism at high field and low temperature. *Journal of Synchrotron Radiation*, 19(5):661–674, 2012.

[119] M. Buzzi, C. A. F. Vaz, J. Raabe, and F. Nolting. Electric field stimulation setup for photoemission electron microscopes. *Review of Scientific Instruments*, 86(8):083702, 2015.

[120] Savoini M. El Moussaoui S. Buzzi M. Tsukamoto A. Itoh A. Kirilyuk A. Rasing T. Kimel A. V. Nolting F. Le Guyader, L. Nanoscale sub-100 picosecond all-optical magnetization switching in gdfeco microstructures. *Nature Communications*, 6(5839), 2015.

[121] K. Prashanthi, M. Mandal, S.P. Duttagupta, R. Pinto, and V.R. Palkar. Fabrication and characterization of a novel magnetoelectric multiferroic mems cantilevers on si. *Sensors and Actuators A: Physical*, 166(1):83 – 87, 2011.

[122] Y. Hui, T. Nan, N. X. Sun, and M. Rinaldi. High resolution magnetometer based on a high frequency magnetoelectric mems-cmos oscillator. *Journal of Microelectromechanical Systems*, 24(1):134–143, 2015.

[123] Oswaldo Diéguez, Silvia Tinte, A. Antons, Claudia Bungaro, J. B. Neaton, Karin M. Rabe, and David Vanderbilt. Ab initio study of the phase diagram of epitaxial batio$_3$. *Phys. Rev. B*, 69:212101, 2004.

[124] Oswaldo Diéguez, Karin M. Rabe, and David Vanderbilt. First-principles study of epitaxial strain in perovskites. *Phys. Rev. B*, 72:144101, 2005.

[125] N. A. Pertsev, A. G. Zembilgotov, and A. K. Tagantsev. Effect of mechanical boundary conditions on phase diagrams of epitaxial ferroelectric thin films. *Phys. Rev. Lett.*, 80:1988–1991, 1998.

[126] S. P. Alpay, I. B. Misirlioglu, A. Sharma, and Z.-G. Ban. Structural characteristics of ferroelectric phase transformations in single-domain epitaxial films. *Journal of Applied Physics*, 95(12):8118–8123, 2004.

[127] Diego López González, Arianna Casiraghi, Florian Kronast, Kévin J.A. Franke, and Sebastiaan van Dijken. Influence of magnetic field and ferromagnetic film thickness on domain pattern transfer in multiferroic heterostructures. *Journal of Magnetism and Magnetic Materials*, 441:404 – 408, 2017.

[128] Takao Shimizu, Dai Suwama, Hiroki Taniguchi, Tomoyasu Taniyama, and Mitsuru Itoh. Structural Modification and Domain Structure in a $BaTiO_3$ Film on (110) $SrTiO_3$. *Applied Physics Express*, 6(1):015803, 2013.

[129] A. Biswas, P. B. Rossen, C.-H. Yang, W. Siemons, M.-H. Jung, I. K. Yang, R. Ramesh, and Y. H. Jeong. Universal Ti-rich termination of atomically flat $SrTiO_3$ (001), (110), and (111) surfaces. *Applied Physics Letters*, 98(5):051904, 2011.

[130] Woon Seob Lee and Seung S. Lee. Piezoelectric microphone built on circular diaphragm. *Sensors and Actuators A: Physical*, 144(2):367 – 373, 2008.

[131] Yongqiang Qiu, James V. Gigliotti, Margeaux Wallace, Flavio Griggio, Christine E. M. Demore, Sandy Cochran, and Susan Trolier-McKinstry. Piezoelectric micromachined ultrasound transducer (pmut) arrays for integrated sensing, actuation and imaging. *Sensors*, 15(4):8020–8041, 2015.

[132] K. W. Cho, S. H. Yi, Y. H. Son, and S. Y. Kweon. Characteristics of piezoelectric micro-speaker fabricated with ZnO thin film. *Integrated Ferroelectrics*, 89(1):141–149, 2007.

[133] M.C. Robinson, P.D. Hayenga, J.H. Cho, C.D. Richards, R.F. Richards, and D.F. Bahr. Fabrication methods for improved electromechanical behavior in piezoelectric membranes. *MRS Proceedings*, 872:J18.26, 2005.

[134] Jaianth Vijayakumar, David Bracher, Tatiana M. Savchenko, Michael Horisberger, Frithjof Nolting, and C.A.F. Vaz. Electric field control of magnetism in Si_3N_4 gated Pt/Co/Pt heterostructures. *Journal of Applied Physics*, 125(114101), 2019.

[135] C. A.F. Vaz, F. J. Walker, C. H. Ahn, and S. Ismail-Beigi. Intrinsic interfacial phenomena in manganite heterostructures. *Journal of Physics Condensed Matter*, 27(12), 2015.

[136] C. A. F. Vaz, Y. Segal, J. Hoffman, F. J. Walker, and C. H. Ahn. Growth and characterization of PZT/LSMO multiferroic heterostructures. *Journal of Vacuum Science & Technology B, Nanotechnology and Microelectronics: Materials, Processing, Measurement, and Phenomena*, 28(4):C5A6–C5A10, 2010.

[137] D. D. Lam, F. Bonell, Y. Shiota, S. Miwa, T. Nozaki, E. Tamura, N. Mizuochi, T. Shinjo, Y. Suzuki, and S. Yuasa. Growth of perpendicularly magnetized thin films on a polymer buffer and voltage-induced change of magnetic anisotropy at the MgO—CoFeB interface. *AIP Advances*, 5(6), 2015.

[138] Takeshi Seki, Makoto Kohda, Junsaku Nitta and Koki Takanashi. Coercivity change in an FePt thin layer in a Hall device by voltage application. *Applied Physics Letters*, 212505:1–4, 2012.

[139] Wen-Chin Lin, Po-Chun Chang, Cheng-Jui Tsai, Tsung-Chun Hsieh and Fang-Yuh Lo. Magnetism modulation of Fe / ZnO heterostructure by interface oxidation. *Applied Physics Letters*, 103(212405):1–6, 2016.

[140] A. Bernand-Mantel, L. Herrera-Diez, L. Ranno, S. Pizzini, J. Vogel, D. Givord, S. Auffret, O. Boulle, I. M. Miron, and G. Gaudin. Electric-field control of domain wall nucleation and pinning in a metallic ferromagnet. *Applied Physics Letters*, 102(12):122406, 2013.

[141] H. A. R. Wegener, A. J. Lincoln, H. C. Pao, M. R. O'Connell, R. E. Oleksiak, and H. Lawrence. The variable-threshold transistor, a new electrically-alterable, nondestructive read-only storage device. *IEEE Transactions on Electron Devices*, 15(6):420–421, 1968.

[142] Panagiotis Dimitrakis. *Charge-Trapping Non-Volatile Memories*. Springer International Publishing AG Switzerland, 2015.

[143] P. F. Carcia, A. D. Meinhaldt, and A. Suna. Perpendicular magnetic anisotropy in Pd/Co thin film layered structures. *Applied Physics Letters*, 47(2):178–180, 1985.

[144] P. F. Carcia. Perpendicular magnetic anisotropy in Pd/Co and Pt/Co thin-film layered structures. *Journal of Applied Physics*, 63(10):5066–5073, 1988.

[145] W. B. Zeper, F. J A M Greidanus, P. F. Carcia, and C. R. Fincher. Perpendicular magnetic anisotropy and magneto-optical Kerr effect of vapor-deposited Co/Pt-layered structures. *Journal of Applied Physics*, 65(12):4971–4975, 1989.

[146] J. Quispe-Marcatoma, H. Tarazona, B. Pandey, M. A. De Sousa, M. Carvalho, C. V. Landauro, F. Pelegrini, and E. Baggio Saitovitch. Spin reorientation transition in Co/Au multilayers. *Thin Solid Films*, 568(1):117–121, 2014.

[147] Keiki Fukumoto, Hiroshi Daimon, Liviu Chelaru, Francesco Offi, and Wolfgang Kuch. Micromagnetic properties of the Cu / Ni crossed-wedge film. *Science And Technology*, 514:151–155, 2002.

[148] N. Tournerie, A. P. Engelhardt, F. Maroun, and P. Allongue. Influence of the surface chemistry on the electric-field control of the magnetization of ultrathin films. *Physical Review B - Condensed Matter and Materials Physics*, 86(10):1–5, 2012.

[149] Lukas Gerhard, Frédéric Bonell, Wulf Wulfhekel, and Yoshishige Suzuki. Influence of an electric field on the spin-reorientation transition in Ni/Cu(100). *Applied Physics Letters*, 105(15), 2014.

[150] Bingfeng Miao, Yonketimtchev Millev, Liang Sun, Biao You, Wei Zhang, and Haifeng Ding. Thickness-driven spin reorientation transition in ultrathin films. *Science China: Physics, Mechanics and Astronomy*, 56(1):70–84, 2013.

[151] N. Bergeard, J. P. Jamet, A. Mougin, J. Ferré, J. Gierak, E. Bourhis, and R. Stamps. Dynamic fluctuations and two-dimensional melting at the spin reorientation transition. *Physical Review B - Condensed Matter and Materials Physics*, 86(9):1–5, 2012.

[152] M. Kronseder, M. Buchner, H. G. Bauer, and C. H. Back. Dipolar-energy-activated magnetic domain pattern transformation driven by thermal fluctuations. *Nature Communications*, 4:1–6, 2013.

[153] M. Kronseder, T. N.G. Meier, M. Zimmermann, M. Buchner, M. Vogel, and C. H. Back. Real-time observation of domain fluctuations in a two-dimensional magnetic model system. *Nature Communications*, 6:1–7, 2015.

[154] W. Kuch, K. Fukumoto, J. Wang, F. Nolting, C. Quitmann, and T. Ramsvik. Thermal melting of magnetic stripe domains. *Physical Review B - Condensed Matter and Materials Physics*, 83(17):1–4, 2011.

[155] J. A. Kittl, K. Opsomer, M. Popovici, N. Menou, B. Kaczer, X. P. Wang, C. Adelmann, M. A. Pawlak, K. Tomida, A. Rothschild, B. Govoreanu, R. Degraeve, M. Schaekers, M. Zahid, A. Delabie, J. Meersschaut, W. Polspoel, S. Clima, G. Pourtois, W. Knaepen, C. Detavernier, V. V. Afanas'ev, T. Blomberg, D. Pierreux, J. Swerts, P. Fischer, J. W. Maes, D. Manger, W. Vandervorst, T. Conard, A. Franquet, P. Favia, H. Bender, B. Brijs, S. Van Elshocht, M. Jurczak, J. Van Houdt, and D. J. Wouters. High-k dielectrics for future generation memory devices (Invited Paper). *Microelectronic Engineering*, 86(7-9):1789–1795, 2009.

[156] F.J.A. den Broeder, W. Hoving, and P.J.H. Bloemen. Magnetic anisotropy of multilayers. *Journal of Magnetism and Magnetic Materials*, 93(C):562–570, 1991.

[157] John Canny. A Computational Approach to Edge Detection. *IEEE Transactions on Pattern Analysis and Machine Intelligence*, PAMI-8(6):679–698, 1986.

[158] Jaianth Vijayakumar. Matlab code for analyzing domain wall fluctuations for PEEM images. *https://github.com/jaianthv/XPEEM-image-analysis-Domain-wall-fluctuations*, 2018.

[159] Motohiro Suzuki, Hiroaki Muraoka, Yuuki Inaba, Hayato Miyagawa, Naomi Kawamura, Takehito Shimatsu, Hiroshi Maruyama, Naoki Ishimatsu, Yoichi Isohama, and Yoshiaki Sonobe. Depth profile of spin and orbital magnetic moments in a subnanometer Pt film on Co. *Phys. Rev. B*, 72:054430, 2005.

[160] Kentaro Toyoki Aya Obinata, Takamasa Hirai, Yoshinori Kotani, Tomohiro Koyama Tetsuya Nakamura, and Daichi Chiba. Electric field effect on magnetism in a MgO / Pd / Co system with a solid-state capacitor structure. *AIP Advances*, 8:115122, 2018.

[161] Shinji Miwa, Motohiro Suzuki, Masahito Tsujikawa, Kensho Matsuda, and Takayuki Nozaki. Voltage controlled interfacial magnetism through platinum orbits. *Nature Communications*, 8:15848, 2017.

[162] Aya Obinata, Yuki Hibino, Daichi Hayakawa, Tomohiro Koyama, and Kazumoto Miwa. Electric-field control of magnetic moment in Pd. *Nature Publishing Group*, 5:14303, 2015.

[163] Y. Hibino, T. Koyama, A. Obinata, T. Hirai, S. Ota, K. Miwa, S. Ono, F. Matsukura, H. Ohno, and D. Chiba. Peculiar temperature dependence of electric-field effect on magnetic anisotropy in co/pd/mgo system. *Applied Physics Letters*, 109(8):082403, 2016.

[164] William Fuller Brown. Thermal fluctuations of a single-domain particle. *Physical Review*, 130(5):1677–1686, 1963.

[165] R. W. Chantrell U.Nowak, O. N. Mryasov, R. Wieser, K. Guslienko. Spin dynamics of magnetic nanoparticles: Beyond Brown's theory. *Physical Review B*, 72(172410):1–4, 2005.

[166] I. Rosenman F. Batallan and C. B. Sommers. Band structure and fermi surface of hcp ferromagnetic cobalt. *Physical Review B*, 11:545–557, 1975.

[167] R. Lorenz and J. Hafner. Magnetic structure and anisotropy of thin Fe films on Cu(001) substrates. *Physical Review B - Condensed Matter and Materials Physics*, 54(22):15937–15949, 1996.

[168] D. A. Muller, T. Sorsch, S. Moccio, F. H. Baumann, K. Evans-Lutterodt, and G. Timp. The electronic structure at the atomic scale of ultrathin gate oxides. *Nature*, 399(6738):758–761, 1999.

[169] J. S. Thorp, T. G. Bushell, D. Evans, and N. E. Rad. The temperature and frequency dependencies of permittivity and dielectric loss in reaction bonded silicon nitride. *Journal of Materials Science*, 22(7):2641–2644, 1987.

[170] D. T. Krick, P. M. Lenahan, and J. Kanicki. Electrically active point defects in amorphous silicon nitride: An illumination and charge injection study. *Journal of Applied Physics*, 64(7):3558–3563, 1988.

[171] John Robertson and Martin J. Powell. Gap states in silicon nitride. *Applied Physics Letters*, 44(4):415–417, 1984.

[172] M. J. Powell. Charge trapping instabilities in amorphous silicon-silicon nitride thin-film transistors. *Applied Physics Letters*, 43(6):597–599, 1983.

[173] S. M. Sze. Current transport and maximum dielectric strength of silicon nitride films. *Journal of Applied Physics*, 38(7):2951–2956, 1967.

[174] W. S. Lau, S. J. Fonash, and J. Kanicki. Stability of electrical properties of nitrogen-rich, silicon-rich, and stoichiometric silicon nitride films. *Journal of Applied Physics*, 66(6):2765–2767, 1989.

[175] T. P. Ma. Making silicon nitride film a viable gate dielectric. *IEEE Transactions on Electron Devices*, 45(3):680–690, 1998.

[176] Shu-Ju Tsai, Chiang-Lun Wang, Hung-Chun Lee, Chun-Yeh Lin, Jhih-Wei Chen, Hong-Wei Shiu, Lo-Yueh Chang, Han-Ting Hsueh, Hung-Ying Chen, Jyun-Yu Tsai, Ying-Hsin Lu, Ting-Chang Chang, Li-Wei Tu, Hsisheng Teng, Yi-Chun Chen, Chia-Hao Chen, Chung-Lin Wu. Approaching Defect-free Amorphous Silicon Nitride by

Plasma-Assisted Atomic Beam Deposition for High Performance Gate Dielectric. *Scientific Reports*, 6:28326, 2016.

[177] Seonghoon Woo, Kai Litzius, Benjamin Krüger, Mi Young Im, Lucas Caretta, Kornel Richter, Maxwell Mann, Andrea Krone, Robert M. Reeve, Markus Weigand, Parnika Agrawal, Ivan Lemesh, Mohamad Assaad Mawass, Peter Fischer, Mathias Kläui, and Geoffrey S.D. Beach. Observation of room-temperature magnetic skyrmions and their current-driven dynamics in ultrathin metallic ferromagnets. *Nature Materials*, 15(5):501–506, 2016.

[178] A. Hrabec, N. A. Porter, A. Wells, M. J. Benitez, G. Burnell, S. McVitie, D. McGrouther, T. A. Moore, and C. H. Marrows. Measuring and tailoring the dzyaloshinskii-moriya interaction in perpendicularly magnetized thin films. *Phys. Rev. B*, 90:020402, 2014.

[179] C. A. F. Vaz, S. J. Steinmuller, and J. A. C. Bland. Roughness-induced variation of magnetic anisotropy in ultrathin epitaxial films: The undulating limit. *Phys. Rev. B*, 75:132402, 2007.

[180] S. J. Steinmuller, C. A. F. Vaz, V. Ström, C. Moutafis, D. H. Y. Tse, C. M. Gürtler, M. Kläui, J. A. C. Bland, and Z. Cui. Effect of substrate roughness on the magnetic properties of thin fcc co films. *Phys. Rev. B*, 76:054429, 2007.

[181] D Mitin, A Kovacs, T Schrefl, A Ehresmann, D Holzinger, and M Albrecht. Magnetic properties of artificially designed magnetic stray field landscapes in laterally confined exchange-bias layers. *Nanotechnology*, 29(35):355708, 2018.

[182] W. Kuch, Xingyu Gao, and J. Kirschner. Competition between in-plane and out-of-plane magnetization in exchange-coupled magnetic films. *Physical Review B - Condensed Matter and Materials Physics*, 65(6):644061–644067, 2002.

[183] M. Farle, B. Mirwald-Schulz, A. Anisimov, W. Platow, and K. Baberschke. Higher-order magnetic anisotropies and the nature of the spin-reorientation transition in face-centered-tetragonal Ni(001)/Cu(001). *Physical Review B - Condensed Matter and Materials Physics*, 55(6):3708–3715, 1997.

[184] Justin M. Shaw, Hans T. Nembach, Mathias Weiler, T. J. Silva, Martin Schoen, Jonathan Z. Sun, and Daniel C. Worledge. Perpendicular Magnetic Anisotropy and Easy Cone State in Ta/Co 60 Fe 20 B 20 /MgO. *IEEE Magnetics Letters*, 6:3500404 (1–4), 2015.

[185] Jaianth Vijayakumar, C.A.F. Vaz. 3d image reconstruction of xpeem images. *https://github.com/jaianthv/3D-image-reconstruction-of-XPEEM-images*, 2018.

[186] Edmund G. Seebauer and Meredith C. Kratzer. Charged point defects in semiconductors. *Materials Science and Engineering: R: Reports*, 55(3):57 – 149, 2006.

[187] Roman Engel-Herbert, Yoontae Hwang, and Susanne Stemmer. Comparison of methods to quantify interface trap densities at dielectric/iii-v semiconductor interfaces. *Journal of Applied Physics*, 108(12):124101, 2010.

[188] J. L. Gavartin, D. Muñoz Ramo, A. L. Shluger, G. Bersuker, and B. H. Lee. Negative oxygen vacancies in HfO_2 as charge traps in high-k stacks. *Applied Physics Letters*, 89(8):082908, 2006.

[189] Minseok Jo, Hokyung Park, Man Chang, Hyung-Suk Jung, Jong-Ho Lee, and Hyunsang Hwang. Oxygen vacancy induced charge trapping and positive bias temperature instability in HfO_2 nMOSFET. *Microelectronic Engineering*, 84(9):1934 – 1937, 2007.

[190] R. Castagné and A. Vapaille. Description of the SiO_2Si interface properties by means of very low frequency MOS capacitance measurements. *Surface Science*, 28(1):157 – 193, 1971.

[191] Peng Zhao, Ava Khosravi, Angelica Azcatl, Pavel Bolshakov, Gioele Mirabelli, Enrico Caruso, Christopher L Hinkle, Paul K Hurley, Robert M Wallace, and Chadwin D Young. Evaluation of border traps and interface traps in HfO_2/MoS_2 gate stacks by capacitance–voltage analysis. *2D Materials*, 5(3):031002, 2018.

[192] J. Tao, C. Z. Zhao, C. Zhao, P. Taechakumput, M. Werner, S. Taylor, and P. R. Chalker. Extrinsic and intrinsic frequency dispersion of high-k materials in capacitance-voltage measurements. *Materials*, 5(6):1005–1032, 2012.

[193] https://sciencestruck.com/lcr-meter-working-principle-uses.

[194] David M Pozar. *Microwave engineering*. Fourth edition. Hoboken, NJ : Wiley ©2012, 2012.

[195] K. Sreenivas, Abhai Mansingh, and M. Sayer. Structural and electrical properties of rf-sputtered amorphous barium titanate thin films. *Journal of Applied Physics*, 62(11):4475–4481, 1987.

[196] Yonghun Kim, Young Gon Lee, Minwoo Kim, Chang Goo Kang, Ukjin Jung, Jin Ju Kim, Seung Song, James Blatchford, Brian Kirkpatrick, Hiro Niimi, Kwan-Yong Lim, and Byoung Lee. Capacitance Analysis of Highly Leaky Al_2O_3 MIM Capacitors Using Time Domain Reflectometry. *IEEE Electron Device Letters*, 33:1303–1305, 2012.

[197] C. Jorel, C. Vallée, P. Gonon, E. Gourvest, C. Dubarry, and E. Defay. High performance metal-insulator-metal capacitor using a $SrTiO_3/ZrO_2$ bilayer. *Applied Physics Letters*, 94(25):253502, 2009.

[198] Aparna Sanal, P. Sathyanarayanan, V. Velmurugan, and D. Kannadassan. Negative VCC in MIM capacitors: modeling and experiments. *Journal of Computational Electronics*, 17(1):458–462, 2018.

[199] Sun Jung Kim, Byung Jin Cho, Ming-Fu Li, Shi-Jin Ding, Chunxiang Zhu, Ming Bin Yu, B. Narayanan, A. Chin, and Dim-Lee Kwong. Improvement of voltage linearity in high- κ MIM capacitors using HfO_2-SiO_2 stacked dielectric. *IEEE Electron Device Letters*, 25(8):538–540, 2004.